NUMERICAL MODEL FOR AXISYMMETRIC INDUCTIVELY COUPLED PLASMA (ICP) IN RADIO-FREQUENCY (RF) ION THRUSTERS

by

Emre Türköz

B.S., Mechanical Engineering, Boğaziçi University, 2012

Submitted to the Institute for Graduate Studies in
Science and Engineering in partial fulfillment of
the requirements for the degree of
Master of Science

Graduate Program in Mechanical Engineering
Boğaziçi University

2014

NUMERICAL MODEL FOR AXISYMMETRIC INDUCTIVELY COUPLED PLASMA (ICP) IN RADIO-FREQUENCY (RF) ION THRUSTERS

APPROVED BY:

Assist. Prof. Murat Çelik .....
(Thesis Supervisor)

Assoc. Prof. Hakan Ertürk .....

Assist. Prof. Ahmet Öncü .....

DATE OF APPROVAL: 07.May.2014

ACKNOWLEDGEMENTS

I would like to express my sincere gratitude to Prof. Murat Çelik for his invaluable guidance and help during the preparation of this dissertation. I am grateful for his patience while giving me hope when I was stuck at dead-ends, and his deep understanding at the points where I fail. This study was very much like solving the pieces of a puzzle, which we could handle together and eventually produce this work.

I am grateful to the members of my thesis committee, Prof. Hakan Ertürk and Prof. Ahmet Öncü, for their time and invaluable advice in the process of bringing the pieces of this thesis together.

I want to thank Yevgeny Raitses, Igor Kaganovich and Alex Khrabrov from Princeton Plasma Physics Laboratory for the three educative months I spent in their research group. I am introduced to different aspects of plasma physics and had the opportunity to work with scientists and engineers from very diverse backgrounds. Our fruitful discussions have contributed greatly to the development of this work.

I am grateful to the senior members of the CFD/FMS laboratory supervised by Prof. Ali Ecder. Senior Ph.D. students of this laboratory, Erhan Turan and Yalın Kaptan have introduced me to world of computational fluid dynamics and led me into the world of academy. Without their supportive attitude and help in the beginning, I would not have embarked on this journey at the first place. I am especially grateful to Prof. Ali Ecder for leading me into the development of my first fluid codes.

I am supported financially by The Scientific and Technological Research Council of Turkey (TUBITAK) throughout my M.Sc. education. I want to thank them for eliminating financial obstacles during my education.

ABSTRACT

NUMERICAL MODEL FOR AXISYMMETRIC INDUCTIVELY COUPLED PLASMA (ICP) IN RADIO-FREQUENCY (RF) ION THRUSTERS

A numerical model is developed to evaluate the inductively coupled plasma properties in a 2-D axisymmetric domain inside an RF ion thruster discharge chamber. The model is built by incorporating an electromagnetic model with a fluid model to describe the plasma. The three species, ions, electrons and neutrals, inside the plasma are modeled assuming that they obey the continuum approach. The spatial distributions of flow parameters are obtained by solving the fluid equations with the SIMPLE algorithm using the finite volume discretization. The flow parameters that can be monitored are ion number density, ion velocity in three dimensions, neutral number density, neutral velocity in three dimensions, electron flux, electron temperature, electric potential and electromagnetic fields. The resulting flow parameters are used to evaluate the thruster performance and efficiency. The model presented in this study demonstrates the same tendency with the experimental results from the literature and verified through comparison with commercial codes. The code is implemented as a software framework, which is named as AETHER, using C++ programming language. The model lays out that after a certain amount of power deposition, there is a trade-off between the efficiency and the thrust in an RF ion thruster.

ÖZET

RADYO-FREKANSI İYON MOTORLARI İÇİN EKSENEL SİMETRİK İNDÜKTİF ETKİLEŞİMLİ PLAZMA MODELLEMESİ

Radyo-frekansı iyon motorları içinde bulunan indüktif etkileşimli plazma parametrelerini elde etmek için iki boyutlu eksenel simetri kullanılarak bir sayısal model geliştirildi. Sayisal model akişkan ve elektromanyetik modellerin etkileşimi göz önüne alınarak oluşturuldu. Model, plazmayı oluşturan iyonlar, elektronlar ve nötr gazin süreklilik yasasina uyduğu var sayılarak geliştirildi. Akış parametrelerinin konumsal dağılımlari, model denklemlerinin sonlu hacimler yöntemiyle SIMPLE algoritmasi kullanılarak çozülmesiyle elde edildi. İyon parçacık yoğunluğu, üç boyutta iyon hız dağılımı, nötr parçacık yoğunluğu, üç boyutta nötr parçacık hız dağılımı, elektron akışı, elektron sıcaklığı, elektron potansiyel ve elektromanyetik alan dağılımları geliştirilen model ile hesaplandı. Elde edilen parametreler iyon motoru performansını ölçmek için kullanıldı. Bu çalışmada sunulan model ile elde edilen sonuçlarin literatürdeki deneylerlerle aynı eğilimleri gösterdiği gözlemlendi ve model ticari kullanıma açık bir yazılımla doğrulandı. Model C++ programlama dili kullanılarak AETHER ismi verilen yazılım biçiminde kodlandı. Modelin uygulanması sonucu bir radyo-frekansı iyon motorunda verim ile itki arasında doğrusal olmayan bir denge olduğu ortaya konuldu.

TABLE OF CONTENTS

LIST OF FIGURES

LIST OF TABLES

LIST OF SYMBOLS

A	Magnetic vector potential
B	Magnetic field
c	Thermal velocity
D	Electric displacement field
E	Electric field
e	Elementary charge
e	(subscript) electrons
H	Magnetic field intensity
i	(subscript) ions
k	Boltzmann's constant
k	(subscript) index
ku	(subscript) index for axial nodes on staggered grid
kv	(subscript) index for radial nodes on staggered grid
kp	(subscript) index for pressure nodes on staggered grid
m	Mass of a particle
n	Number density
n	(subscript) neutrals
p	Pressure
p	(subscript) plasma
Q	Energy flux
$\dot{R}$	Mass generation rate
T	Temperature
u	Axial velocity
v	Radial velocity
w	Azimuthal velocity
Γ	Particle flux
δ	Skin depth
$\Delta\phi$	Sheath potential drop

ϵ_0	Electric permittivity of vacuum
η_d	Discharge loss per ion
λ_{th}	Electron thermal conductivity
μ_0	Magnetic permeability of vacuum
ν	Collision frequency
ρ	Charge density
σ	Electrical conductivity
Φ	Grid transparency
ϕ	Electric potential
ω_p	Plasma frequency

LIST OF ACRONYMS/ABBREVIATIONS

DSMC	Direct Simulation Monte Carlo
EP	Electric Propulsion
GMRES	Generalized Minimal Residual Method
ICP	Inductively Coupled Plasma
ILU	Incomplete LU Factorization
PIC	Particle-in-Cell
RF	Radio-Frequency

1. INTRODUCTION

Plasma is existent in stars and places between stars in the free space. The word "plasma" indicates an ionized gas, which contains electrons, ions and neutrals. Plasma is the most common condition of the visible matter in the universe [5]. It is also found on earth, being subject to many applications ranging from thermonuclear fusion to semiconductor manufacturing and space propulsion, which is the subject of this work. The properties of the plasma vary also depending on the application. The plasma in the core of the stars is very hot and dense whereas the interstellar plasma is cold. Similarly, low-temperature plasma is used in semiconductor processing, whereas hot and dense plasma is required to be sustained in fusion applications. In this work, the focus is on low-temperature, weakly-ionized, relatively dense inductively coupled plasma that is generated through radio-frequency heating.

Plasma created on earth has the common problem of sustainability, which depends on many factors including the energy deposition, gas pressure and ionization fraction. The term radio-frequency (RF) plasma is used to indicate that the energy deposition mechanism into the plasma is by RF coils. RF plasma can be classified into three groups as inductively coupled, capacitively coupled, and helicon mode [1]. These modes differ from each other depending on the direction of the electric field inside the chamber that confines the plasma. If the electric field induced by RF coils is parallel to the walls, the plasma is called inductively coupled, whereas if the electric field is perpendicular to the walls, the plasma is called capacitively coupled. On the other hand, in the helicon mode, the electric field is neither parallel nor perpendicular to the chamber walls, but reaches the wall at a skewed angle.

Electric propulsion (EP) is an application area of plasma. It is a technology aimed at generating the maximum possible thrust with high exhaust velocities and minimum amount of propellant [6]. The reduction of the amount of propellant is the key consideration here, since smaller propellant mass and a long-lasting propulsion system can lead to high duration missions. The quantification of this property is performed

with the parameter called specific impulse, I_{sp}, which denotes the ratio between the momentum and the weight of the exhaust particle. I_{sp} is directly the measure of the propellant mass required to change the velocity of an object (spacecraft or satellite) in space. The relationship is laid out with the rocket equation [6]:

$$\Delta m_p = m_0 \left[1 - \exp\left(\frac{-\Delta V}{I_{sp} g} \right) \right] \tag{1.1}$$

where Δm_p is the propellant mass to be spent for a velocity increase of ΔV, g is the gravitational acceleration of earth, and m_0 is the initial spacecraft mass. The specific impulse therefore can be used as a parameter for fuel efficiency. Most advanced chemical rockets can achieve up to 450 sec of specific impulse [7], a value which is easily superseded by electric propulsion devices.

The idea of an RF ion thruster incorporates RF plasma physics into the EP framework. As a member of the electric propulsion technology, the radio-frequency ion engine, which is also known as RF ion thruster, is an easy-to-construct impulse generator for small thrust values. It is a plasma-based device which utilizes electrostatic force between grids to accelerate ionized gas out of the discharge chamber to generate thrust. Examples from the literature can be found such that the thrust is varying from 10 mN to 200 mN with specic impulse values ranging from 2500 to 5500 sec [8].

The RF ion thrusters are first invented in the 1960s in Germany [9]. Giessen University was the host of this invention. After that, Astrium GmbH, a private German company, has adopted this development and managed to build thrusters which can be used in space missions. The most advanced product of these early efforts was RIT-10, which has a 10 cm discharge chamber diameter. RIT-10 is space tested in 1992. This spacetest was performed on the EURECA carrier. RIT-10 was incorporated into the European ARTEMIS satellite, which was sent to the space for geo-stationary communication purposes. RIT-10 is lifetime tested for 15,000 hours in 2000. The commercially available RIT-10 package is also called as *RITA* [10].

After the development of the RIT-10 ion thruster, German Space Agency (DARA) has started a project in 1995 for RIT-15, which has a 15 cm chamber diameter and is planned to deliver specific impulse more than 4000 seconds at 50 mN of thrust [9]. This amount of specific impulse enables the application area of large geostationary satellites and platforms for RF ion thrusters.

Miniaturization of RF ion thrusters are performed in the late 2000s. Astrium GmbH and their partners in the academy developed RIT-μX, which is built for micropropulsion applications in 2007 [11]. In 2011, researchers from Giessen University and Moscow Aviation Institute designed a very large ion thruster, RIT-45, which has a discharge chamber diameter of 46.5 cm [12]. RIT-45 works with 35 kW power and delivers a specific impulse of 7000 s.

1.1. Previous Modeling Effort

Plasma physics simulations are relatively new in the modeling world, since most of the underlying physics is subject to further investigation. Numerical treatment of inductively coupled plasma is performed many times in the literature. Electromagnetic heating is the core of the process, which is again elaborated in many examples. Two application areas, plasma processing and plasma torch modeling, come forward for the fields that have similar physics as RF ion thrusters. Examples in the literature about these fields are very helpful in building a numerical model for RF plasma.

As for the plasma processing, Kawamura [13] offers a numerical model for inductively coupled plasma. Suekane [14] presented a simpler version of inductively coupled plasma model for plasma torches, which the model developed in this study greatly benefited from. This work includes the evaluation of the boundary conditions for the electromagnetic equations. Hammond [15] built a 2D fluid model of the inductively coupled plasma, which is an example on how to handle the electron energy equation. Kumar [16] and Hsu [17] also provided numerical models for inductively coupled plasma, incorporating energy equations for electrons and also other species along with the boundary conditions. Parent [18] developed a new scheme to solve for the species

transport equations using fluid model for plasma.

Additional to the RF plasma modeling efforts, there are other methodologies developed to simulate other EP plasma devices. The state of the art in plasma modeling for electric propulsion applications is using the kinetic model with the Particle-In-Cell (PIC) algorithm. Oh [19] laid out the basics of the particle tracking simulations for quasi-neutral plasma. Fife [20] developed a hybrid-PIC simulation scheme where the electrons are assumed to be fluid but remaining species are tracked using particles. Szabo [7] developed a fully kinetic model for plasma thrusters. The code AQUILA [21] is developed to simulate Hall thruster plume using the Hybrid-PIC approach.

There are few numerical models for ion thrusters in general, and there are models for inductively coupled plasma, but the number of models for RF ion thruster is very limited. A leading example [22] is based on evaluating the discharge loss per ion with an analytical model. This 0D model is simple but successful at predicting the performance of ion thrusters in real applications. It lays out the effect of the induced magnetic field due to the RF coils on the ion confinement and discusses factors that result in a decrease in the discharge loss per ion. Another recent 0D model [23] indicates a trade-off between mass utilization efficiency and power transfer efficiency with increasing gas flow rate.

Additional to the analytical models, there are also one or multi-dimensional RF ion thruster discharge chamber modeling studies. A simple transformer model [2] is first laid out for 1D modeling, assuming that the thruster is large enough to assume 1D approach could be valid. Then this model is extended to a 2D model [8] which evaluates the plasma parameters of RF ion thrusters with the help of additional experimental data specific for the thruster to be modeled. In that study, the plasma is treated as a continuum as it is treated in the same way as in this work. There are also studies with the kinetic approach, using a PIC (Particle-In-Cell) code to solve for the spatial distribution of the plasma parameters. An example model [24] is developed to evaluate the performance of the micro RF ion thrusters. A 3D fully kinetic model [25], that requires strong computation power, is laid out recently for RF ion thrusters.

Compared to a PIC code implementation, the usage of the fluid approach decreases the computational cost drastically. Plasma must obey the continuum approach for the fluid modeling to be possible. The investigation whether the inductively coupled plasma inside the RF ion thruster discharge chamber obeys the continuum approach is already performed [8]. Therefore a fluid model is developed in this work. The model presented in this work consists of three main components: Electromagnetic model, fluid model and the transformer model. The electromagnetic model handles the solution of the Maxwell's equations, the fluid model evaluates the flow of the plasma and the transformer model evaluates the matching circuit parameters and most importantly the alternating current magnitude to be supplied to the RF coils.

1.2. Concept and Description

The geometry of a conical and a cylindrical shaped discharge chamber can be seen in Figure 1.1 . The simplicity of the construction comes from the fact that there are no extra magnets that are needed to be assembled to generate a magnetic field topology, which is the case for the other types of ion engines. The necessary energy deposited into the partially ionized gas comes from the RF coils, which generates the inductively coupled plasma. Screen and accelerator grids can be seen on the right end of the discharge chamber, which accelerate ions out of the discharge chamber. Manufacturing of these grids is also subject to a great effort, since a great precision is required in the machining process. The grids can be made of several materials, such as carbon and molybdenum, whereas the discharge chamber is generally made of dielectric materials, such as quartz. Neutral Xenon gas is fed from the left end. Neutral Xenon atoms get ionized with the energy provided by the RF coils. The output from the discharge chamber is neutralized with a cathode, which can be seen aiming towards the plume of the thruster.

The heating mechanism of the discharge is the RF heating that deposits energy to the electrons. The electric field has only the component in the azimuthal direction and causes the electrons move back and forth as the alternating current changes direction in the coils. The time-varying electric field in the azimuthal direction induces magnetic

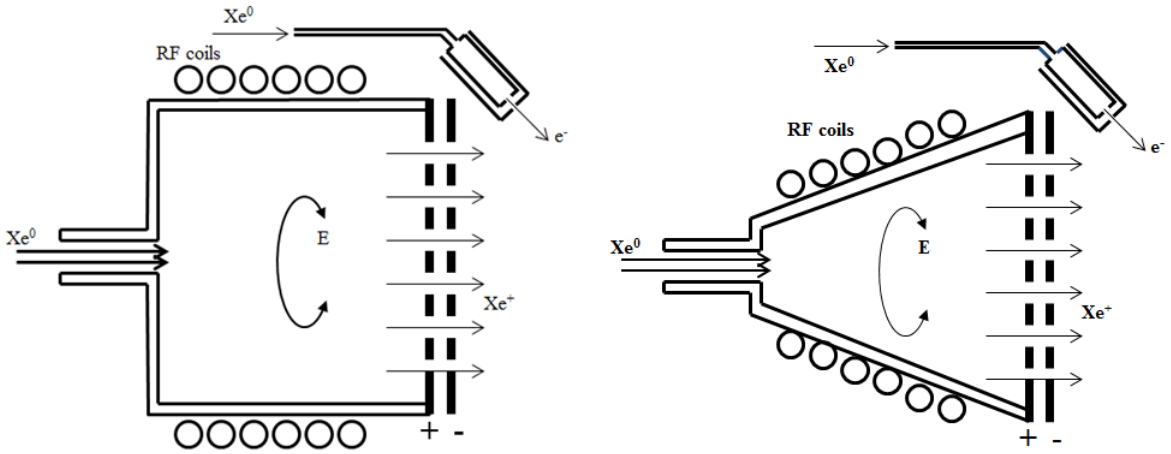

Figure 1.1. Representation of the cylindrical and conical discharge chambers.

field in radial and axial directions. These magnetic fields affect the charged particle velocities and they are accounted for in the scope of this study. The heated up electrons collide with the neutral gas atoms that are present in the chamber. Some of these collisions lead to ionization and therefore generate ions. The generated ions move inside the discharge chamber under the effect of the varying magnetic fields. Ions that are incident on the screen grid at the end of the discharge chamber are accelerated due to the high potential difference between the grids and are accelerated out of the chamber.

2. THEORY

Plasma is a collection of charged particles that move under the effects applied onto them or by the fields induced because of their charges. Plasma is on the average electrically neutral, which means that the ion number density is equal to the electron number density ($n_i = n_e$) [6]. This quasi-neutral medium is separated from the chamber walls with a narrow region of positively charged particles, which is called as *sheath*. The model which will be elaborated in the next section deals with the physics in the quasi-neutral medium. The representation of the sheath and the quasi-neutral region is given in Figure 2.1.

The existence of the sheath region is a consequence of the difference between the mobility of electrons and ions in the plasma. Even though the sheath is not spatially resolved in our model, it strongly affects the physics in the quasi-neutral part. Therefore the plasma sheath will not be completely ignored.

There are three separate modes of RF plasmas, which are called E, H and W-modes. These modes indicate different amount of energy coupling and result in different amount of densities.

The first mode, E-mode, is observed when the RF electromagnetic fields result in capacitively coupled plasma (CCP). Usually, the E-mode is observed when the plasma is generated with two parallel electrodes by applying an RF voltage across them. Typical plasma densities lies on the order of 10^{15} and 10^{16} m^{-3}. The CCP is utilized in various other applications like etching, which is not the interest of this work and therefore it is not covered further.

The main interest of this work is the H-mode, which is observed in inductively coupled plasmas (ICP). The reactors that process this type of plasmas are called inductive reactors. In inductive reactors with external coils, plasma generally starts in the E-mode and then switches to H-mode when the plasma density is increased to a

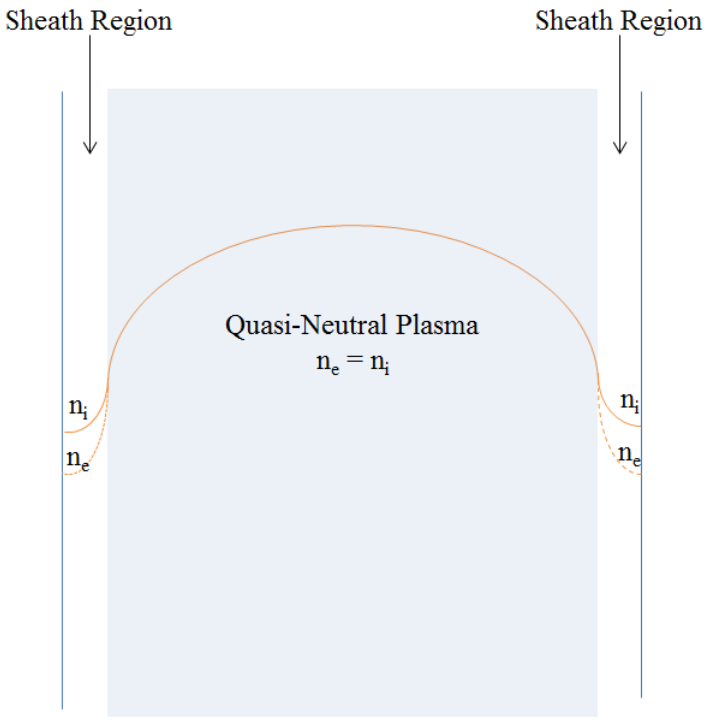

Figure 2.1. Representation of the sheath and the quasi-neutral regions in a plasma [1].

certain degree. This phenomenon, called as the E-H transition, is a field of study by itself. The physics of this transition is beyond the scope of this work. The plasma investigated in this work lies in the H-mode and assumed to remain so. The average density lies on the order of 10^{16} and 10^{18} m^{-3}.

The third mode, W-mode, is observed in helicon plasmas. In this mode, RF coils are supported by a background steady magnetic field to sustain a higher density plasma. Helicon plasmas are used for example in deep etching of hard materials and in the ionization stage of plasma thrusters. Typical densities in helicon mode lies above 10^{19} m^{-3}.

RF ion thrusters work with the inductively coupled plasma in the H-mode. The mode is important while determining equations to be included in the electromagnetic model. On the other hand, the modeling of the plasma dynamics is handled separately. There are two different approaches to the modeling of the plasma dynamics:

- **Based on Kinetic Theory**: This approach is known in the literature with its common name as Particle-In-Cell (PIC). PIC relies on statistical physics and it investigates the plasma in microscopic scale. Particle tracking with PIC relies on solving the Newton's first law of motion and electromagnetic field equations simultaneously. In this method, velocity or energy distributions in phase space, $f(\mathbf{r}, \mathbf{v}, t)$, are tracked using conservation laws. PIC is useful for investigating the microscale phenomena and turns out to be too complicated to investigate the macroscopic or high-pressure phenomena. High-pressure plasma calculations using PIC take too long. In this work, the PIC method is not preferred because of its high computational cost.
- **Based on Fluid Theory**: This approach approximates plasma as a fluid continuum and the governing equations are obtained through the integration of distribution functions over the velocity. It is useful at investigating the macroscopic behavior of the plasma. This approach is used and implemented in this work. The details of this approach is explained in the following sections of the text.

Since the fluid approximation is derived from the kinetic equations through taking the moments of the distribution conservation function, some basic definitions should be stated before delving directly into the fluid model.

The first term that needs to be clarified is the "distribution function." This function, $f(\mathbf{r}, \mathbf{v}, t)$, defines the number of particles in phase-space. Phase-space is the 6-dimensional volume element consisting of position ($\mathbf{r}$) and velocity ($\mathbf{v}$) components. The distribution function is the starting point for the derivation of many plasma parameters. For example, the number density of particles in the spatial volume element $d^3\mathbf{r}$ is found as:

$$n(\mathbf{r}, t) = \int_{-\infty}^{\infty} \int_{-\infty}^{\infty} \int_{-\infty}^{\infty} f(\mathbf{r}, \mathbf{v}, t) d^3\mathbf{v} \tag{2.1}$$

The important parameters for the fluid model is derived by averaging quantities over the velocity coordinates. For example, an important parameter for next derivations,

the mean velocity is denoted as:

$$\mathbf{u} = \langle \mathbf{v}(\mathbf{r},t) \rangle = \frac{1}{n(\mathbf{r},t)} \int_{-\infty}^{\infty} \int_{-\infty}^{\infty} \int_{-\infty}^{\infty} \mathbf{v} f(\mathbf{r},\mathbf{v},t) d^3\mathbf{v} \tag{2.2}$$

Another important statement for the following discussion is the assumption that $f \to 0$ sufficiently rapidly as the velocity goes to infinity so that for all functions $\Psi(\mathbf{v})$:

$$\lim_{|\mathbf{v}| \to \infty} (\Psi f) = 0 \tag{2.3}$$

Distribution functions obey a conservation rule. One of the most important equations of plasma physics is therefore the Boltzmann equation, which lays out the conservation scheme for the distribution function. The moments of this equation leads to the derivation of the fluid equations. The Boltzmann equation is denoted as:

$$\frac{\partial f}{\partial t} + \mathbf{v} \cdot \frac{\partial f}{\partial \mathbf{r}} + \frac{\mathbf{F}}{m} \cdot \frac{\partial f}{\partial \mathbf{v}} = \left(\frac{\partial f}{\partial t} \right)_c \tag{2.4}$$

where f is the distribution function in phase space, $\mathbf{F}$ denotes velocity independent forces, $\mathbf{r}$ is the position vector and $\mathbf{v}$ is the velocity vector. The subscript c stands for "collisions." The term on the RHS is the symbolic representation of the collision processes.

The equation above will be multiplied by a function $\Psi(\mathbf{v})$ and then integrated over velocity space. This procedure is named as "taking the moment of the kinetic equation." In the end, it will be shown that for the special cases of Ψ, continuity and momentum equations for plasma can be derived. The analysis presented below is obtained from [26].

When multiplied by $\Psi(\mathbf{v})$ and integrated over the velocity, the first term on the LHS of the Boltzmann equation becomes (since Ψ is independent of time):

$$\int \Psi(\mathbf{v}) \frac{\partial f}{\partial t} d\mathbf{v} = \frac{\partial}{\partial t} \int \Psi f d\mathbf{v} = \frac{\partial}{\partial t} (n \langle \Psi \rangle) \tag{2.5}$$

Similarly, since Ψ is also independent of $\mathbf{r}$, the second term becomes:

$$\int \Psi(\mathbf{v})\mathbf{v}\cdot \frac{\partial f}{\partial \mathbf{r}} d\mathbf{v} = \frac{\partial}{\partial \mathbf{r}}\cdot \int \Psi \mathbf{v} f d\mathbf{v} = \frac{\partial}{\partial \mathbf{r}}\cdot (n\langle \Psi \mathbf{v}\rangle) \tag{2.6}$$

The third term deals with the applied forces, $\mathbf{F}$:

$$\frac{1}{m}\int \Psi(\mathbf{v})\mathbf{F}\cdot \frac{\partial f}{\partial \mathbf{v}} d\mathbf{v} = \frac{\mathbf{F}}{m}\cdot \int \left[\frac{\partial(\Psi f)}{\partial \mathbf{v}} - f\frac{\partial \Psi}{\partial \mathbf{v}}\right] d\mathbf{v} \tag{2.7}$$

where the first term on the RHS in square brackets goes to zero as the distribution function vanishes as velocity goes to infinity, which means:

$$\frac{\mathbf{F}}{m}\cdot \int \left[\frac{\partial(\Psi f)}{\partial \mathbf{v}} - f\frac{\partial \Psi}{\partial \mathbf{v}}\right] d\mathbf{v} = -\frac{n}{m}\mathbf{F}\cdot \left\langle \frac{\partial \Psi}{\partial \mathbf{v}} \right\rangle \tag{2.8}$$

The formula above deals with the velocity independent force terms. But as it is the case with Lorentz force, the forcing term $\mathbf{F}$ can also have a velocity dependent component. In this case, using the summation convention:

$$\frac{e}{mc}\int \Psi(\mathbf{v})(\mathbf{v}\times \mathbf{B})_i \frac{\partial f}{\partial v_i} d\mathbf{v} \tag{2.9}$$

This may be rewritten as:

$$\frac{e}{mc}\int \left[\frac{\partial}{\partial v_i}(\Psi f(\mathbf{v}\times \mathbf{B})_i) - f(\mathbf{v}\times \mathbf{B})_i \frac{\partial \Psi}{\partial v_i}\right] d\mathbf{v} \tag{2.10}$$

The first term vanishes in the limit where velocity goes to the infinity. This gives:

$$\frac{e}{mc}\int \Psi(\mathbf{v})(\mathbf{v}\times \mathbf{B})\cdot \frac{\partial f}{\partial \mathbf{v}} d\mathbf{v} = -\frac{ne}{mc}\left\langle (\mathbf{v}\times \mathbf{B})\cdot \frac{\partial \Psi}{\partial \mathbf{v}} \right\rangle \tag{2.11}$$

Writing the three terms of the Boltzmann equation gives the general moment equation:

$$\frac{\partial n\langle \Psi\rangle}{\partial t} + \frac{\partial}{\partial \mathbf{r}}\cdot (n\langle \mathbf{v}\Psi\rangle) - \frac{n}{m}\mathbf{F}\cdot \left\langle \frac{\partial \Psi}{\partial \mathbf{v}} \right\rangle - \frac{ne}{mc}\left\langle (\mathbf{v}\times \mathbf{B})\cdot \frac{\partial \Psi}{\partial \mathbf{v}} \right\rangle = \int \Psi(\mathbf{v}) \left(\frac{\partial f}{\partial t}\right)_c d\mathbf{v} \tag{2.12}$$

The continuity and momentum fluid equations are obtained by setting the parameter Ψ to 1 and $m\mathbf{u}$, respectively. The fluid equations in closed form are therefore: Continuity equation ($\Psi = 1$):

$$\frac{\partial n}{\partial t} + \nabla\cdot(n\mathbf{u}) = S - L \tag{2.13}$$

Momentum equation ($\Psi = m\mathbf{u}$)

$$nm\left[\frac{\partial \mathbf{u}}{\partial t} + (\mathbf{u}\cdot\nabla)\mathbf{u}\right] = nq\mathbf{E} - \nabla p - m\mathbf{u}[n\nu_m + S - L] \tag{2.14}$$

where ν_m is the total elastic collision frequency. S and L denote the sources and the losses, respectively. The fluid equations are derived from the Boltzmann equation. But the information about the required parameters, like collision frequencies and reaction rates, must be obtained from the distribution function. Therefore the Boltzmann equation is valid for all kinds of distributions. For the RF plasmas investigated in this work, it is assumed that the electrons have Maxwellian energy distribution function. This approximation is supported by the empirical observations of Irving Langmuir, where he discovered that the electron distribution function was nearly Maxwellian by using the elestrostatic probes developed by himself [27].

Here the classical form of the Navier-Stokes equation should be remembered to make a comparison with ordinary hydrodynamics. The momentum equation for the ordinary fluids are formulated as:

$$\rho\left[\frac{\partial \mathbf{u}}{\partial t} + (\mathbf{u}\cdot\nabla)\mathbf{u}\right] = -\nabla p + \mu\nabla^2\mathbf{u} \tag{2.15}$$

where ρ is density, p is pressure and μ is viscosity. This is the same as the plasma momentum Equation 2.14 except for the absence of the electromagnetic forces and collisions between species. The equation above describes a fluid in which there are *frequent* collisions between its particles, whereas Equation 2.14 is derived without any explicit information regarding the collision rate [27]. This observation invokes the idea that the term that contains the viscosity can be modeled using collision terms derived

from the kinetic theory and Maxwellian distribution. The momentum source generated by neutral-neutral particle collisions should be equal to the momentum generated by the viscous term in the equation given above.

2.1. Maxwellian Distribution and Plasma-Wall Interactions

This study is based on the assumption that the electrons are distributed according to the Maxwellian distribution. We derive all the necessary boundary conditions and collision properties using this assumption.

The Maxwellian three-dimensional velocity distribution is given as [1]:

$$f(\mathbf{v}) = n\left(\frac{m}{2\pi kT}\right)^{3/2} exp\left(-\frac{m(v_x^2+v_y^2+v_z^2)}{2kT}\right) \tag{2.16}$$

where n is the number density, m is the mass, k is the Boltzmann constant, T is the temperature and v_x, v_y, and v_z are the velocity components in the specified directions. This distribution is crucial for our discussion since it is used to evaluate the *averaged* components.

The distribution equation given above is used to evaluate the particle and the thermal flux at the boundaries. To find the particle flux in one particular direction, say in our case the z direction, one should evaluate the integral:

$$\Gamma_{wall} = n\left(\frac{m}{2\pi kT}\right)^{3/2} \int_{-\infty}^{\infty} dv_x \int_{-\infty}^{\infty} dv_y \int_{0}^{\infty} v_z exp\left(-\frac{mv^2}{2kT}\right) dv_z \tag{2.17}$$

Here one should pay attention to the limits of the third integral, which is for the v_z component. To find the directed flux, the integral is evaluated over all x and y components of the velocity but only the positive z components [1]. To evaluate this integral, the following identities are used:

$$\int x e^{-cx^2} dx = -\frac{1}{2c} e^{-cx^2} \tag{2.18}$$

$$\int_{-\infty}^{\infty} e^{-cx^2} dx = \sqrt{\frac{\pi}{c}} \tag{2.19}$$

By expanding $v^2 = v_x^2 + v_y^2 + v_z^2$, it can be seen that the first relation above can be used to evaluate the integral for the z component of the velocity whereas the second relation is utilized to evaluate the remaining two integrals in x and y components of the velocity. Observing that c in the identities given above can be set equal to $m/2kT$ for this problem, the integral becomes:

$$\Gamma_{wall} = n \left(\frac{m}{2\pi kT}\right)^{3/2} \frac{\pi 2kT}{m} \frac{kT}{m} = n\sqrt{\frac{kT}{2\pi m}} = n\frac{1}{4}\sqrt{\frac{8kT}{\pi m}} \tag{2.20}$$

The term in the result of the integral $\sqrt{\frac{8kT}{\pi m}}$ denotes the thermal velocity which needs more elaboration. It is again evaluated using the Maxwellian distribution:

$$\langle v \rangle = \left(\frac{m}{2\pi kT}\right)^{3/2} \int_{-\infty}^{\infty}\int_{-\infty}^{\infty}\int_{-\infty}^{\infty} (v_x^2 + v_y^2 + v_z^2)^{1/2}\, exp\left(-\frac{m(v_x^2 + v_y^2 + v_z^2)}{2kT}\right) dv_x dv_y dv_z \tag{2.21}$$

This integral is equivalent to the expression using the Maxwellian speed distribution form:

$$\langle v \rangle = \left(\frac{m}{2\pi kT}\right)^{3/2} 4\pi \int_0^{\infty} v^3\, exp\left(-\frac{mv^2}{2kT}\right) dv \tag{2.22}$$

To evaluate this integral, the following relationship is used:

$$\int_0^{\infty} x^3 e^{-cx^2} = \frac{1}{2c^2} \tag{2.23}$$

Therefore, the result of this integral is:

$$\langle v \rangle = \bar{v} = \sqrt{\frac{8kT}{\pi m}} \tag{2.24}$$

which is called as the mean thermal velocity.

Here we have completed the derivation of an important plasma-wall interaction

relation. The particle flux for a species under no particular force is given as:

$$\Gamma_{wall} = n\frac{1}{4}\bar{v} \tag{2.25}$$

For the neutral species in our study this formulation specifies our boundary conditions for particle flux with an additional wall recombination term which will be elaborated later. For the electrons, the same procedure is applied with a slight difference. There is a special region formed during the plasma flow, which is called the sheath, in the locations very adjacent to the wall. For the electrons to reach the wall they should overcome a potential denoted as $\Delta\phi$, the sheath potential [1]. If the energy balance is formulated for an electron moving in the z direction and approaching the wall:

$$\frac{1}{2}mv_z^2 = e\Delta\phi \tag{2.26}$$

$$v_z = \sqrt{\frac{2e\Delta\phi}{m}} \tag{2.27}$$

Using the same logic, the wall particle flux is evaluated with the following integral:

$$\Gamma_{e,wall} = \int_V v_z f(\mathbf{v}) d\mathbf{v} = n\left(\frac{m}{2\pi kT}\right)^{3/2} \int_{-\infty}^{\infty} dv_x \int_{-\infty}^{\infty} dv_y \int_{\sqrt{2e\Delta\phi/m}}^{\infty} v_z exp\left(-\frac{mv^2}{2kT}\right) dv_z \tag{2.28}$$

Using the first integral relation 2.18, the last integral becomes:

$$\int_{\sqrt{2e\Delta\phi/m}}^{\infty} v_z exp\left(-\frac{mv_z^2}{2kT}\right) dv_z = \frac{kT}{m}\, exp\left(-\frac{e\Delta\phi}{kT}\right) \tag{2.29}$$

The remaining of the integral is evaluated using the second integral relation 2.19:

$$\Gamma_{e,wall} = n\left(\frac{m}{2\pi kT}\right)^{3/2} \frac{kT}{m}\, exp\left(-\frac{e\Delta\phi}{kT}\right) \frac{2kT}{m}\pi = n\left(\frac{kT}{\pi 2m}\right)^{1/2} exp\left(-\frac{e\Delta\phi}{kT}\right) = \frac{n\bar{v}}{4} exp\left(-\frac{e\Delta\phi}{kT}\right) \tag{2.30}$$

This yields the particle flux for the electrons on the boundary. This expression is very similar to the wall particle flux calculated in 2.25. The difference in between is the coefficient that contains the exponential function with the sheath potential drop.

The ion flux is formulated according to the physical limits for their motion. The ions in the presheath region can accelerate only up to the Bohm velocity, which is formulated as:

$$u_B = \sqrt{\frac{kT_e}{m_i}} \tag{2.31}$$

where T_e is the electron temperature and m_i is the ion mass. Based on this formulation, the ion flux to the wall is formulated as:

$$\Gamma_{i,wall} = n_i u_B \tag{2.32}$$

The sheath region adjacent to the wall does not affect the motion of the neutral species and the Bohm velocity is not a limitation for neutrals since they have much less thermal velocity. But the particle flux depends on the phenomenon named as wall recombination. The ions that reach the wall become neutral and go back into the discharge chamber as neutral species. This phenomenon is represented with Figure 2.2. Using the equation including that effect, the particle flux for the neutrals is denoted as:

$$\Gamma_{n,wall} = \frac{n_n \bar{v}_n}{4} - \gamma \Gamma_{i,wall} \tag{2.33}$$

where the subscript n denotes the neutral species, and the coefficient γ denotes the ratio of ions recombining at the wall to the neutrals. In this study, this value is taken to be equal to 1. The thermal flux is again evaluated using the Maxwellian distribution. The thermal flux is associated with the electrons, since they are the particles thermalized

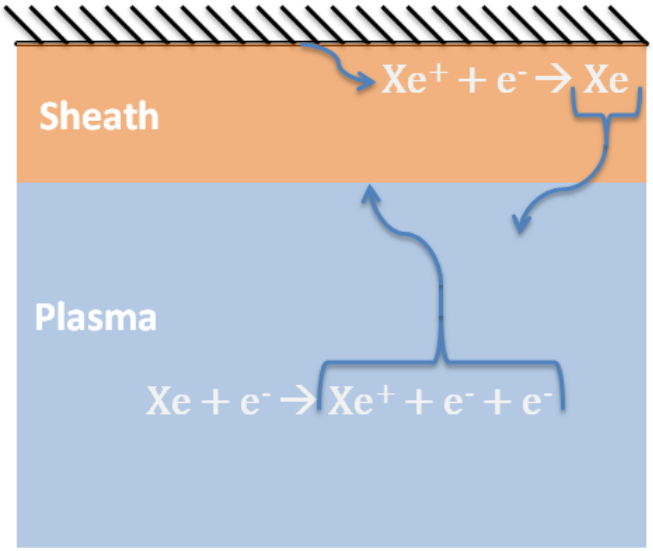

Figure 2.2. Representation of the wall recombination, where ions become neutrals.

in low temperature plasmas. Therefore, the energy flux leaving the plasma [1]:

$$Q = \left\langle \frac{1}{2} m v^2 v_z \right\rangle = n \left(\frac{m}{2\pi kT}\right)^{3/2} \frac{m}{2} \int_{-\infty}^{\infty} dv_x \int_{-\infty}^{\infty} dv_y \int_{\sqrt{2e\Delta\phi/m}}^{\infty} v^2 v_z exp\left(-\frac{mv^2}{2kT}\right) dv_z \tag{2.34}$$

The integral is evaluated using the integration by parts rule and utilizing 2.18:

$$\begin{aligned} &\int_{-\infty}^{\infty}\int_{-\infty}^{\infty}\int_{\sqrt{\frac{2e\Delta\phi}{m}}}^{\infty} v^2 v_z exp\left(-\frac{mv^2}{2kT}\right) = \\ &\int_{-\infty}^{\infty}\int_{-\infty}^{\infty}\left[v^2 \frac{kT}{m} exp\left(-\frac{m}{2kT}(v_x^2+v_y^2+v_z^2)\right)\right]^{v_z=\sqrt{\frac{2e\Delta\phi}{m}}} dv_y dv_x \\ &+ \int_{-\infty}^{\infty}\int_{-\infty}^{\infty}\int_{\sqrt{\frac{2e\Delta\phi}{m}}}^{\infty} \frac{kT}{m} 2v_z exp\left(-\frac{m}{2kT}(v_x^2+v_y^2+v_z^2)\right) dv_z dv_y dv_x \end{aligned} \tag{2.35}$$

To evaluate this integral, the integration by parts is used:

$$\int qdp = qp - \int pdq \tag{2.36}$$

To adapt this rule for the equation under consideration:

$$q = v^2 \tag{2.37}$$

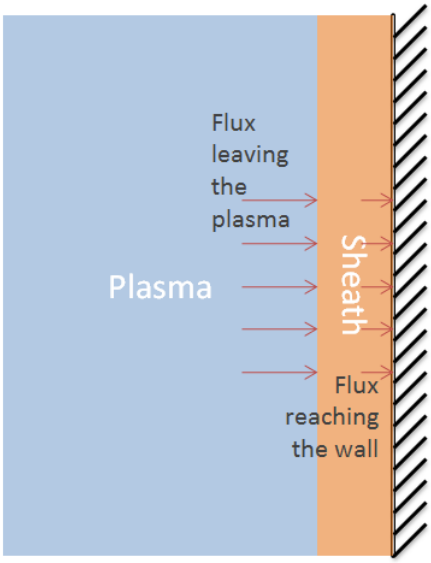

Figure 2.3. Representation of fluxes leaving the plasma and reaching the wall.

$$dp = v_z exp\left(-\frac{mv^2}{2kT}\right) \tag{2.38}$$

Evaluating this integral results in the RHS of Equation 2.35. For the sake of clarity, this integral is investigated in two parts. The first part is the double integral expression and the second part is the triple integral expression. Evaluating the first term, the double integral:

$$\begin{aligned}\int_{-\infty}^{\infty}\int_{-\infty}^{\infty}\left(v_x^2+v_y^2+\frac{2e\Delta\phi}{m}\right)\frac{kT}{m}exp\left(-\frac{m(v_x^2+v_y^2)}{2kT}\right)exp\left(-\frac{e\Delta\phi}{kT}\right)dv_y dv_x \\ = \frac{kT}{m}exp\left(-\frac{e\Delta\phi}{kT}\right)\left[\int_{-\infty}^{\infty}\int_{-\infty}^{\infty}(v_x^2+v_y^2)exp\left(-\frac{m(v_x^2+v_y^2)}{2kT}\right)dv_y dv_x + \right. \\ \left. \int_{-\infty}^{\infty}\int_{-\infty}^{\infty}\frac{2e\Delta\phi}{m}exp\left(-\frac{m(v_x^2+v_y^2)}{2kT}\right)dv_y dv_x\right]\end{aligned} \tag{2.39}$$

So, the second term is separated into two double integrals. The second double integral can be evaluated using the second integral relation 2.19:

$$\int_{-\infty}^{\infty}\int_{-\infty}^{\infty}\frac{2e\Delta\phi}{m}exp\left(-\frac{m(v_x^2+v_y^2)}{2kT}\right)dv_y dv_x = \frac{2e\Delta\phi}{m}\pi\frac{2kT}{m} \tag{2.40}$$

The first double integral can be evaluated using the polar coordinates:

$$\int_{-\infty}^{\infty}\int_{-\infty}^{\infty}(v_x^2+v_y^2)exp\left(-\frac{m(v_x^2+v_y^2)}{2kT}\right)dv_ydv_x=\int_0^{2\pi}\int_0^{\infty}r^2exp\left(-\frac{mr^2}{2kT}\right)rdrd\theta \tag{2.41}$$

where $r^2=v_x^2+v_y^2$. The integral is evaluated using the relation 2.23:

$$\int_0^{2\pi}\int_0^{\infty}r^2exp\left(-\frac{mr^2}{2kT}\right)rdrd\theta=\frac{1}{2}\frac{4k^2T^2}{m^2}2\pi=\frac{4k^2T^2\pi}{m^2} \tag{2.42}$$

With this result the evaluation of the double integral derived in 2.35 is completed. The triple integral in this expression is evaluated as follows:

$$\begin{aligned}\int_{-\infty}^{\infty}\int_{-\infty}^{\infty}\int_{\sqrt{\frac{2e\Delta\phi}{m}}}^{\infty}\frac{kT}{m}2v_zexp\left(-\frac{m}{2kT}(v_x^2+v_y^2+v_z^2)\right)dv_zdv_ydv_x=\\ \int_{-\infty}^{\infty}\int_{-\infty}^{\infty}\frac{2k^2T^2}{m^2}exp\left(-\frac{m(v_x^2+v_y^2)}{2kT}\right)exp\left(-\frac{e\Delta\phi}{kT}\right)dv_ydv_x\end{aligned} \tag{2.43}$$

Again, using 2.19:

$$\frac{2k^2T^2}{m^2}exp\left(-\frac{e\Delta\phi}{kT}\right)\int_{-\infty}^{\infty}\int_{-\infty}^{\infty}exp\left(-\frac{m}{2kT}(v_x^2+v_y^2)\right)dv_ydv_x=\frac{4k^3T^3\pi}{m^3}exp\left(-\frac{e\Delta\phi}{kT}\right) \tag{2.44}$$

The whole expression can be evaluated by bringing the results together from 2.40, 2.42 and 2.44:

$$Q=n\left(\frac{m}{2\pi kT}\right)^{3/2}\frac{m}{2}\frac{kT}{m}exp\left(-\frac{e\Delta\phi}{kT}\right)\left[\frac{2e\Delta\phi}{m}\pi\frac{2kT}{m}+\frac{4k^2T^2\pi}{m^2}+\frac{4k^2T^2\pi}{m^2}\right] \tag{2.45}$$

Evaluating the multiplications above yields:

$$Q=\left[n\sqrt{\frac{kT}{2\pi m}}exp\left(-\frac{e\Delta\phi}{kT}\right)\right](2kT+e\Delta\phi)=\left[\frac{n\bar{v}}{4}exp\left(-\frac{e\Delta\phi}{kT}\right)\right](2kT+e\Delta\phi) \tag{2.46}$$

The energy flux leaving the plasma is evaluated with this equation. According to [1], the energy flux leaving the plasma and the energy flux to the wall are not equal. The

energy flux to the wall is given as:

$$Q_{wall} = \left[\frac{n\bar{v}}{4} exp\left(-\frac{e\Delta\phi}{kT}\right)\right](2kT) \tag{2.47}$$

As it can be realized from the ongoing discussion, there is a distinction between the fluxes *leaving the plasma* and the fluxes *reaching the wall*. The distinction is represented in Figure 2.3. Regarding the particle flux, the distinction actually is not important due to the mass conservation, that is, the flux leaving the plasma from the presheath nodes actually is the same with the flux reaching the wall. But in the case of energy balance, things differ between the energy leaving the plasma and the energy reaching the wall. The difference in the amount of energy is absorbed by the sheath.

2.2. Collision Cross-Sections and Reaction Rates

Reaction rate denotes the number of particles per volume taking part in a specific type of reaction per second. Collisions that lead to a reaction is called as inelastic collisions. For this study, two types of inelastic collisions are considered. These reactions are formulated for the operating gas, Xenon, as follows:

- Ionization from neutral state: $Xe + e^- \longrightarrow Xe^+ + e^- + e^-$
- Excitation from neutral state: $Xe + e^- \longrightarrow Xe^* + e^-$

The ionization reaction rate is utilized in the continuity equation for ions and electrons as the source term and for neutrals as the loss term. Both the ionization and excitation rates are accounted for in the electron energy balance equation, where the reaction rates are used to calculate the energy loss due to inelastic collisions.

In this study, as stated many times before, the electrons are assumed to be distributed according to the Maxwellian distribution. The reaction rates are therefore defined as the product of the collision cross section and the electron thermal velocity

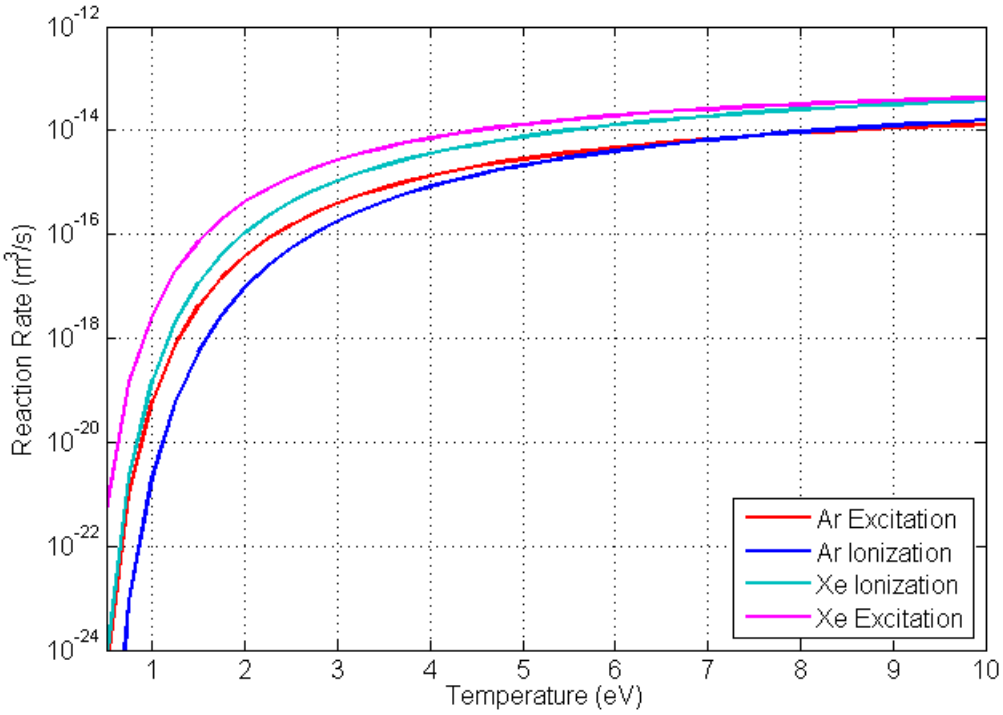

Figure 2.4. Reaction rates of Argon and Xenon.

averaged over the Maxwellian. It is denoted as:

$$\bar{Q} = \left\langle \mathbf{v}_e \sigma_{e-Xe}^{reaction} \right\rangle \tag{2.48}$$

where Q denotes the reaction rate, $\mathbf{v}_e$ is the electron velocity and $\sigma_{e-Xe}^{reaction}$ is the cross section of the collision under consideration. The guidelines to calculate this expression are presented in [28]. First, a normalized Maxwellian energy distribution for electrons are assumed:

$$f_e(E_e) = \frac{2}{\sqrt{\pi}} \sqrt{\frac{E_e}{(kT_e)^3}} e^{-\frac{E_e}{kT_e}} \tag{2.49}$$

the ionization reaction rate is calculated by the integral:

$$\bar{Q} = \int_0^\infty f_e(E_e) \sigma_{e-Xe}^{ion} \sqrt{\frac{2E_e}{m_e}} dE_e = \int_0^\infty 2E_e \sqrt{\frac{2}{\pi (kT_e)^3 m_e}} e^{-\frac{E_e}{kT_e}} \sigma_{e-Xe}^{ion} dE_e \tag{2.50}$$

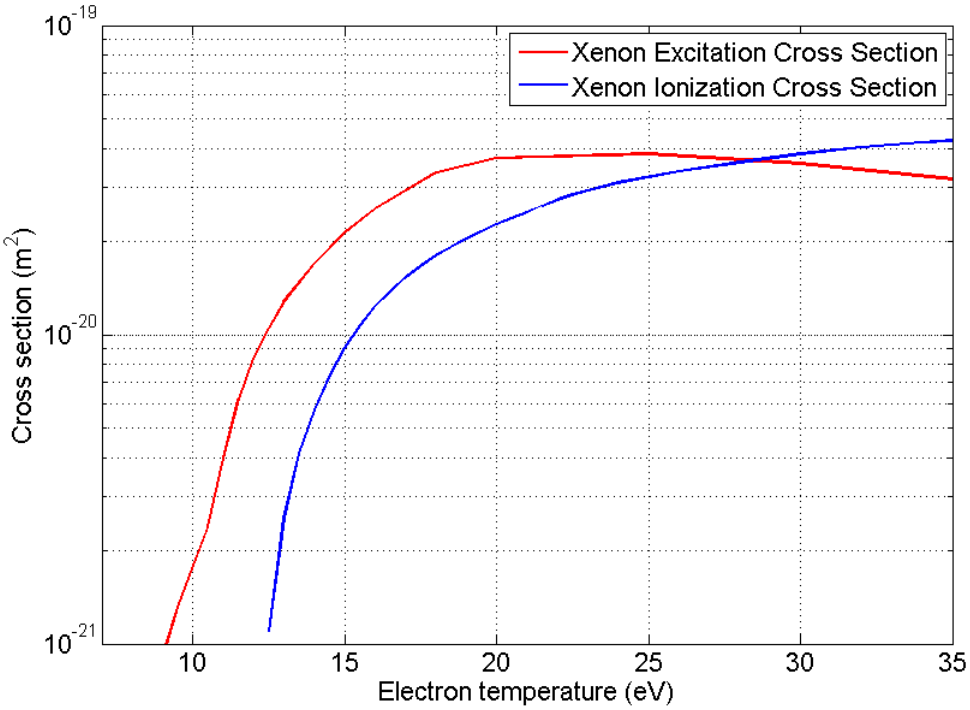

Figure 2.5. Xenon excitation and ionization cross sections.

where m_e is the electron mass, E_e is the electron energy, σ^{ion}_{e-Xe} is the ionization collision cross section as a function of energy, and $\sqrt{\frac{2E_e}{m_e}}$ is the electron velocity. The excitation reaction rate is calculated with the same formula, by only changing the collision cross-sections. This formula denotes a numerical integration over the electron energy, and is a function of temperature. Therefore, during the simulation, the reaction rate value of each node is evaluated according to the temperature value at this node.

The collision cross-section data is conventionally presented as a table which gives the collision cross section in m^2 for a particular energy level in eV. For the operating gas, Xenon, the data for ionization and excitation is obtained from [6]. Also for Argon, which is implemented in the code and can also be used in simulations, the data is obtained from [29].

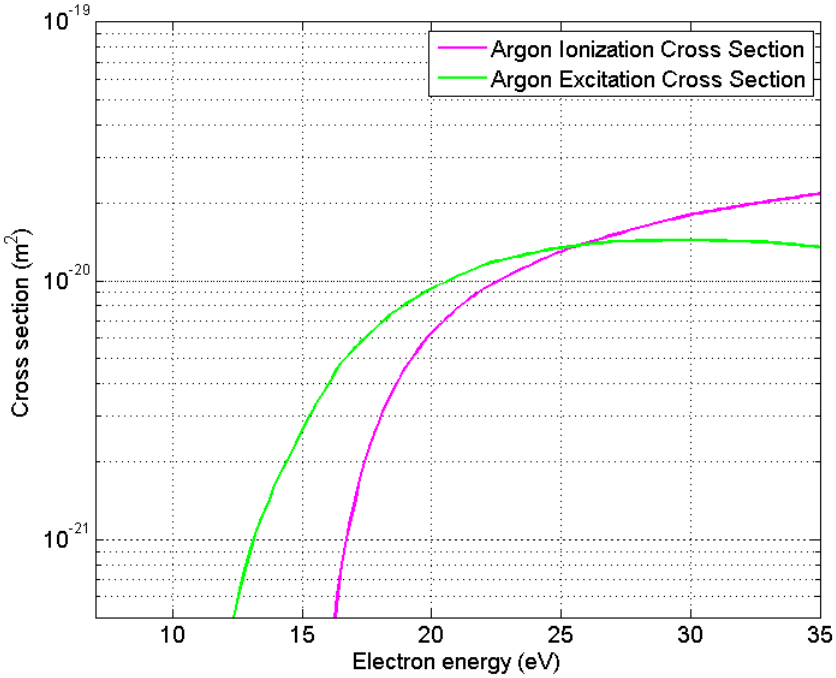

Figure 2.6. Argon excitation and ionization cross sections.

2.3. Electron Energy Balance

It is necessary to investigate the energy balance of electrons to calculate the electron temperature during simulations. Therefore the contribution of each physical process should be included in the energy equation to be developed. Here the terms that contribute to the electron energy balance equation are elaborated.

To start with the terms included in the energy balance, it is appropriate to express the random kinetic energy for each particle, which is formulated as:

$$\frac{3}{2}nkT \tag{2.51}$$

where the same expression takes the form of $\frac{1}{2}nkT$ for each direction. There is also a directed kinetic energy associated with the volume element:

$$\frac{1}{2}nmv^2 \tag{2.52}$$

Another contribution to the energy balance is the electromagnetic work. Electromagnetic work is also called as Joule heating (or cooling) due to the ambipolar electric field. It is formulated as:

$$\mathbf{E}\cdot(nq\mathbf{v}) \tag{2.53}$$

where q denotes the charge of the considered type of particle, which is $-e$ for electrons.

While writing the balance equation for a parameter, the flux across the boundaries of the control volume for this parameter is included into the equation. Energy flux across the boundary of an infinitesimal element is formulated as:

$$\nabla\cdot\mathbf{Q} = \nabla\cdot\int \mathbf{u}\frac{1}{2}mu^2 f(\mathbf{u})d^3\mathbf{u} = \nabla\cdot < n\mathbf{u}\frac{1}{2}mu^2 > \tag{2.54}$$

$$\mathbf{Q} = < n\mathbf{u}\frac{1}{2}mu^2 > \tag{2.55}$$

where f is the Boltzmann function in phase space. The velocity vector, $\mathbf{u}$ consists of two components:

$$\mathbf{u} = \mathbf{v} + \mathbf{w} \tag{2.56}$$

where $\mathbf{u}$ is the velocity of the fluid element, $\mathbf{v}$ is the mean velocity of the fluid and $\mathbf{w}$ is the difference between the velocity of the fluid element and the mean velocity. Substituting this expression for $\mathbf{u}$ into the energy flux equation yields:

$$\mathbf{Q} \;=\; n < (\mathbf{v}+\mathbf{w})\frac{1}{2}m(v^2 + 2\mathbf{v}\mathbf{w} + w^2) > \tag{2.57}$$

$$\mathbf{Q} = n\left\{\mathbf{v}\frac{1}{2}mv^2 + <\mathbf{w}>\frac{1}{2}mv^2 + \mathbf{v}\frac{1}{2}m<2\mathbf{vw}> + m<\mathbf{w}\cdot\mathbf{w}>\mathbf{v} + \mathbf{v}<\frac{1}{2}mw^2> + <\mathbf{w}\frac{1}{2}mw^2>\right\} \tag{2.58}$$

This expression can be reduced to:

$$\mathbf{Q} = \underbrace{\mathbf{v}\left(\frac{1}{2}nmv^2\right)}_{\substack{\text{convection of directed}\\ \text{(mean) kinetic energy}}} + \underbrace{\bar{\bar{p}}\cdot\mathbf{v}}_{\substack{\text{rate at which plasma}\\ \text{pressure does work}}} + \underbrace{\frac{3}{2}nkT\mathbf{v}}_{\substack{\text{convection of thermal}\\ \text{(random) kinetic energy}}} + \underbrace{\mathbf{q}}_{\substack{\text{heat flux due}\\ \text{to conduction}}} \tag{2.59}$$

with the following identities:

$$\bar{\bar{p}} = m<\mathbf{ww}> \tag{2.60}$$

where $\bar{\bar{p}}$ denotes the pressure tensor. The conduction term is formulated as:

$$\mathbf{q} = <\mathbf{w}\frac{1}{2}mw^2> = \int \mathbf{w}\frac{1}{2}mw^2 f(\mathbf{w})d^3w \tag{2.61}$$

So, putting the kinetic energy, electromagnetic work and the energy flux across the boundary together yields the primitive form of the energy equation:

$$\frac{\partial}{\partial t}\left(\frac{3}{2}nkT + \frac{1}{2}nmv^2\right) + \nabla\cdot\mathbf{Q} = nq\mathbf{E}\cdot\mathbf{v} + P_{source} \tag{2.62}$$

where P_{source} denotes the problem specific source term on the energy equation. Replacing the energy flux term with its extended form yields:

$$\frac{\partial}{\partial t}\left(\frac{3}{2}nkT + \frac{1}{2}nmv^2\right) + \nabla\cdot\left(\frac{1}{2}nmv^2\mathbf{v}\right) + p\left(\nabla\cdot\mathbf{v}\right) + \left(\nabla\cdot\mathbf{v}\right)\frac{3}{2}nkT + \nabla\cdot\mathbf{q} = nq\mathbf{E}\cdot\mathbf{v} + P_{source} \tag{2.63}$$

Using the relation $p = nkT$, and the fact that the directed kinetic energy is very small

compared to the thermal energy, the above equation becomes:

$$\frac{\partial}{\partial t}\left(\frac{3}{2}nkT\right)+\nabla\cdot\left(\frac{5}{2}nkT\right)\mathbf{v}+\nabla\cdot\mathbf{q}=nq\mathbf{E}\cdot\mathbf{v}+P_{source} \tag{2.64}$$

The conduction term is expressed according to the Fourier Law:

$$\mathbf{q}=-\lambda\nabla T \tag{2.65}$$

where λ denotes the thermal conductivity of electrons. According to [13], [17], [30], [31], [32], and [33]:

$$\lambda=\frac{5}{2}\frac{n_e e^2 T_e}{m_e\nu_{elastic}} \tag{2.66}$$

Inserting this expression into 2.64:

$$\frac{\partial}{\partial t}\left(\frac{3}{2}nkT\right)+\nabla\cdot\left(\frac{5}{2}nkT\right)\mathbf{v}+\nabla\cdot\left(-\frac{5}{2}\frac{n_e e^2 T_e}{m_e\nu_{elastic}}\nabla T_e\right)=nq\mathbf{E}\cdot\mathbf{v}+P_{source} \tag{2.67}$$

This equation is used as the energy equation in the model developed for this study. The most important assumption in this formulation is that the electron directed kinetic energy is small compared to the thermal energy. It is indeed true for the case of ICP discharges, since there is no very strong external electromagnetic fields that can actually confine and control the electron flow in RF plasma. The implementation of this equation in the model is explained in the upcoming sections.

3. NUMERICAL MODEL

The model consists of three submodels that communicate with each other throughout the simulation. These submodels are namely the fluid model, the electromagnetic model and the transformer model. Fluid equations are solved to evaluate the plasma flow parameters, whereas the electromagnetic model handles the calculation of the electromagnetic fields and the transformer model captures the effect of the matching circuit utilized in the real life experiments for constant power deposition. The equations are discretized with the finite volume method and the resulting linear systems are solved with iterative solvers including Jacobi and GMRES. The solved equations are continuity and momentum for ions and neutrals, electric potential equation, energy equation for electrons, and magnetic vector potential equation to evaluate the electromagnetic fields.

The discussion starts with the electromagnetic model (Section 3.1) and continues with the fluid model for plasma (Section 3.2). The underlying physics of these models are elaborated previously in Chapter 2. Then the transformer model is presented, whose formulations are obtained from previous works performed on inductively coupled plasma (Section 3.3). In the end of this chapter, the numerical method utilized in this work is explained (Section 3.4).

3.1. Electromagnetic Model

The RF heating model is based on the electromagnetic theory. Maxwell's equations govern the underlying physics:

Gauss' Law:

$$\nabla \cdot \mathbf{E} = \frac{\rho_{ch}}{\epsilon_0} \tag{3.1}$$

Gauss' Law for Magnetism:

$$\nabla \cdot \mathbf{B} = 0 \tag{3.2}$$

Faraday's Law:

$$\nabla \times \mathbf{E} = -\frac{\partial \mathbf{B}}{\partial t} \tag{3.3}$$

Ampere's Law:

$$\nabla \times \mathbf{H} = \mathbf{j} + \frac{\partial \mathbf{D}}{\partial t} \tag{3.4}$$

also utilizing the relations:

$$\mathbf{B} = \mu_r \mu_0 \mathbf{H} = \mu \mathbf{H} \quad \mathbf{D} = \kappa \epsilon_0 \mathbf{E} = \epsilon \mathbf{E} \tag{3.5}$$

The current density in Ampere's Law is given as:

$$\mathbf{j} = \sigma \mathbf{E} \tag{3.6}$$

For the equations presented above, the information related to the symbols and their meanings are presented in Table 3.1.

A special attention should be paid to Ampere's Law, as it is known that it is reformulated by adding the displacement current to the equation, which implies the inductance of a magnetic field through the change in the electric field.

Considering the conditions of the ICP discharge plasma, the displacement current can be neglected. Displacement currents are negligible in good conductors, and in this case plasma is assumed to have a high conductivity [8]. This reduces the Ampere's

Table 3.1. Symbols in the Maxwell's Equations.

Symbol	Meaning	SI Unit
E	*electric field*	volt per meter
B	*magnetic field*	tesla
D	*electric displacement field*	coulombs per square meter
H	*magnetic field intensity*	amperes per meter
j	*free current density*	amperes per meter square
ε_0	*permittivity of free space*	farads per meter
μ_0	*permeability of free space*	henries per meter
ρ	*total charge density*	coulombs per cubic meter
κ	*dielectric constant*	
μ_r	*relative permeability*	
$\epsilon = \epsilon_r\epsilon_0$	*permittivity of the medium*	farads per meter
$\mu = \mu_r\mu_0$	*permeability of the medium*	henries per meter
σ	*electrical conductivity*	siemens per meter

Law to the following form:

$$\nabla \times \mathbf{H} = \mathbf{j} \tag{3.7}$$

Instead of solving all of the four Maxwell's equations simultaneously, it is possible to eliminate some steps of calculations using the geometry of the domain. For this purpose, the magnetic vector potential, $\mathbf{A}$, is introduced, which is defined as:

$$\mathbf{B} = \nabla \times \mathbf{A} \qquad\qquad \nabla \cdot \mathbf{A} = 0 \tag{3.8}$$

Inserting the magnetic field relation in Equation 3.5 into the magnetic vector potential Equation 3.8:

$$\mu\mathbf{H} = \nabla \times \mathbf{A} \tag{3.9}$$

Inserting the relation found above into the reduced Ampere's Law 3.7 yields:

$$\nabla \times \nabla \times \mathbf{A} = \mu \mathbf{j} \tag{3.10}$$

A special attention should be paid to the magnetic permeability term. For the plasma medium, the magnetic permeability is assumed as: $\mu = \mu_0$. This assumption is demonstrated to be valid for low-temperature plasmas in [34].

Here, vector identities should be used to evaluate the left hand side, which contains two sequential cross products:

$$\nabla \times \nabla \times \mathbf{A} = \nabla(\nabla \cdot \mathbf{A}) - \nabla^2 \mathbf{A} \tag{3.11}$$

By the definition given in 3.8, first term on the right hand side at the relation given above yields zero. Using this and the equation derived in 3.10:

$$\nabla^2 \mathbf{A} = -\mu_0 \mathbf{j} \tag{3.12}$$

The current density is expressed as in 3.6. Replacing this expression:

$$\nabla^2 \mathbf{A} = -\mu_0 \sigma \mathbf{E} \tag{3.13}$$

Vector representing the electric field can also be replaced with a relation, which includes the magnetic vector potential. This relation can be evaluated using the Faraday's Law 3.3 and the definition of the magnetic vector potential 3.8:

$$\nabla \times \mathbf{E} = -\frac{\partial \mathbf{B}}{\partial t} = -\frac{\partial}{\partial t} \nabla \times \mathbf{A} = -\nabla \times \frac{\partial \mathbf{A}}{\partial t} \tag{3.14}$$

This expression results in:

$$\nabla \times \left(\mathbf{E} + \frac{\partial \mathbf{A}}{\partial t} \right) = 0 \tag{3.15}$$

A scalar potential can be defined as:

$$\mathbf{E} + \frac{\partial \mathbf{A}}{\partial t} = -\nabla \phi \tag{3.16}$$

In the absence of an electrostatic field in the plasma, the scalar potential is equal to zero [35]. The relation between the electric field and the magnetic vector potential is therefore defined as:

$$\mathbf{E} = -\frac{\partial \mathbf{A}}{\partial t} \tag{3.17}$$

This relation can be inserted into 3.13:

$$\nabla^2 \mathbf{A} = \mu_0 \sigma \frac{\partial \mathbf{A}}{\partial t} \tag{3.18}$$

This equation is the main equation in our model. To investigate this equation further, we need to define the vector Laplacian in cylindrical coordinates:

$$\nabla^2 \mathbf{A} = \begin{bmatrix} \frac{\partial^2 A_r}{\partial r^2} + \frac{1}{r^2}\frac{\partial^2 A_r}{\partial \theta^2} + \frac{\partial^2 A_r}{\partial z^2} + \frac{1}{r}\frac{\partial A_r}{\partial r} - \frac{2}{r^2}\frac{\partial A_\theta}{\partial \theta} - \frac{A_r}{r^2} \\ \\ \frac{\partial^2 A_\theta}{\partial r^2} + \frac{1}{r^2}\frac{\partial^2 A_\theta}{\partial \theta^2} + \frac{\partial^2 A_\theta}{\partial z^2} + \frac{1}{r}\frac{\partial A_\theta}{\partial r} - \frac{2}{r^2}\frac{\partial A_r}{\partial \theta} - \frac{A_\theta}{r^2} \\ \\ \frac{\partial^2 A_z}{\partial r^2} + \frac{1}{r^2}\frac{\partial^2 A_z}{\partial \theta^2} + \frac{\partial^2 A_z}{\partial z^2} + \frac{1}{r}\frac{\partial A_z}{\partial r} \end{bmatrix}$$

In the case of magnetic vector potential, only the theta component is nonzero. Since the coil currents flow in the azimuthal θ direction, the induced electric field must also be in the θ direction. Thus, the inductive fields are in the transverse electric mode, where the magnetic field has components in r and z. From the definition of the magnetic potential 3.8, it is derived that the magnetic vector potential only has the azimuthal component:

$$\mathbf{A} = (0, A_\theta, 0) \tag{3.19}$$

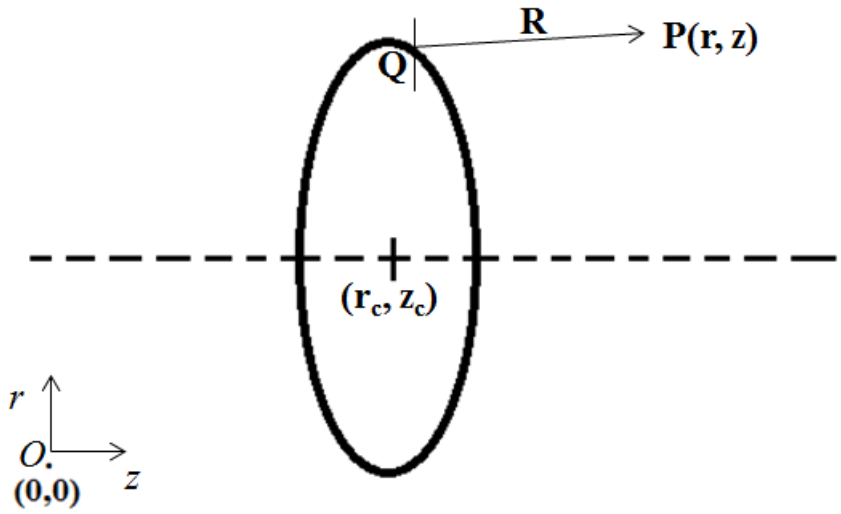

Figure 3.1. The loop on which the current flows and the important points used on derivation.

From the vector Laplacian, and considering the fact that the magnetic vector potential only has the azimuthal component, Equation 3.18 becomes:

$$\frac{\partial^2 A_\theta}{\partial r^2} + \frac{\partial^2 A_\theta}{\partial z^2} + \frac{1}{r}\frac{\partial A_\theta}{\partial r} - \frac{A_\theta}{r^2} = \mu_0 \sigma \frac{\partial A_\theta}{\partial t} \tag{3.20}$$

Solution of this PDE is straightforward if the boundary conditions are known. The boundary conditions will be found from the Biot-Savart law, which explores the magnetic field induced around a current carrying coil. Derivation here is based on the one presented in [8], but the expression derived here is more general than the one found in that text. Here also the geometry of the model should be elaborated. Biot-Savart law is expressed as:

$$d\mathbf{B}(P) = \frac{\mu}{4\pi}\frac{I d\mathbf{l} \times \hat{\mathbf{e}}_\mathbf{R}}{R^2} \tag{3.21}$$

where μ is the magnetic permeability constant, $d\mathbf{l}$ is infinitesimal length of the coil wire carrying current I, R is the radius of the coil, and $\hat{\mathbf{e}}_\mathbf{R}$ is the unit displacement vector from the wire element to the point at which the field is being computed. Here P stands for the point.

For the following derivation, we assume a Cartesian coordinate system for simplicity, but instead of (x,y,z) a (z,y,r) coordinate notation. The purpose of this notation choice is to have the final result in (r,z) coordinates. This approach is valid since azimuthal component of the magnetic field is not considered [8]. It is assumed that the origin of the coordinate system is aligned with the center of the current carrying coil in the y-direction. The alignment of the coil in the coordinate system is presented in Figure 3.1.

The required vectors for derivation are:

$$\mathbf{OP} = \begin{pmatrix} z \\ 0 \\ r \end{pmatrix} \quad \mathbf{OQ} = \begin{pmatrix} z_c \\ a\cos\theta \\ a\sin\theta + r_c \end{pmatrix}$$

where a denotes the radius of the coil and θ is the angle between the radial coordinate axis, which passes through the center point of the coil, and the vector connecting the center point of the coil to the point Q. The vector R can be expressed as:

$$\mathbf{R} = \mathbf{OP} - \mathbf{OQ} = \begin{pmatrix} z - z_c \\ -a\cos\theta \\ r - a\sin\theta - r_c \end{pmatrix}$$

Thus, to be used later:

$$R^2 = z^2 + z_c^2 + r^2 + r_c^2 + a^2 - 2rr_c - 2zz_c - 2ra\sin\theta + 2r_c a\sin\theta \tag{3.22}$$

The elementary length vectors from the Biot-Savart law are denoted as:

$$d\mathbf{l} = \frac{d(\mathbf{OQ})}{d\theta}d\theta = \begin{pmatrix} 0 \\ -ad\theta\sin\theta \\ ad\theta\cos\theta \end{pmatrix} \quad \mathbf{e_R} = \frac{\mathbf{R}}{|\mathbf{R}|}\begin{pmatrix} \frac{z-z_c}{R} \\ \frac{-a\cos\theta}{R} \\ \frac{r-a\sin\theta-r_c}{R} \end{pmatrix}$$

The cross product in the Biot-Savart equation is performed as:

$$d\mathbf{l} \times \mathbf{e_R} = \begin{vmatrix} i & j & k \\ 0 & -ad\theta \sin\theta & ad\theta \cos\theta \\ \frac{z-z_c}{R} & \frac{-a\cos\theta}{R} & \frac{r-a\sin\theta-r_c}{R} \end{vmatrix}$$

Substituting the result of this cross-product into the Biot-Savart law 3.21:

$$d\mathbf{B}(P) = \frac{\mu_0 I}{4\pi R^2} \begin{vmatrix} -a\sin\theta d\theta \left(\frac{r-a\sin\theta-r_c}{R}\right) + a\cos\theta d\theta \left(\frac{a\cos\theta}{R}\right) \\ \left(\frac{z-z_c}{R}\right) a\cos\theta d\theta \\ \left(\frac{z-z_c}{R}\right) a\sin\theta d\theta \end{vmatrix}$$

Rearranging the terms:

$$d\mathbf{B}(P) = \frac{\mu_0 I}{4\pi R^3} \begin{vmatrix} -ar\sin\theta + ar_c\sin\theta + a^2 \\ za\cos\theta - z_c a\cos\theta \\ za\sin\theta - z_c a\sin\theta \end{vmatrix} d\theta$$

Again:

$$d\mathbf{B}(P) = \frac{\mu_0 Ia}{4\pi R^3} \begin{vmatrix} -r\sin\theta + r_c\sin\theta + a \\ z\cos\theta - z_c\cos\theta \\ z\sin\theta - z_c\sin\theta \end{vmatrix} d\theta = \frac{\mu_0 Ia}{4\pi} \begin{vmatrix} \frac{-r\sin\theta+r_c\sin\theta+a}{R^3} \\ \frac{(z-z_c)\cos\theta}{R^3} \\ \frac{(z-z_c)\sin\theta}{R^3} \end{vmatrix} d\theta$$

We need to integrate the expression to find the magnetic field components in r and z directions. Remembering that:

$$R = \sqrt{z^2 + z_c^2 + r^2 + r_c^2 + a^2 - 2rr_c - 2zz_c - 2ra\sin\theta + 2r_c a\sin\theta} \tag{3.23}$$

And it should be observed:

$$\frac{\partial}{\partial z}\left(\frac{1}{R}\right) = -\frac{1}{2}\left(\frac{2z - 2z_c}{(z^2 + z_c^2 + r^2 + r_c^2 + a^2 - 2rr_c - 2zz_c - 2ra\sin\theta + 2r_c a\sin\theta)^{\frac{3}{2}}}\right) = -\frac{z - z_c}{R^3}$$

$$\frac{\partial}{\partial a}\left(\frac{1}{R}\right) = -\frac{1}{2}\left(\frac{2a - 2r\sin\theta + 2r_c\sin\theta}{(z^2 + z_c^2 + r^2 + r_c^2 + a^2 - 2rr_c - 2zz_c - 2ra\sin\theta + 2r_c a\sin\theta)^{\frac{3}{2}}}\right) = \frac{a - r\sin\theta + r_c\sin\theta}{R^3}$$

Using these relations, the magnetic field components can be expressed as:

$$d\mathbf{B}(P) = \frac{\mu_0 I a}{4\pi}\begin{vmatrix} -\frac{\partial}{\partial a}\left(\frac{1}{R}\right) \\ -\frac{\partial}{\partial z}\left(\frac{1}{R}\right)\cos\theta \\ -\frac{\partial}{\partial z}\left(\frac{1}{R}\right)\sin\theta \end{vmatrix} d\theta$$

Separating into components and integrating:

$$B_r = -\frac{\mu_0 I a}{2\pi}\frac{\partial}{\partial z}\int_{-\frac{\pi}{2}}^{\frac{\pi}{2}} \frac{\sin\theta d\theta}{(z^2 + z_c^2 + r^2 + r_c^2 + a^2 - 2rr_c - 2zz_c - 2ra\sin\theta + 2r_c a\sin\theta)^{\frac{1}{2}}} \tag{3.24}$$

$$B_z = -\frac{\mu_0 I a}{2\pi}\frac{\partial}{\partial a}\int_{-\frac{\pi}{2}}^{\frac{\pi}{2}} \frac{d\theta}{(z^2 + z_c^2 + r^2 + r_c^2 + a^2 - 2rr_c - 2zz_c - 2ra\sin\theta + 2r_c a\sin\theta)^{\frac{1}{2}}} \tag{3.25}$$

To validate these equations, one can calculate the magnetic field components on the center of the coil, namely on (r_c, z_c).

$$B_r(r_c, z_c) = 0 \tag{3.26}$$

$$B_z(r_c, z_c) = -\frac{\mu_0 I a}{2\pi}\frac{\partial}{\partial a}\int_{-\frac{\pi}{2}}^{\frac{\pi}{2}}\frac{d\theta}{a} = \frac{\mu_0 I}{2a} \tag{3.27}$$

This result is as expected and the equations are therefore validated. Before calculating the azimuthal component of the magnetic vector potential, more rearrangements can be made. Defining:

$$\phi = \frac{\theta + \pi/2}{2} \tag{3.28}$$

Using the trigonometric identities:

$$\sin\theta = \sin\left(2\phi - \pi/2\right) = -cos(2\phi) = -(1 - 2\sin^2\phi) \tag{3.29}$$

Then R becomes:

$$R = \sqrt{z^2 + z_c^2 + r^2 + r_c^2 + a^2 - 2rr_c - 2zz_c + 2ra(1 - 2\sin^2\phi) - 2r_c a(1 - 2\sin^2\phi)} \tag{3.30}$$

It can be seperated into two components as follows:

$$R = \sqrt{(z - z_c)^2 + (r - r_c + a)^2}\,\sqrt{1 - \frac{4a(r - r_c)\sin^2\phi}{(z - z_c)^2 + (r - r_c - a)^2}} \tag{3.31}$$

Here it is convenient to introduce a parameter, m:

$$m = \frac{4a(r - r_c)}{(z - z_c)^2 + (r - r_c + a)^2} \tag{3.32}$$

Rewriting the expression for radial magnetic field component using these variables:

$$B_r = \frac{\mu_0 I a}{2\pi}\frac{\partial}{\partial z}\left[\frac{1}{\sqrt{(z - z_c)^2 + (r - r_c + a)^2}}\int_0^{\frac{\pi}{2}}\frac{2(1 - 2\sin^2\phi)}{\sqrt{1 - m\sin^2\phi}}\,d\phi\right] \tag{3.33}$$

It is needed to do one more mathematical trick to form the expression suitable for

complete elliptic integrals. Defining:

$$D = 1 - m\sin^2\phi \tag{3.34}$$

$$\sin^2\phi = \frac{1-D}{m} \tag{3.35}$$

$$2 - 4\sin^2\phi = 2 - 4\left(\frac{1-(1-m\sin^2\phi)}{m}\right) = 2 - \frac{4}{m} + \frac{4}{m}(1 - m\sin^2\phi) \tag{3.36}$$

The radial component of the magnetic field becomes:

$$B_r = \frac{\mu_0 I a}{2\pi}\frac{\partial}{\partial z}\left[\frac{1}{\sqrt{(z-z_c)^2 + (r - r_c + a)^2}}\left(\left(2 - \frac{4}{m}\right)\int_0^{\frac{\pi}{2}} \frac{d\phi}{\sqrt{1 - m\sin^2\phi}} + \frac{4}{m}\int_0^{\frac{\pi}{2}} \sqrt{1 - m\sin^2\phi}\; d\phi\right)\right] \tag{3.37}$$

The expression above includes the complete elliptic integrals of first and second kind. They are defined respectively as:

$$K(m) = \int_0^{\frac{\pi}{2}} \frac{d\phi}{\sqrt{1 - m^2\sin^2\phi}} \tag{3.38}$$

$$E(m) = \int_0^{\frac{\pi}{2}} \sqrt{1 - m^2\sin^2\phi}\; d\phi \tag{3.39}$$

The radial magnetic field component can be expressed using the elliptic integrals as:

$$B_r = \frac{\mu_0 I a}{2\pi}\frac{\partial}{\partial z}\left\{\frac{1}{\sqrt{(z-z_c)^2 + (r - r_c + a)^2}}\left[\left(2 - \frac{4}{m}\right)K(\sqrt{m}) + \frac{4}{m}E(\sqrt{m})\right]\right\} \tag{3.40}$$

Now, the magnetic vector potential can be defined from the radial component of the magnetic field using the following relation:

$$-\frac{\partial A_\theta}{\partial z} = B_r \tag{3.41}$$

Therefore, magnetic vector potential is defined as:

$$A_\theta = -\frac{\mu_0 I a}{2\pi\sqrt{(z-z_c)^2+(r-r_c+a)^2}}\left[\left(2-\frac{4}{m}\right)K(\sqrt{m})+\frac{4}{m}E(\sqrt{m})\right] \tag{3.42}$$

where m is defined as in 3.32.

So, the expression found in 3.42 is used to evaluate the boundary condition. In case of multiple coils, their effects will be superposed on every boundary point to find the eventual BC value. When the coordinate system axis is aligned with the center of the coil, the r_c value is zero. Some rearrangements can be applied on 3.42 to have a compact form.

For $r_c = 0$:

$$m = \frac{4ar}{(z-z_c)^2+(r+a)^2} \tag{3.43}$$

And

$$A_\theta = \frac{\mu_0 I a}{2\pi\sqrt{(z-z_c)^2+(r+a)^2}}\frac{2}{m}\left[(2-m)K(\sqrt{m})-2E(\sqrt{m})\right] \tag{3.44}$$

Observe:

$$\frac{1}{\sqrt{(z-z_c)^2+(r+a)^2}} = \frac{\sqrt{m}}{2\sqrt{ar}} \tag{3.45}$$

Inserting this expression into the magnetic vector potential equation results in the final

compact form:

$$A_\theta = \frac{\mu_0 I}{2\pi}\sqrt{\frac{a}{r}}\,\frac{[(2-m)K(\sqrt{m}) - 2E(\sqrt{m})]}{\sqrt{m}} \tag{3.46}$$

where the calculation of the elliptic integrals of first and second kind is elaborated in Appendix A. This formula is the first part of the boundary condition on dielectric walls and it represents the effect of the coil. For multiple coils, the magnetic vector potential takes the form:

$$A_\theta = \frac{\mu_0 I}{2\pi}\sum_{i=1}^{coil}\sqrt{\frac{a}{R_0}}G(m_i) \tag{3.47}$$

where $G(m_i)$ is defined as:

$$G(m_i) = \frac{\left[(2-m_i)K(\sqrt{m_i}) - 2E(\sqrt{m_i})\right]}{\sqrt{m_i}} \tag{3.48}$$

The other component of the BC on dielectric walls comes from the induced current density in the plasma. From the numerical point of view, the plasma will be divided into N cylindrical control volumes and instead of the coil current, induced current in plasma will be implemented into the formula from the Biot-Savart law. So the I in the formula for the coil current contribution to the magnetic vector potential equation will be replaced by $j_{\theta,i}S_i$ where S_i denotes the side surface area whose normal is in the azimuthal direction of the computational element. The full expression for the boundary condition is:

$$A_\theta(r,z) = \frac{\mu_0 I}{2\pi}\sum_{i=1}^{coil}\sqrt{\frac{a}{r}}G(m_i) + \frac{\mu_0}{2\pi}\sum_{i=1}^{element}\sqrt{\frac{r_i}{r}}j_{\theta,i}S_i G(m_i) \tag{3.49}$$

where r_i denotes the element radial position. The boundary condition for the magnetic vector potential equation in case of the dielectric walls are evaluated with the formula given above.

3.2. Fluid Model

The model continues with the fluid model whose foundations are explained in Chapter 2. The fluid equations are listed below.

Continuity equations:

$$\frac{\partial n_i}{\partial t} + \nabla\cdot(n_i\mathbf{v_i}) = \dot{R}_i \tag{3.50}$$

$$\frac{\partial n_e}{\partial t} + \nabla\cdot(n_e\mathbf{v_e}) = \dot{R}_e \tag{3.51}$$

$$\frac{\partial n_n}{\partial t} + \nabla\cdot(n_n\mathbf{v_n}) = -\dot{R}_i \tag{3.52}$$

Momentum equations:

$$m_i n_i\left(\frac{\partial \mathbf{v_i}}{\partial t} + \mathbf{v_i}\cdot\nabla\mathbf{v_i}\right) + k\nabla(n_iT_i) = en_i\mathbf{E} + en_i\mathbf{v_i}\times\mathbf{B} - m_in_i\nu_{in}(\mathbf{v_i}-\mathbf{v_n}) - m_en_i\nu_{ei}(\mathbf{v_i}-\mathbf{v_e}) \tag{3.53}$$

$$m_e n_e\left(\frac{\partial \mathbf{v_e}}{\partial t} + \mathbf{v_e}\cdot\nabla\mathbf{v_e}\right) + k\nabla(n_eT_e) = -en_e\mathbf{E} - en_e\mathbf{v_e}\times\mathbf{B} - m_en_e\nu_{en}(\mathbf{v_e}-\mathbf{v_n}) - m_en_e\nu_{ei}(\mathbf{v_e}-\mathbf{v_i}) \tag{3.54}$$

$$m_n n_n\left(\frac{\partial \mathbf{v_n}}{\partial t} + \mathbf{v_n}\cdot\nabla\mathbf{v_n}\right) + k\nabla(n_nT_n) = -m_nn_n\nu_{in}(\mathbf{v_n}-\mathbf{v_i}) - m_en_n\nu_{en}(\mathbf{v_n}-\mathbf{v_e}) \tag{3.55}$$

The power balance for electrons:

$$\frac{3}{2}\frac{\partial}{\partial t}(n_eeT_e) + \nabla\cdot\mathbf{Q_e} = -e\mathbf{E_a}\cdot\mathbf{\Gamma_e} + P_{dep} - P_{coll} \tag{3.56}$$

Divergence-free current constraint:

$$\nabla\cdot\mathbf{j} = \nabla\cdot\left(n_i\mathbf{v}_i - n_e\mathbf{v}_e\right) = 0 \tag{3.57}$$

So, the model consists of the solutions for the 8 equations given above for the 8 parameters: n_i, n_e, n_n, $\mathbf{v_i}$, $\mathbf{v_e}$, $\mathbf{v_n}$, T_e and ϕ. These parameters represent ion number density, electron number density, neutral number density, ion velocity, electron velocity, neutral velocity, electron temperature, and electric potential, respectively. The term $\dot{R}_{species}$ denotes the source, which indicates the production of the specified species.

These equations can be solved to evaluate the plasma parameters. But there are some approximations applied in our model reduce the calculation costs. These approximations can be listed as follows:

- The species under consideration are assumed to obey the ideal gas law, and therefore the pressure gradient can be expressed as:

$$\nabla p \approx k\nabla(nT) \tag{3.58}$$

  where k denotes the Boltzmann's constant and n is the particle number density.
- The discharge chamber plasma parameters are assumed to be axially symmetric. Solutions are obtained in (r, z) plane, therefore azimuthal variations of density and temperature variables are neglected. This is the most basic assumption of our model. Thus, it allows us to reduce the 3D problem into a 2D problem.
- There will be no energy equation solved for ions and neutrals. Therefore, the temperature of these two species is assumed to be constant. This assumption is called as *cold-gas approximation*. The gas temperature can be taken as [8]:

$$T_i = T_n = 450\,K \tag{3.59}$$

  This approximation eliminates the temperature dependence in the pressure gradient term in momentum Equations 3.53 and 3.55.

- Quasi-neutrality, $n_i = n_e$, is assumed to hold throughout the domain, which means that the plasma sheath region incident to the walls is not physically resolved. Ions are assumed to leave the domain with Bohm velocity, which is formulated as:

$$v_i = \sqrt{\frac{kT_e}{m_i}} \tag{3.60}$$

- It is known from the experiments that electron temperature in a RF ion thruster discharge chamber is on the order of 3-5 eVs. This temperature range allows for making the assumption that secondary electron emission from the chamber walls is negligible. Also it is assumed that the double ionization is neglected, which requires 21.21 eV ionization energy.
- Solving the momentum equation for electrons is computationally expensive because electrons have much higher velocities than ions and neutrals have. The electron velocity can be captured properly only if a very small mesh size, on the order of the Debye length, is used and a very small time step is chosen. To overcome this challenge, an approximation to electron flux is used, which is called the drift-diffusion approximation [13]. In this formulation the ion and neutral velocities are neglected compared to the electron velocity. It is also assumed that the inertia terms of the momentum equation can be neglected because of the small electron mass. This approximation eliminates the nonlinearity of the momentum equation and the momentum equation becomes:

$$m_e n_e(\nu_{ei} + \nu_{en})\mathbf{v_e} = -\nabla P_e - e n_e \mathbf{E} - e n_e v_{e,\theta} \times \mathbf{B} \tag{3.61}$$

According to this expression the electron flux is:

$$\Gamma_e = n_e \mathbf{v}_e = -\frac{k}{m_e \nu_{elastic}} \nabla(T_e n_e) - \frac{e n_e}{m_e \nu_{elastic}} (\mathbf{E} + v_{e,\theta} \times \mathbf{B}) \tag{3.62}$$

where $\nu_{elastic} = \nu_{ei} + \nu_{en}$. With this formulation, the electron flux can be evaluated with the plasma parameters that are obtained from the other equations of the model.

Since there is no external electron source inside the thruster, the quasi-neutrality assumption makes the continuity equation for the electrons and ions identical. The ion generation rate is therefore equal to the electron generation rate inside the solution domain, which means that for each ion generated, there is also an electron that accompanies it. The ion generation rate is expressed as:

$$\dot{R}_e = \dot{R}_i = n_n n_e < \mathbf{v_e} \bar{Q}_{ion} > \tag{3.63}$$

where $\bar{Q}_{ion}$ is the ionization cross section and $< \mathbf{v_e} \bar{Q}_{ion} >$ is the Maxwellian averaged ionization rate function. The evaluation of this rate function is explained in Section 2.2.

Momentum equations include collision frequencies that need further elaboration. The collision terms are formulated as:

$$\nu_{en} = \bar{c}_e n_n \sigma_{en} \tag{3.64}$$

$$\nu_{ei} = \bar{c}_e n_i \sigma_{ei} \tag{3.65}$$

$$\nu_{in} = \bar{c}_i n_n \sigma_{in} \tag{3.66}$$

σ_{en} is the electron-neutral scattering cross-section, σ_{ei} is the electron-ion elastic collision cross section, and σ_{in} is the ion-neutral elastic collision cross-section. These values depend on the type of the gas and they can be obtained from the literature [29] for Xenon and Argon. $\bar{c}_e$ is electron thermal velocity which is formulated as:

$$\bar{c}_e = \sqrt{\frac{8kT_e}{\pi m_e}} \tag{3.67}$$

Similarly, the ion thermal velocity is:

$$\bar{c}_i = \sqrt{\frac{8kT_i}{\pi m_i}} \tag{3.68}$$

The energy equation includes the power deposition term, P_{dep}, which is formulated as:

$$P_{dep} = \frac{1}{2}\sigma_p |\mathbf{E}|^2 \tag{3.69}$$

where σ denotes the plasma conductivity. This term is formulated as [36]:

$$\sigma_p = \frac{\epsilon_0 \omega_p^2}{m_e \nu_{elastic}} \tag{3.70}$$

where ϵ_0 is the electric permittivity of free space. The expression includes the plasma frequency, which is formulated as:

$$\omega_p = \sqrt{\frac{n_e e^2}{\epsilon_0 m_e}} \tag{3.71}$$

Another parameter that needs to be defined in the energy balance Equation 3.56 is the power lost to elastic and inelastic collisions, P_{coll}.

$$P_{coll} = n_e n_n e < \mathbf{v_e} \bar{Q}_{ion} > U_{ion} + n_e n_n e < \mathbf{v_e} \bar{Q}_{exc} > U_{exc} + \sum_{h}^{heavy} \frac{2m_e}{m_h} \frac{3}{2} k(T_e - T_h)\nu_{eh} n_e \tag{3.72}$$

where, U_{ion} is the first ionization energy, U_{exc} is the excitation energy, and the terms in corner brackets represent the rate coefficients which are derived in Section 2.2. The first term in the collision power loss expression denotes the power loss due to ionization, whereas the second term is the power loss due to excitation collisions. The third term with the summation sign is the energy loss due to the elastic collisions between the electrons and the heavy species.

The first term on the right hand side of the energy Equation 3.56 denotes the Joule heating from the ambipolar field. The electron flux term, $\mathbf{\Gamma}_e$, is defined as:

$$\mathbf{\Gamma}_e = n_e \mathbf{v_e} \tag{3.73}$$

and

$$\mathbf{E_a} = -\frac{D_e}{\mu_e}\frac{\nabla n_e}{n_e} \tag{3.74}$$

where D_e and μ_e are diffusion constant and electron mobility, respectively [5]. The diffusion constant, diffusivity, is defined as:

$$D_e = \frac{kT_e}{m_e \nu_{elastic}} \tag{3.75}$$

and the electron mobility:

$$\mu_e = -\frac{e}{m_e \nu_{elastic}} \tag{3.76}$$

The second term on the left hand side is called electron energy flux. And it is defined as in Section 2.3:

$$\mathbf{Q_e} = \frac{5}{2}\mathbf{\Gamma}_e e T_e - \frac{5}{2}\frac{n_e e^2 T_e}{m_e \nu_{elastic}} \nabla T_e \tag{3.77}$$

The first term above defines the energy transported by electron net motion while the second term is the electron thermal conduction. The coefficient before the temperature gradient in the above expression is called as the thermal conductivity of plasma:

$$\lambda_{th} = \frac{5}{2}\frac{n_e e^2 T_e}{m_e \nu_{elastic}} \tag{3.78}$$

The divergence-free current constraint (Equation 3.57) is utilized to calculate the electric potential with the drift-diffusion approximation for electrons, which is formulated in Equation 3.62. The electric potential is embedded in the electric field term, which is formulated as:

$$\mathbf{E} = -\nabla\phi + \frac{\partial A_\theta}{\partial t} \tag{3.79}$$

Inserting this formulation into the drift-diffusion approximation and plugging 3.62 into the divergence-free current constraint (Equation 3.57) yields:

$$\nabla\cdot\left(n_e\mathbf{v}_i+\frac{k}{m_e\nu_{elastic}}\nabla(T_en_e)-\frac{en_e}{m_e\nu_{elastic}}\nabla\phi+\frac{en_e}{m_e\nu_{elastic}}(v_{e,\theta}\times\mathbf{B})\right)=0 \tag{3.80}$$

Multiplying the whole expression with the elementary charge e to obtain expressions containing the plasma conductivity and moving the electric potential term to the other side of the equation:

$$\nabla\cdot(\sigma\nabla\phi)=e\nabla\cdot(n_e\mathbf{v}_i)+\nabla\cdot\left(\frac{ek}{m_e\nu_{elastic}}\nabla(T_en_e)\right)+\nabla\cdot(\sigma(v_{e,\theta}\times\mathbf{B})) \tag{3.81}$$

This equation completes the equations in the model developed in the scope of this work.

Boundary conditions are extremely important, because they give the flow field its identity. The solution domain extends up to the plasma sheath region and throughout the domain it is assumed that the quasi-neutrality holds. In the end of the solution boundaries, ions are assumed to leave out the domain with Bohm velocity:

$$v_i=\sqrt{\frac{kT_e}{m_i}} \tag{3.82}$$

For the neutral momentum equation, it is assumed that the ions reaching the wall undergo recombination and go back into the system as neutrals. Therefore it is imposed that:

$$\mathbf{\Gamma}_n=-\mathbf{\Gamma}_i \tag{3.83}$$

For the domain edge adjacent to the accelerator grids, the ion and neutral grid transparency values are taken into account. Additional to the ions reflected from the grids, the neutral flux is affected by the neutrals that leave the domain. The neutral flux

adjacent to the grid is:

$$\mathbf{\Gamma}_n = -(1-\Phi_i)\mathbf{\Gamma}_i - \Phi_n n_n \frac{\bar{c}_n}{4} \tag{3.84}$$

where Φ_i denotes the ion transparency and Φ_n denotes the neutral transparency of the grids.

Boundary condition for the energy equation is evaluated in Section 2.1. According to the discussion presented in that section, the heat flux directed outwards from the domain is formulated:

$$Q = \left[\frac{n\bar{v}}{4} exp\left(-\frac{e\Delta\phi}{kT_e}\right)\right](2kT_e + e\Delta\phi) \tag{3.85}$$

where $\Delta\phi$ denotes the sheath potential drop at the sheath edge. The sheath potential drop is calculated using the fact that the dielectric walls have floating potential. According to this, the net current reaching the wall is zero. For the net current to be zero, the ion and electron flux reaching the wall should be zero:

$$n_i u_B = \frac{n_e \bar{c}_e}{4} exp\left(\frac{e\Delta\phi}{kT_e}\right) \tag{3.86}$$

where the left hand side is the expression for ion flux and the right hand side is the electron flux. Due to the quasi-neutrality ion density is equal to the electron density at the sheath edge: $n_i = n_e$. The sheath potential can be expressed as:

$$\Delta\phi = -\frac{kT_e}{e} \ln\left(\sqrt{\frac{m_i}{2\pi m_e}}\right) \tag{3.87}$$

3.3. Transformer Model

This transformer model is an adaptation of the model presented in [8]. The examples of modeling the inductively coupled discharge as the secondary coil of an air core transformer are to be found in [37].

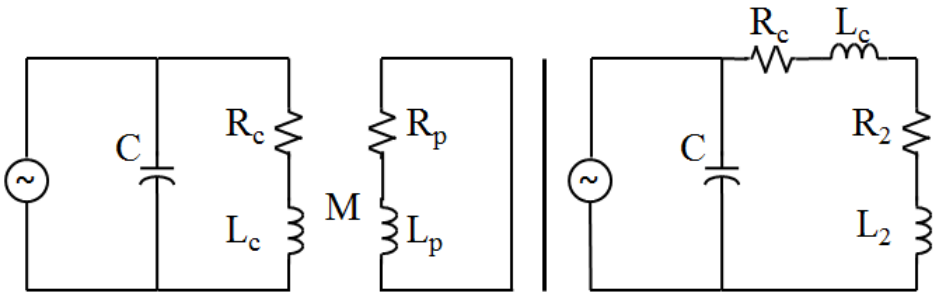

Figure 3.2. Representation of the transformer model. Plasma is represented as the secondary of an air-core transformer. The figure on the right shows the transformed circuit [2].

The transformer model is used to update the magnitude of the current supplied to the RF coil. The concept is called the matching network. The coil current magnitude is changed to increase the power deposition efficiency. There are models in the literature that evaluate the whole ICP as the secondary coil of an air core transformer and evaluate the global plasma parameters. Here in this work, as also presented in [8], the transformer model is used to to evaluate the coil current for maximum power deposition.

In the scope of this model, plasma is treated as a medium where the electrons can flow through. The circuit representation of plasma and the transformer model are depicted in Figure 3.2. In this figure C denotes the capacitance of the matching circuit, R_c is the coil resistance, and L_c is the coil inductance. R_p and L_p are resistance and inductance values of the plasma, respectively. The figure on the right hand side represents the circuit with transformed resistance and inductance, which are represented by R_2 and L_2, respectively.

The self-inductance of the coil, in [H], which is modeled as a short-solenoid is expressed as:

$$L_c = 0.002\pi \left(D_w \times 100\right) \left(N^2\right) \left[ln\left(\frac{4D_w}{l_c}\right) - \frac{1}{2}\right] \times 10^{-6} \tag{3.88}$$

where D_w is the winding diameter of the coil, which is taken as the outer diameter of

the discharge chamber.

The plasma inductance is expressed as:

$$L_p = 0.002\pi(D_p \times 100)\left[ln\left(\frac{4D_p}{L}\right) - \frac{1}{2}\right] \times 10^{-6} + \left(\frac{R_p}{\nu_{en}}\right) \tag{3.89}$$

The plasma resistance:

$$R_p = \frac{2\pi R}{\sigma L \delta} \tag{3.90}$$

From the plasma resistance equation, it can be seen how the plasma is attributed the characteristics of a conductor. The skin depth is formulated as:

$$\delta = \sqrt{\frac{2}{\omega \mu_0 \sigma}} \tag{3.91}$$

The mutual inductance is written for a coaxial coil as follows:

$$L_m = 0.0095N \frac{(D_p \times 100)^2}{\sqrt{(D_w \times 100)^2 + (l_c \times 100)^2}} \tag{3.92}$$

and the transformed plasma inductance and resistance become:

$$L_2 = \frac{-\omega^2 L_m^2 L_p}{R_p^2 + (\omega L_p)^2} \tag{3.93}$$

$$R_2 = \frac{\omega^2 L_m^2 R_p}{R_p^2 + (\omega L_p)^2} \tag{3.94}$$

After these definitions, the two parallel impedances in the transformed circuit can be defined as follows:

$$Z_1 = \frac{1}{j\omega C} \tag{3.95}$$

$$Z_2 = R_c + R_2 + j\omega L_c + j\omega L_2 \tag{3.96}$$

The total impedance is calculated from the well-known parallel impedances formula

$$Z = \frac{Z_1 Z_2}{Z_1 + Z_2} = \frac{\left(\frac{1}{j\omega C}\right)(R_c + R_2 + j\omega L_c + j\omega L_2)}{\left(\frac{1}{j\omega C}\right) + (R_c + R_2 + j\omega L_c + j\omega L_2)} \tag{3.97}$$

The total impedance is used to characterize the quality of the matching circuit by including this term into the calculation of the power reflection:

$$PR = \left|\frac{Z - Z_0}{Z + Z_0}\right|^2 \times 100\% \tag{3.98}$$

The peak current is calculated as follows:

$$I_{peak} = \frac{\sqrt{2 Z_0 P_{forward}}}{Z_0}\left(1 - \frac{Z - Z_0}{Z + Z_0}\right) \tag{3.99}$$

The peak current is used to calculate the RMS coil current which will be used to update the current magnitude:

$$I_{coil,RMS} = \left| I_{peak}\left(\frac{Z_1}{Z_1 + Z_2}\right)/\sqrt{2}\right| \tag{3.100}$$

3.4. Finite Volume Method and Discretization of Partial Differential Equations

The discretization of partial differential equations are performed according to the finite volume and finite difference discretization schemes. Finite volume method is utilized to solve the fluid equations whereas finite difference is utilized to solve the magnetic vector potential which is used to evaluate the electromagnetic fields.

Before delving into the details of the finite volume method, the discretization schemes for the gradient and del operators in cylindrical coordinates are presented

below.

The divergence of a vector, for example of the electron flux, $\mathbf{\Gamma}_e$, takes the form at r-z plane:

$$\nabla \cdot \mathbf{\Gamma}_e = \frac{\partial \Gamma_{e,z}}{\partial z} + \frac{1}{r}\frac{\partial (r\Gamma_{e,r})}{\partial r} \tag{3.101}$$

where $\Gamma_{e,r}$ and $\Gamma_{e,z}$ denote the components of the electron flux in radial and axial directions, respectively.

The gradient of a scalar, for example of the electron temperature, T_e, takes the form at r-z plane:

$$\nabla T_e = \frac{\partial T_e}{\partial z} + \frac{\partial T_e}{\partial r} \tag{3.102}$$

The Laplacian of a scalar, for example of the electric potential, ϕ, takes the form at r-z plane:

$$\nabla^2 \phi = \frac{\partial^2 \phi}{\partial r^2} + \frac{1}{r}\frac{\partial \phi}{\partial r} + \frac{\partial^2 \phi}{\partial z^2} \tag{3.103}$$

The equations included in the scope of the model presented contains either the gradient, divergence or the Laplacian of the parameters. These operators are discretized on the structured rectangular grid as follows:

First derivative in axial direction is discretized as:

$$\frac{\partial \phi}{\partial z} = \frac{\phi_{i+1,j} - \phi_{i-1,j}}{2\Delta z} \tag{3.104}$$

First derivative in radial direction is discretized as:

$$\frac{\partial \phi}{\partial r} = \frac{\phi_{i,j+1} - \phi_{i,j-1}}{2\Delta r} \tag{3.105}$$

The Laplacian operator that contains second derivatives is discretized as:

$$\nabla^2 \phi = \frac{\phi_{i+1,j} - 2\phi_{i,j} + \phi_{i-1,j}}{\Delta z^2} + \frac{\phi_{i,j+1} - 2\phi_{i,j} + \phi_{i,j-1}}{\Delta r^2} + \frac{1}{r_{i,j}} \frac{\phi_{i,j+1} - \phi_{i,j-1}}{2\Delta r} \tag{3.106}$$

where r denotes the radial coordinate of the node under consideration. These discretization formulas are utilized when finite difference discretization is applied to an equation. For the electric potential, whose final form is presented above, finite difference discretization is applied.

For the continuity and momentum equations, that are formulated in Equations 3.50, 3.52, 3.53, and 3.55, finite volume method is utilized with the SIMPLE algorithm [38].

SIMPLE algorithm relies on the mathematical formulation that the convective terms ($\mathbf{v} \cdot \nabla \mathbf{v}$) in momentum equations actually represent the flux conservation across the boundaries of a control volume element. Evaluating flux instead of trying to discretize the nonlinear convective term lays out a linear formulation of the momentum equation and facilitates the solution of the flow equations.

Before proceeding, the details of the control volume element should be explained. In this study, a structured rectangular mesh in cylindrical coordinates is utilized, which means that the radial distance, Δr, and the axial distance, Δz, of each grid cell is equal. This lays out a wedge shaped domain, where the volume of a cell is a function of the radial position of the cell. An example volume element for the axially symmetric domain is shown in Figure 3.3. In this figure it is observed that the west and east face

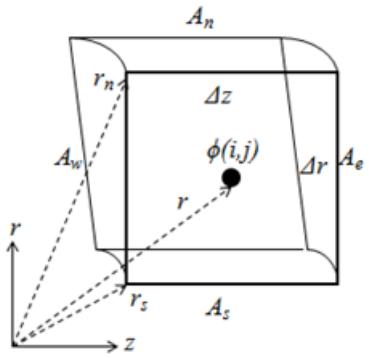

Figure 3.3. Control volume cell in cylindrical coordinates.

areas are equal to teach other ($A_e = A_w$) whereas the north face area is larger than the south face area ($A_n > A_s$).

The volume of a cell can be calculated first by evaluating the east or west area and multiplying this expression by the axial distance, Δz. According to this guideline, the volume of a control volume cell is:

$$\Delta V = (\pi r_n^2 - \pi r_s^2)\frac{\Delta\theta}{2\pi}\Delta z = (r_n + r_s)(r_n - r_s)\frac{1}{2}\Delta\theta\Delta z = \frac{(r_n + r_s)}{2}\Delta r\Delta\theta\Delta z \quad (3.107)$$

The structured, rectangular grid used in this work is represented in Figure 3.4. In this grid the alignment of the nodes can be seen on the staggered grid. On a staggered grid, the scalars are stored at the center of the control volume cell whereas the velocity nodes are located at the boundaries. Staggered grids are used in fluid simulations to avoid the odd-even decoupling between the pressure and velocity. Odd-even decoupling is a discretization error that can occur and lead to checkerboard patterns in the solutions [39].

According to the staggered grid alignment, the number of nodes on the grid for the flow parameters may vary. If it is desired to divide the axial domain in nz nodes, and the radial domain in nr nodes, the axial velocity grid is $(nz+1) \times (nr)$, the radial velocity grid is $(nz) \times (nr+1)$ and the scalar parameter grid is $(nz+1) \times (nr+1)$. The additional nodes are used to implement the boundary conditions, whose details

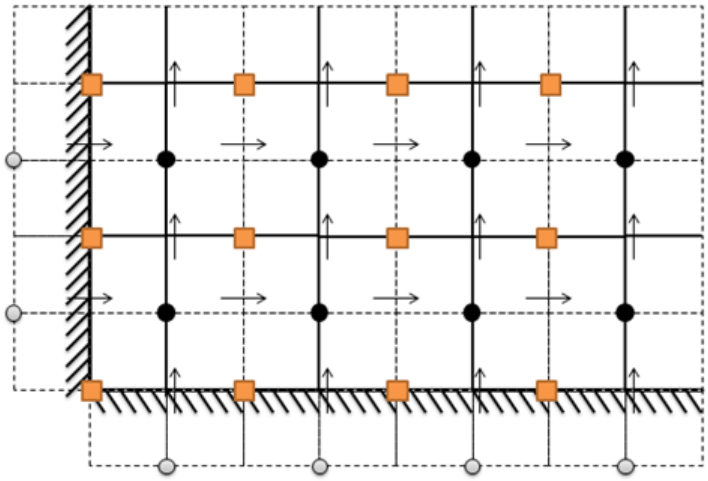

Figure 3.4. Nodes on the structured grid. Number density and momentum equations are solved using the staggered grid alignment.

are to be found in [38].

Two interger indices, (i, j), are used to locate a node on the staggered grid for each parameter. Knowing these two indices, Δr, Δz, and the type of the parameter (axial, radial vector components or scalar) allows for locating the node in the r-z plane. It is also necessary to convert the two-index address to a one-index type of address for implementation purposes. Therefore a third index, k, is introduced. The calculation of k depends on which of the axial, radial vector components or scalar grids is under consideration. For axial vector components this third index is named as ku, whereas it is kv for radial vector components, and kp for the scalars. These indices are calculated as:

$$kp = j(nz+1)+i \tag{3.108}$$

$$ku = j(nz)+i \tag{3.109}$$

$$kv = j(nz+1)+i \tag{3.110}$$

The control volumes used in the numerical formulation depends also on the type of the parameter under consideration. The structured staggered grid produces different control volumes for each of the parameters, u, v, and n. Figure 3.5 represents the

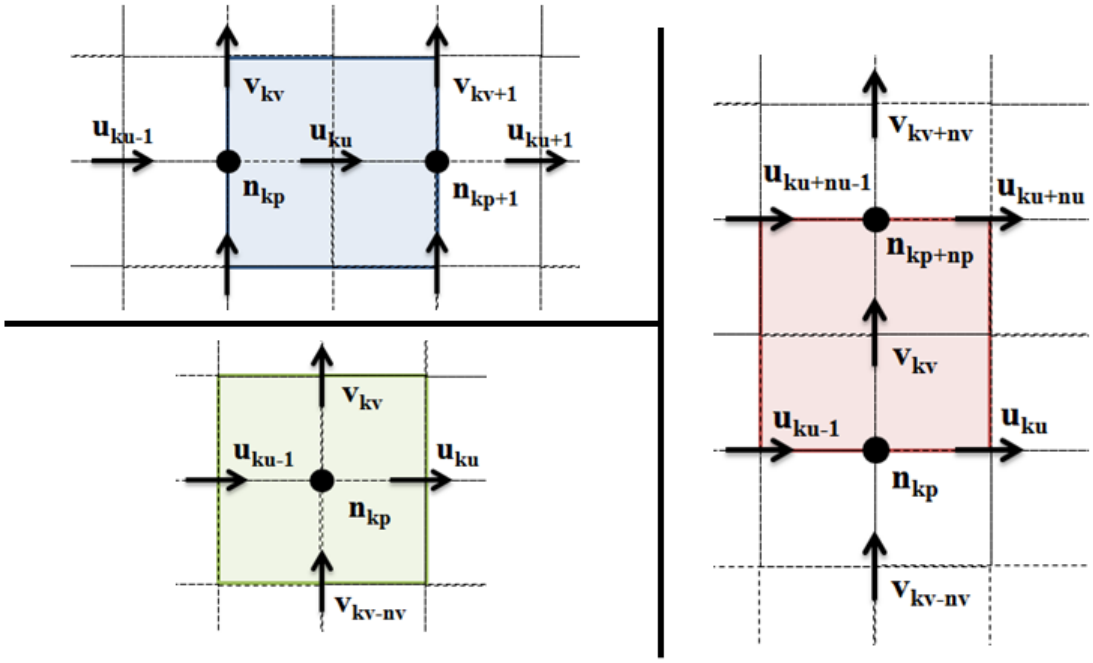

Figure 3.5. Control volumes for axial and radial velocities, and number density. Left top shows the control volume for axial velocity, whereas left bottom is for number density and right is for the radial velocity.

neighboring parameters and their indices for the three control volume types. In this formulation nu, nv, and np represents the number of nodes in the axial direction for axial velocity, radial velocity, and the number density, respectively.

The finite volume method starts with writing the momentum equations in radial and axial directions. Here the application of the method for ions is demonstrated. It is straightforward to apply the same scheme to neutrals.

Before writing these equations in radial and axial directions, some terms in these equations should be elaborated. The Lorentz force ($\mathbf{v} \times \mathbf{B}$) is expanded as:

$$\mathbf{v} \times \mathbf{B} = \begin{vmatrix} \hat{\mathbf{r}} & \hat{\theta} & \hat{\mathbf{z}} \\ v & w & u \\ B_r & 0 & B_z \end{vmatrix} = (wB_z)\hat{\mathbf{r}} - (vB_z - uB_r)\hat{\theta} + (-wB_r)\hat{\mathbf{z}}$$

Convective terms in the momentum equation need also to be elaborated. The expression, $\mathbf{v}\cdot\nabla\mathbf{v}$ in cylindrical coordinates:

$$\mathbf{v}\cdot\nabla\mathbf{v} = \begin{bmatrix} v\frac{\partial v}{\partial r} + \frac{w}{r}\frac{\partial v}{\partial \theta} - \frac{w^2}{r} + u\frac{\partial v}{\partial z} \\ \\ v\frac{\partial w}{\partial r} + \frac{w}{r}\frac{\partial w}{\partial \theta} + \frac{vw}{r} + u\frac{\partial w}{\partial z} \\ \\ v\frac{\partial u}{\partial r} + \frac{w}{r}\frac{\partial u}{\partial \theta} + u\frac{\partial u}{\partial z} \end{bmatrix}$$

where the velocity vector is defined as:

$$\mathbf{v}(r,\theta,z) = (v(r,z), w(r,z), u(r,z)) \tag{3.111}$$

Using these identities, the ion momentum Equation 3.53 takes the form in axial direction:

$$m_i n_i \left(\frac{\partial u_i}{\partial t} + u_i\frac{\partial u_i}{\partial z} + v_i\frac{\partial u_i}{\partial r}\right) = -kT_i\frac{\partial n_i}{\partial z} + en_iE_z - en_iw_iB_r - m_in_i\nu_{in}(u_i - u_n) \tag{3.112}$$

where the forcing term due to electron-ion collisions is neglected due to the small mass of electrons. Similarly in radial direction:

$$m_i n_i \left(\frac{\partial v_i}{\partial t} + u_i\frac{\partial v_i}{\partial z} + v_i\frac{\partial v_i}{\partial r} - \frac{w_i^2}{r}\right) = -kT_i\frac{\partial n_i}{\partial r} + en_iE_r + en_iw_iB_z - m_in_i\nu_{in}(v_i - v_n) \tag{3.113}$$

Here it is also appropriate to present the neutral momentum equation in the two radial coordinate system directions. Neutral momentum equation in axial direction:

$$m_n n_n \left(\frac{\partial u_n}{\partial t} + u_n\frac{\partial u_n}{\partial z} + v_n\frac{\partial u_n}{\partial r}\right) = -kT_n\frac{\partial n_n}{\partial z} + m_in_i\nu_{in}(u_i - u_n) \tag{3.114}$$

This expression is much simpler than 3.112 because there is no electromagnetic force

applied on neutral particles. Similarly, neutral momentum equation in radial direction:

$$m_n n_n \left(\frac{\partial v_n}{\partial t} + u_n \frac{\partial v_n}{\partial z} + v_n \frac{\partial v_n}{\partial r} - \frac{w_n^2}{r} \right) = -kT_n \frac{\partial n_n}{\partial r} + m_n n_i \nu_{in} (v_i - v_n) \tag{3.115}$$

The finite volume formulation of these equations are written by integrating each parameter over the control volume. The left hand side of the ion momentum equation in axial direction 3.112 can be expressed as:

$$m_i n_i \frac{u_i - u_i^o}{\Delta t} \Delta V + (m_i n_i u_i^* u_i A)_e - (m_i n_i u_i^* u_i A)_w + (m_i n_i v_i^* u_i A)_n - (m_i n_i v_i^* u_i A)_s \tag{3.116}$$

where the convected parameter is the axial velocity, u_i, and the subscripts of the brackets denote the location of the cell faces. u_i^o denotes the axial ion velocity from the previous time step. The superscript (*) of the velocity components denote the values from the initial guess for the particular time step. For convenience, the following naming is introduced:

$$F_e = (m_i n_i u_i^* A)_e \quad F_w = (m_i n_i u_i^* A)_w \quad F_n = (m_i n_i v_i^* A)_n \quad F_s = (m_i n_i v_i^* A)_s \tag{3.117}$$

where the velocity values, u_i and v_i in these equalities come from the previous iteration. These values are calculated according to the neighboring parameters shown in Figure 3.5:

$$F_e = m \frac{1}{2} \left[\left(\frac{n_{kp+1} + n_{kp+2}}{2} \right) u_{ku+1}^* + \left(\frac{n_{kp} + n_{kp+1}}{2} \right) u_{ku}^* \right] A_e \tag{3.118}$$

$$F_w = m \frac{1}{2} \left[\left(\frac{n_{kp} + n_{kp+1}}{2} \right) u_{ku}^* + \left(\frac{n_{kp} + n_{kp-1}}{2} \right) u_{ku-1}^* + \right] A_w \tag{3.119}$$

$$F_n = m \frac{1}{2} \left[\left(\frac{n_{kp} + n_{kp+np}}{2} \right) v_{kv} + \left(\frac{n_{kp+1} + n_{kp+np+1}}{2} \right) v_{kv+1}^* \right] A_n \tag{3.120}$$

$$F_s = m \frac{1}{2} \left[\left(\frac{n_{kp} + n_{kp-np}}{2} \right) v_{kv-nv} + \left(\frac{n_{kp+1} + n_{kp+1-np}}{2} \right) v_{kv-nv+1}^* \right] A_s \tag{3.121}$$

The convected parameters, $(u_i)_e$, $(u_i)_w$, $(u_i)_n$, and $(u_i)_s$ can be discretized according to various differencing schemes. In this work, the central differencing approach [38] is

obtained:

$$(u_i)_e = \frac{u_{ku} + u_{ku+1}}{2}, \qquad (u_i)_w = \frac{u_{ku-1} + u_{ku}}{2} \tag{3.122}$$

$$(u_i)_n = \frac{u_{ku} + u_{ku+nu}}{2}, \qquad (u_i)_s = \frac{u_{ku-nu} + u_{ku}}{2} \tag{3.123}$$

After inserting these expressions into the expression 3.116 becomes:

$$m_i n_i \frac{u_{ku} - u^o_{ku}}{\Delta t}\Delta V + \frac{F_e}{2}(u_{ku}+u_{ku+1}) - \frac{F_w}{2}(u_{ku-1}+u_{ku}) + \frac{F_n}{2}(u_{ku}+u_{ku+nu}) - \frac{F_s}{2}(u_{ku-nu}+u_{ku}) \tag{3.124}$$

The right hand side of the axial momentum Equation 3.112 can be discretized as:

$$\left(-kT_i\frac{n_{kp+1} - n_{kp}}{\Delta z} + en_{ku}\frac{\phi_{kp} - \phi_{kp+1}}{\Delta z} - en_{ku}w_{ku}B_{r(ku)} - m_i n_{ku}\nu_{in}(u_{ku} - u_{n(ku)})\right)\Delta V \tag{3.125}$$

where the ku subscript for parameters other than the axial velocity denotes their interpolation to the location of the axial velocity. For the convenience of applying the SIMPLE algorithm, the coefficients will be written in the form of:

$$a_{ku}u_{ku} = a_{ku+1}u_{ku+1} + a_{ku-1}u_{ku-1} + a_{ku+nu}u_{ku+nu} + a_{ku-nu}u_{ku-nu} + b_{source} \tag{3.126}$$

where b_{source} denotes the source terms that do not include the axial velocity term and a terms represent the coefficients in front of the velocity components. Coupling both the left hand side and right hand side discretizations, the coefficients for the velocity components are written as:

$$a_{ku+1} = -\frac{F_e}{2} \qquad a_{ku-1} = \frac{F_w}{2} \qquad a_{ku+nu} = -\frac{F_n}{2} \qquad a_{ku-nu} = \frac{F_s}{2} \tag{3.127}$$

and the center coefficient is formulated as:

$$a_{ku} = \frac{F_e}{2} - \frac{F_w}{2} + \frac{F_n}{2} - \frac{F_s}{2} + m_i n_{ku}\frac{\Delta V}{\Delta t} + m_i n_{ku}\nu_{in}\Delta V \tag{3.128}$$

These 5 coefficients build up the coefficient matrix. The source term is formulated as

follows:

$$b_{source} = \left(-kT_i \frac{n_{kp+1} - n_{kp}}{\Delta z} + en_{ku} \frac{\phi_{kp} - \phi_{kp+1}}{\Delta z} - en_{ku} w_{ku} B_{r(ku)} + m_i n_{ku} \nu_{in} u_{n(ku)} \right) \Delta V \tag{3.129}$$

The axial momentum equation is solved using these coefficients. A very similar formulation can be performed for the radial momentum equation. The left hand side of the momentum equation in radial direction 3.113 can be written as:

$$m_i n_i \frac{v_i - v_i^o}{\Delta t} \Delta V + (m_i n_i u_i^* v_i A)_e - (m_i n_i u_i^* v_i A)_w + (m_i n_i v_i^* v_i A)_n - (m_i n_i v_i^* v_i A)_s \tag{3.130}$$

The same naming detailed in 3.117 is again performed for the radial direction. This time parameters are defined as:

$$F_e = m \frac{1}{2} \left[\left(\frac{n_{kp} + n_{kp+1}}{2} \right) u_{ku}^* + \left(\frac{n_{kp+np} + n_{kp+np+1}}{2} \right) u_{ku+nu}^* \right] A_e \tag{3.131}$$

$$F_w = m \frac{1}{2} \left[\left(\frac{n_{kp} + n_{kp-1}}{2} \right) u_{ku-1}^* + \left(\frac{n_{kp+np} + n_{kp+np-1}}{2} \right) u_{ku+nu-1}^* \right] A_w \tag{3.132}$$

$$F_n = m \frac{1}{2} \left[\left(\frac{n_{kp+np} + n_{kp+2np}}{2} \right) v_{kv+nv} + \left(\frac{n_{kp} + n_{kp+np}}{2} \right) v_{kv}^* \right] A_n \tag{3.133}$$

$$F_s = m \frac{1}{2} \left[\left(\frac{n_{kp} + n_{kp+np}}{2} \right) v_{kv} + \left(\frac{n_{kp} + n_{kp-np}}{2} \right) v_{kv-nv}^* \right] A_s \tag{3.134}$$

The convected parameters, $(v_i)_e$, $(v_i)_w$, $(v_i)_n$, and $(v_i)_s$ can be discretized according to various differencing schemes. In this work, the central differencing approach [38] is obtained:

$$(v_i)_e = \frac{v_{kv} + v_{kv+1}}{2}, \qquad (v_i)_w = \frac{v_{kv-1} + v_{kv}}{2} \tag{3.135}$$

$$(v_i)_n = \frac{v_{kv} + v_{kv+nv}}{2}, \qquad (v_i)_s = \frac{v_{kv-nv} + v_{kv}}{2} \tag{3.136}$$

After inserting these expressions into the expression 3.130 becomes:

$$m_i n_i \frac{v_{kv} - v_{kv}^o}{\Delta t} \Delta V + \frac{F_e}{2}(v_{kv} + v_{kv+1}) - \frac{F_w}{2}(v_{kv-1} + v_{kv}) + \frac{F_n}{2}(v_{kv} + v_{kv+nv}) - \frac{F_s}{2}(v_{kv-nv} + v_{kv}) \tag{3.137}$$

The right hand side of the radial momentum Equation 3.113 can be discretized as:

$$\left(-kT_i\frac{n_{kp+np}-n_{kp}}{\Delta r}+en_{kv}\frac{\phi_{kp}-\phi_{kp+np}}{\Delta r}+en_{kv}w_{kv}B_{z(kv)}-m_in_{kv}\nu_{in}(v_{kv}-v_{n(kv)})+\frac{w_{kv}^2}{r_{kv}}\right)\Delta V \tag{3.138}$$

where the kv subscript for parameters other than the radial velocity denotes their interpolation to the location of the radial velocity. For the convenience of applying the SIMPLE algorithm, the coefficients will be written in the form of:

$$a_{kv}v_{kv}=a_{kv+1}v_{kv+1}+a_{kv-1}v_{kv-1}+a_{kv+nv}v_{kv+nv}+a_{kv-nv}v_{kv-nv}+b_{source} \tag{3.139}$$

where b_{source} denotes the source terms that do not include the radial velocity term and a terms represent the coefficients in front of the radial velocity components. Coupling both the left hand side and right hand side discretizations, the coefficients for the radial velocity component are written as:

$$a_{kv+1}=-\frac{F_e}{2}\qquad a_{kv-1}=\frac{F_w}{2}\qquad a_{kv+nv}=-\frac{F_n}{2}\qquad a_{kv-nv}=\frac{F_s}{2} \tag{3.140}$$

and the center coefficient is formulated as:

$$a_{kv}=\frac{F_e}{2}-\frac{F_w}{2}+\frac{F_n}{2}-\frac{F_s}{2}+m_in_{kv}\frac{\Delta V}{\Delta t}+m_in_{kv}\nu_{in}\Delta V \tag{3.141}$$

These 5 coefficients build up the coefficient matrix. The source term is formulated as follows:

$$b_{source}=\left(-kT_i\frac{n_{kp+np}-n_{kp}}{\Delta r}+en_{kv}\frac{\phi_{kp}-\phi_{kp+np}}{\Delta r}+en_{kv}w_{kv}B_{z(kv)}+\frac{w_{kv}^2}{r_{kv}}+m_in_{kv}\nu_{in}v_{n(kv)}\right)\Delta V \tag{3.142}$$

The equations for neutral momentum is discretized with the same procedure here, therefore their discretization will not be shown. The next step is to formulate the

continuity equation, which is the heart of the SIMPLE algorithm.

The ion continuity Equation 3.50 is extended in cylindrical coordinates as follows:

$$\frac{\partial n_i}{\partial t} + \frac{\partial (n_i u_i)}{\partial z} + \frac{1}{r}\frac{\partial (n_i r v_i)}{\partial r} = \dot{R} \tag{3.143}$$

which can be also written as:

$$\frac{1}{r}\frac{\partial (n_i r)}{\partial t} + \frac{1}{r}\frac{\partial (n_i r u_i)}{\partial z} + \frac{1}{r}\frac{\partial (n_i r v_i)}{\partial r} = \dot{R} \tag{3.144}$$

and multiplying both sides with r yields:

$$\frac{\partial (n_i r)}{\partial t} + \frac{\partial (n_i r u_i)}{\partial z} + \frac{\partial (n_i r v_i)}{\partial r} = r\dot{R} \tag{3.145}$$

Finite volume discretization of the equation given above is:

$$\left(\frac{\partial (n_i r)}{\partial t}\right)_V + (n_i r u_i A)_e - (n_i r u_i A)_w + (n_i r v_i A)_n - (n_i r v_i A)_s = \left(r\dot{R}\right)_V \tag{3.146}$$

For simplicity, u, v and n are used during the following discussion instead of u_i, v_i and n_i.

In this step it is appropriate to introduce the logic of the SIMPLE algorithm. The first step of the SIMPLE algorithm is formulating the variables to be found into two components:

$$u = u^* + u' \tag{3.147}$$

$$v = v^* + v' \tag{3.148}$$

$$n = n^* + n' \tag{3.149}$$

where the superscript (*) denotes the component, which is guessed or calculated from the guessed initial conditions. The other superscript ($'$) denotes the corrector compo-

nent. The algorithm starts with solving the discretized momentum equations with the guessed number density field, n^*. The acquired solution fields are denoted as u^* and v^*. To derive the correction terms, subtracting the solution of the momentum equations (u^* and v^*) using the guessed number density field (n^*) yields:

$$a_{ku}(u_{ku} - u^*_{ku}) = \sum a_{xy}(u_{xy} - u^*_{xy}) + (S_u - S^*_u)\Delta V \tag{3.150}$$

in axial direction. In radial direction:

$$a_{kv}(v_{kv} - v^*_{kv}) = \sum a_{xy}(v_{xy} - v^*_{xy}) + (S_v - S^*_v)\Delta V \tag{3.151}$$

When the corrections 3.147 are utilized, equations above become:

$$a_{ku}u'_{ku} = \sum a_{xy}u'_{xy} + S'_u\Delta V \tag{3.152}$$

$$a_{kv}v'_{kv} = \sum a_{xy}v'_{xy} + S'_v\Delta V \tag{3.153}$$

Main approximation of the SIMPLE algorithm is the omission of the summation term, which is the first term on the right hand side of the both equations. The SIMPLE algorithm relies on the assumption that the correction terms denoted with the summation sign are very small, especially as the algorithm converges to the actual solution. So the equations become:

$$a_{ku}u'_{ku} = S'_u\Delta V \tag{3.154}$$

$$a_{kv}v'_{kv} = S'_v\Delta V \tag{3.155}$$

where S'_u and S'_v terms are called as the correction terms for the axial and radial

velocities, respectively. The velocity corrections for ions are therefore formulated as:

$$u'_{ku} = \left[en'_{ku} \frac{\phi_w - \phi_e}{\Delta z} - en'_{ku} w_{ku} B_{r(ku)} - kT_i \frac{n'_{kp+1} - n'_{kp}}{\Delta z} + m_i n'_{ku} \nu_{in} v_{n(ku)} \right] \frac{\Delta V}{a_{ku}} \tag{3.156}$$

$$v'_{kv} = \left[en'_{kv} \frac{\phi_s - \phi_n}{\Delta r} + en'_{kv} w_{kv} B_{z(kv)} - kT_i \frac{n'_{kp+np} - n'_{kp}}{\Delta r} + m_i n'_{kv} \frac{w_{kv}^2}{r} + m_i n'_{kv} \nu_{in} v_{n(kv)} \right] \frac{\Delta V}{a_{kv}} \tag{3.157}$$

With these formulations velocity corrections are expressed in terms of number density corrections. Here it is appropriate to explain the handling of the continuity equation in the scope of the SIMPLE algorithm. Continuity equation serves as the number density correction equation in the model presented here. Terms in the continuity equation are written in terms of the number density corrections. The terms included in the discretized Equation 3.146 can be written in terms of the number density corrections as follows [40]:

$$(nruA) = (n^* + n')r(u^* + u')A = n^* r u^* A + n^* r u' A + n' r u^* A + n' r u' A \tag{3.158}$$

where u^*, v^* and n^* are known before the start of the iteration. The last term in the equation above, which contains the multiplication of number density and velocity corrections, is neglected assuming that this terms is small [40]. To calculate the neutral number density correction, the velocity corrections given in Equation 3.156 are plugged into the finite volume discretization formulated in Equation 3.146 and the coefficients are calculated.

Discretizations of the remaining equations solved in the model are presented in the remaining part of this section. These equations are:

- Ion continuity equation (Equation 3.50)
- Neutral continuity equation (Equation 3.52)
- Neutral momentum equation in axial direction (Equation 3.114)

- Neutral momentum equation in radial direction (Equation 3.115)
- Electron power balance equation (Equation 3.56)
- Electric potential equation (Equation 3.81)

3.4.1. Ion Continuity Equation

Ion continuity equation is formulated in Equation 3.50. For convenience, this equation is written here again:

$$\frac{\partial n_i}{\partial t} + \nabla\cdot\left(n_i \mathbf{v}_i\right) = \dot{R}_i$$

whose finite volume discretization is given in 3.146:

$$\left(\frac{\partial (n_i r)}{\partial t}\right)_V + (n_i r u_i A)_e - (n_i r u_i A)_w + (n_i r v_i A)_n - (n_i r v_i A)_s = \left(r\dot{R}\right)_V$$

Using the expansion formulated in Equation 3.158, the discretization for the continuity equation is performed. As stated in Section 3.4, the continuity equations are used to solve the number density corrections that are used to correct the initial number density guess, which generally comes from the previous iteration. The first term on the left hand side, the transient term, can be discretized as:

$$\frac{n^*_{i,kp} + n'_{i,kp} - n^o_{i,kp}}{\Delta t} r \Delta V$$

The second, third, fourth and fifth terms, which denote the fluxes passing through the four boundaries of the control volume, are expanded as:

$$(n_i r u_i A)_e = n^*_{i,ku} u^*_{i,ku} r A_h + n^*_{i,ku} u'_{i,ku} r A_h + n'_{i,ku} u^*_{i,ku} r A_h$$
$$(n_i r u_i A)_w = n^*_{i,ku-1} u^*_{i,ku-1} r A_h + n^*_{i,ku-1} u'_{i,ku-1} r A_h + n'_{i,ku} u^*_{i,ku-1} r A_h$$
$$(n_i r v_i A)_n = n^*_{i,kv} v^*_{i,kv} r_n A_n + n^*_{i,kv} v'_{i,kv} r_n A_n + n'_{i,kv} v^*_{i,kv} r_n A_n$$
$$(n_i r v_i A)_s = n^*_{i,kv-nv} v^*_{i,kv-nv} r_s A_s + n^*_{i,kv-nv} v'_{i,kv-nv} r_s A_s + n'_{i,kv-nv} v^*_{i,kv-nv} r_s A_s$$

where the velocity correction terms, u', need to be defined as well. These terms are formulated as:

$$u'_{i,ku} = \left(eT_i \frac{n'_{kp} - n'_{kp+1}}{\Delta z} + n'_{i,ku} e \frac{\phi_{kp} - \phi_{kp+1}}{\Delta z} \right) \frac{r\Delta V}{a_{P,ku}}$$
$$u'_{i,ku-1} = \left(eT_i \frac{n'_{kp-1} - n'_{kp}}{\Delta z} + n'_{i,ku-1} e \frac{\phi_{kp-1} - \phi_{kp}}{\Delta z} \right) \frac{r\Delta V}{a_{P,ku-1}}$$
$$v'_{i,kv} = \left(eT_i \frac{n'_{kp} - n'_{kp+np}}{\Delta r} + n'_{i,kv} e \frac{\phi_{kp} - \phi_{kp+np}}{\Delta z} + m_i n'_{i,kv} \frac{w^2_{i,kv}}{r} \right) \frac{r\Delta V}{a_{P,kv}}$$
$$v'_{i,kv-nv} = \left(eT_i \frac{n'_{kp-np} - n'_{kp}}{\Delta r} + n'_{i,kv-nv} e \frac{\phi_{kp-np} - \phi_{kp}}{\Delta z} + m_i n'_{i,kv-nv} \frac{w^2_{i,kv-nv}}{r} \right) \frac{r\Delta V}{a_{P,kv}}$$

where $a_{P,ku}$ is the center coefficient for the ion momentum equation in axial direction, and it is formulated as given in 3.128. Similarly, the center coefficient for the ion momentum equation in radial direction, $a_{P,kv}$, is fomulated as given in 3.141.

The right hand side of the ion continuity equation represents the particle generation rate which is caused by ionization. This term is discretized as:

$$n_{n,kp} n_{e,kp} \langle \mathbf{v}_e Q_{ion} \rangle \, r\Delta V$$

Here it should be emphasized that the number densities evaluated on the velocity nodes are linear interpolations of the neighboring number density nodes:

$$n'_{i,ku} = \frac{n'_{i,kp} + n'_{i,kp+1}}{2} \qquad n'_{i,ku-1} = \frac{n'_{i,kp-1} + n'_{i,kp}}{2}$$
$$n'_{i,kv} = \frac{n'_{i,kp} + n'_{i,kp+np}}{2} \qquad n'_{i,kv-nv} = \frac{n'_{i,kp-np} + n'_{i,kp}}{2}$$

These identities and the discretizations given above result in the following coefficients

for the coefficient matrix:

$$a_N = \frac{1}{2}v_{i,kv}r_nA_n - n^*_{i,kv}r_nA_n\frac{r_n\Delta V}{a_{P,kv}}\left(\frac{eT_i}{\Delta r} - e\frac{\phi_{kp}-\phi_{kp+np}}{2\Delta r} - \frac{1}{2}\frac{m_iw^2_{i,kv}}{r}\right)$$
$$a_S = -\frac{1}{2}v_{i,kv-nv}r_sA_s - n^*_{i,kv-nv}r_sA_s\frac{r_s\Delta V}{a_{P,kv-nv}}\left(\frac{eT_i}{\Delta r} + e\frac{\phi_{kp-np}-\phi_{kp}}{2\Delta r} + \frac{1}{2}\frac{m_iw^2_{i,kv-nv}}{r}\right)$$
$$a_E = \frac{1}{2}u_{i,ku}rA_h - n^*_{i,ku}rA_h\frac{r\Delta V}{a_{P,ku}}\left(\frac{eT_i}{\Delta z} - e\frac{\phi_{kp}-\phi_{kp+1}}{2\Delta z}\right)$$
$$a_W = \frac{1}{2}u_{i,ku-1}rA_h - n^*_{i,ku-1}rA_h\frac{r\Delta V}{a_{P,ku-1}}\left(\frac{eT_i}{\Delta z} + e\frac{\phi_{kp-1}-\phi_{kp}}{2\Delta z}\right)$$

and the central coefficient is:

$$a_P = -\frac{1}{2}u_{i,ku-1}rA_h + \frac{1}{2}u_{i,ku}rA_h + \frac{1}{2}v_{i,kv}r_nA_n - \frac{1}{2}v_{i,kv-nv}r_sA_s + n^*_{i,ku-1}rA_h\frac{r\Delta V}{a_{P,ku-1}}\left(\frac{eT_i}{\Delta z}\right.$$
$$\left.-e\frac{\phi_{kp-1}-\phi_{kp}}{2\Delta z}\right) + n^*_{i,ku}rA_h\frac{r\Delta V}{a_{P,ku}}\left(\frac{eT_i}{\Delta z} + e\frac{\phi_{kp}-\phi_{kp+1}}{2\Delta z}\right) + n^*_{i,kv}r_nA_n\frac{r_n\Delta V}{a_{P,kv}}\left(\frac{eT_i}{\Delta r}+\right.$$
$$\left.e\frac{\phi_{kp}-\phi_{kp+np}}{2\Delta r} + \frac{1}{2}\frac{m_iw^2_{i,kv}}{r}\right) + n^*_{i,kv-nv}r_sA_s\frac{r_s\Delta V}{a_{P,kv-nv}}\left(-\frac{1}{2}\frac{m_iw^2_{i,kv-nv}}{r} - e\frac{\phi_{kp-np}-\phi_{kp}}{2\Delta r}+\right.$$
$$\left.+\frac{eT_i}{\Delta r}\right) + \frac{r\Delta V}{\Delta t}$$

The remaining terms are handled as the source term that builds up the right hand side of the linear system. The source term is formulated as:

$$b_{source} = n^*_{i,ku-1}u^*_{i,ku-1}rA_h - n^*_{i,ku}u^*_{i,ku}rA_h + n^*_{i,kv-nv}v^*_{i,kv-nv}r_sA_s - n^*_{i,kv}v^*_{i,kv}r_nA_n -$$
$$r\Delta V\frac{n^*_{i,kp}-n^o_{i,kp}}{\Delta t} + n_{n,kp}n_{e,kp}\left\langle \mathbf{v}_eQ_{ion}\right\rangle r\Delta V$$

3.4.2. Neutral Continuity Equation

Neutral continuity equation is formulated in Equation 3.52. For convenience, this equation is written here again:

$$\frac{\partial n_n}{\partial t} + \nabla\cdot(n_n\mathbf{v}_n) = -\dot{R}_i$$

whose finite volume discretization can be formulated very similar to 3.146:

$$\left(\frac{\partial(n_n r)}{\partial t}\right)_V + (n_n r u_n A)_e - (n_n r u_n A)_w + (n_n r v_n A)_n - (n_n r v_n A)_s = -\left(r\dot{R}\right)_V$$

For the neutral continuity equation, almost exact steps and expansions are used as the ones presented for the ion continuity equation in the previous section. According to these same guidelines, the transient term on the left hand side is discretized as:

$$\frac{n^*_{n,kp} + n'_{n,kp} - n^o_{n,kp}}{\Delta t} r \Delta V$$

The second, third, fourth and fifth terms, which denote the fluxes passing through the four boundaries of the control volume, are expanded as:

$$(n_n r u_n A)_e = n^*_{n,ku} u^*_{n,ku} r A_h + n^*_{n,ku} u'_{n,ku} r A_h + n'_{n,ku} u^*_{n,ku} r A_h$$
$$(n_n r u_n A)_w = n^*_{n,ku-1} u^*_{n,ku-1} r A_h + n^*_{n,ku-1} u'_{n,ku-1} r A_h + n'_{n,ku} u^*_{n,ku-1} r A_h$$
$$(n_n r v_n A)_n = n^*_{n,kv} v^*_{n,kv} r_n A_n + n^*_{n,kv} v'_{n,kv} r_n A_n + n'_{n,kv} v^*_{n,kv} r_n A_n$$
$$(n_n r v_n A)_s = n^*_{n,kv-nv} v^*_{n,kv-nv} r_s A_s + n^*_{n,kv-nv} v'_{n,kv-nv} r_s A_s + n'_{n,kv-nv} v^*_{n,kv-nv} r_s A_s$$

where the velocity correction terms, u', need to be defined as well. These terms are formulated as:

$$u'_{n,ku} = \left(eT_n \frac{n'_{kp} - n'_{kp+1}}{\Delta z}\right) \frac{r\Delta V}{a_{P,ku}}$$
$$u'_{n,ku-1} = \left(eT_n \frac{n'_{kp-1} - n'_{kp}}{\Delta z}\right) \frac{r\Delta V}{a_{P,ku-1}}$$
$$v'_{n,kv} = \left(eT_i \frac{n'_{kp} - n'_{kp+np}}{\Delta r} + m_n n'_{n,kv} \frac{w^2_{n,kv}}{r}\right) \frac{r\Delta V}{a_{P,kv}}$$
$$v'_{n,kv-nv} = \left(eT_i \frac{n'_{kp-np} - n'_{kp}}{\Delta r} + m_n n'_{n,kv-nv} \frac{w^2_{n,kv-nv}}{r}\right) \frac{r\Delta V}{a_{P,kv}}$$

where $a_{P,ku}$ is the center coefficient for the neutral momentum equation in axial direction 3.159, and $a_{P,kv}$ is the center coefficient for the neutral momentum equation in radial direction 3.161.

The right hand side of the neutral continuity equation represents the loss of neutral particles due to ionization. This term is discretized as:

$$n_{n,kp} n_{e,kp} \langle \mathbf{v}_e Q_{ion} \rangle \, r \Delta V$$

As it is the case with the ion continuity equation, it should be emphasized that the number densities evaluated on the velocity nodes are linear interpolations of the neighboring number density nodes:

$$n'_{n,ku} = \frac{n'_{n,kp} + n'_{n,kp+1}}{2} \qquad n'_{n,ku-1} = \frac{n'_{n,kp-1} + n'_{n,kp}}{2}$$
$$n'_{n,kv} = \frac{n'_{n,kp} + n'_{n,kp+np}}{2} \qquad n'_{n,kv-nv} = \frac{n'_{n,kp-np} + n'_{n,kp}}{2}$$

These identities and the discretizations given above result in the following coefficients for the coefficient matrix:

$$a_N = \frac{1}{2} v_{n,kv} r_n A_n - n^*_{n,kv} r_n A_n \frac{r_n \Delta V}{a_{P,kv}} \left(\frac{eT_n}{\Delta r} - \frac{1}{2} \frac{m_n w^2_{n,kv}}{r} \right)$$
$$a_S = -\frac{1}{2} v_{n,kv-nv} r_s A_s - n^*_{n,kv-nv} r_s A_s \frac{r_s \Delta V}{a_{P,kv-nv}} \left(\frac{eT_n}{\Delta r} + \frac{1}{2} \frac{m_i w^2_{i,kv-nv}}{r} \right)$$
$$a_E = \frac{1}{2} u_{n,ku} r A_h - n^*_{n,ku} r A_h \frac{r \Delta V}{a_{P,ku}} \frac{eT_n}{\Delta z}$$
$$a_W = \frac{1}{2} u_{n,ku-1} r A_h - n^*_{n,ku-1} r A_h \frac{r \Delta V}{a_{P,ku-1}} \frac{eT_n}{\Delta z}$$

and the central coefficient is:

$$\begin{aligned} a_P = -\frac{1}{2} u_{n,ku-1} r A_h + \frac{1}{2} u_{n,ku} r A_h + \frac{1}{2} v_{n,kv} r_n A_n - \frac{1}{2} v_{n,kv-nv} r_s A_s + n^*_{n,ku} r A_h \frac{r \Delta V}{a_{P,ku}} \frac{eT_i}{\Delta z} \\ + n^*_{n,ku-1} r A_h \frac{r \Delta V}{a_{P,ku-1}} \frac{eT_n}{\Delta z} + n^*_{n,kv} r_n A_n \frac{r_n \Delta V}{a_{P,kv}} \left(\frac{eT_n}{\Delta r} + \frac{1}{2} \frac{m_n w^2_{n,kv}}{r} \right) \\ + n^*_{n,kv-nv} r_s A_s \frac{r_s \Delta V}{a_{P,kv-nv}} \left(-\frac{1}{2} \frac{m_i w^2_{i,kv-nv}}{r} + \frac{eT_i}{\Delta r} \right) + \frac{r \Delta V}{\Delta t} \end{aligned}$$

The remaining terms are handled as the source term that builds up the right hand side

of the linear system. The source term is formulated as:

$$b_{source} = n^*_{n,ku-1}u^*_{n,ku-1}rA_h - n^*_{n,ku}u^*_{n,ku}rA_h + n^*_{n,kv-nv}v^*_{n,kv-nv}r_sA_s - n^*_{n,kv}v^*_{n,kv}r_nA_n - r\Delta V\frac{n^*_{n,kp} - n^o_{n,kp}}{\Delta t} - n_{n,kp}n_{e,kp}\langle \mathbf{v}_e Q_{ion}\rangle r\Delta V$$

3.4.3. Neutral Momentum Equation in Axial Direction

The discretization of the momentum equation in axial direction for ions is represented before in Section 3.4. The formulation here follows the same procedure, but neutral momentum equation is relatively simpler because there is no Lorentz force acting on neutral particles.

The neutral momentum equation in axial direction is formulated in Equation 3.114. Here for convenience, this equation is written again:

$$m_n n_n\left(\frac{\partial u_n}{\partial t} + u_n\frac{\partial u_n}{\partial z} + v_n\frac{\partial u_n}{\partial r}\right) = -kT_n\frac{\partial n_n}{\partial z} + m_i n_i \nu_{in}(u_i - u_n)$$

The discretization of the left hand side of this equation is identical to 3.116. The right hand side of this equation can be discretized as:

$$\left(-kT_n\frac{n_{kp+1} - n_{kp}}{\Delta z} + m_i n_{ku}\nu_{in}(u_{i(ku)} - u_{ku})\right)\Delta V$$

In the form that is given in 3.126, the coefficients a_{ku+1}, a_{ku-1}, a_{ku+nu}, and a_{ku-nu} are formulated as the same given in 3.127. The center coefficient is formulated as:

$$a_{ku} = \frac{F_e}{2} - \frac{F_w}{2} + \frac{F_n}{2} - \frac{F_s}{2} + m_n n_{ku}\frac{\Delta V}{\Delta t} + m_i n_{ku}\nu_{in}\Delta V \tag{3.159}$$

The linear system is completed with the right hand side, which is formulated as:

$$b_{source} = \left(-kT_n\frac{n_{kp+1} - n_{kp}}{\Delta z} + m_i n_{ku}\nu_{in}u_{i(ku)}\right)\Delta V \tag{3.160}$$

3.4.4. Neutral Momentum Equation in Radial Direction

The neutral momentum equation in radial direction is formulated in Equation 3.115. Here for convenience, this equation is written again:

$$m_n n_n \left(\frac{\partial v_n}{\partial t} + u_n \frac{\partial v_n}{\partial z} + v_n \frac{\partial v_n}{\partial r} - \frac{w_n^2}{r} \right) = -kT_n \frac{\partial n_n}{\partial r} + m_i n_i \nu_{in} (v_i - v_n)$$

The discretization of the left hand side of this equation is identical to 3.130. The right hand side of this equation can be discretized as:

$$\left(-kT_n \frac{n_{kp+np} - n_{kp}}{\Delta r} + m_i n_{i,kv} \nu_{in} (v_{i(kv)} - v_{kv}) + \frac{w_{kv}^2}{r_{kv}} \right) \Delta V$$

In the form that is given in 3.139, the coefficients a_{kv+1}, a_{kv-1}, a_{kv+nv}, and a_{kv-nv} are formulated as the same given in 3.140. The center coefficient is formulated as:

$$a_{kv} = \frac{F_e}{2} - \frac{F_w}{2} + \frac{F_n}{2} - \frac{F_s}{2} + m_n n_{kv} \frac{\Delta V}{\Delta t} + m_i n_{kv} \nu_{in} \Delta V \tag{3.161}$$

The linear system is completed with the right hand side, which is formulated as:

$$b_{source} = \left(-kT_n \frac{n_{kp+np} - n_{kp}}{\Delta r} + \frac{w_{kv}^2}{r_{kv}} + m_i n_{kv} \nu_{in} v_{i(kv)} \right) \Delta V \tag{3.162}$$

3.4.5. Electron Power Balance Equation

Electron power balance equation is formulated in Equation 3.56. For convenience, this equation is written here again:

$$\frac{\partial}{\partial t} \left(\frac{3}{2} n_e e T_e \right) + \nabla \cdot \mathbf{Q}_e = -e \mathbf{E}_a \cdot \mathbf{\Gamma}_e + P_{dep} + P_{coll}$$

where the electron flux is calculated according to the drift-diffusion approximation 3.62, the electron thermal flux is calculated as given in 3.77, the ambipolar electric field is calculated as given in 3.74, the power deposition is calculated as given in 3.69, and the

power loss due to collisions is calculated as given in 3.72.

This equation is discretized according to the finite differencing scheme. The first term at the left hand side is discretized as:

$$\frac{3}{2}n_{e,kp}e\frac{T_{e,kp}-T^{o}_{e,kp}}{\Delta t}$$

The second term at the left hand side, electron heat flux term, is formulated as:

$$\nabla\cdot\mathbf{Q}_e=\frac{5}{2}eT_e\left(\frac{1}{r}\frac{\partial(r\Gamma_r)}{\partial r}+\frac{\partial\Gamma_z}{\partial z}\right)-\lambda_{th}\nabla^2T_e$$

This equation is discretized as:

$$\frac{5}{2}eT_{e,kp}\left(\frac{\Gamma_{r,kv}-\Gamma_{r,kv-nv}}{\Delta r}+\frac{\Gamma_{r,kp}}{r}+\frac{\Gamma_{z,ku}-\Gamma_{z,ku-1}}{\Delta z}\right)-\lambda_{th}\left(\frac{T_{e,kp+1}-2T_{e,kp}+T_{e,kp-1}}{\Delta z^2}+\frac{T_{e,kp+np}-2T_{e,kp}+T_{e,kp-np}}{\Delta r^2}+\frac{1}{r}\frac{T_{e,kp+np}-T_{e,kp-np}}{2\Delta r}\right)$$

The first term in the right hand side denotes the ambipolar field Joule heating. This term is formulated as:

$$-e\mathbf{E}_a\cdot\mathbf{\Gamma}_e=-e\left(-\frac{T_e}{n_e}\right)\left(\frac{\partial n_e}{\partial z}\Gamma_z+\frac{\partial n_e}{\partial r}\Gamma_r\right)$$

This equation is discretized as:

$$\frac{e}{n_{e,kp}}\left(\Gamma_{z,kp}\frac{n_{e,kp+1}-n_{e,kp-1}}{2\Delta z}+\Gamma_{r,kp}\frac{n_{e,kp+np}-n_{e,kp-np}}{2\Delta r}\right)T_{e,kp}$$

The second term at the right hand side denotes the power deposition into the plasma. This term is discretized as:

$$\frac{1}{2}\sigma_{p,kp}E^2_{\theta,kp}$$

The last term of this equation is the power loss due to collisions. This term is treated

as a source term and is discretized as:

$$n_{e,kp}n_{n,kp}e\left\langle \mathbf{v}_e Q_{ion}\right\rangle U_{ion} + n_{e,kp}n_{n,kp}e\left\langle \mathbf{v}_e Q_{exc}\right\rangle U_{exc} + 3\frac{m_e}{m_i}e(T_{e,kp} - T_{i,kp})\nu_{ei}n_{e,kp} + 3\frac{m_e}{m_i}e(T_{e,kp} - T_{n,kp})\nu_{en}n_{e,kp}$$

where the terms in the angled brackets are calculated as a function of temperature through an external function implemented into the code.

The discretizations given above result in the following coefficients for the coefficient matrix:

$$\begin{aligned} a_N &= -\lambda_{th}/\Delta r^2 - \frac{1}{2\Delta r}\lambda_{th}/r \\ a_S &= -\lambda_{th}/\Delta r^2 + \frac{1}{2\Delta r}\lambda_{th}/r \\ a_E &= -\lambda_{th}/\Delta z^2 \\ a_W &= -\lambda_{th}/\Delta z^2 \end{aligned}$$

and the central coefficient is:

$$a_P = \frac{3}{2}n_{e,kp}e\frac{1}{\Delta t} + \frac{5}{2}e\left(\frac{\Gamma_{r,kv} - \Gamma_{r,kv-nv}}{\Delta r} + \frac{\Gamma_{r,kp}}{r} + \frac{\Gamma_{z,ku} - \Gamma_{z,ku-1}}{\Delta z}\right) + 2\lambda_{th}/\Delta r^2 + 2\lambda_{th}/\Delta z^2 - \frac{e}{n_{e,kp}}\left(\Gamma_{z,kp}\frac{n_{e,kp+1} - n_{e,kp-1}}{2\Delta z} + \Gamma_{r,kp}\frac{n_{e,kp+np} - n_{e,kp-np}}{2\Delta r}\right) \tag{3.163}$$

The remaining terms are handled as the source term that builds up the right hand side of the linear system. The source term is formulated as:

$$b_{source} = \frac{3}{2}n_{e,kp}e\frac{T^o_{e,kp}}{\Delta t} + \frac{1}{2}\sigma_{p,kp}E^2_{\theta.kp} - n_{e,kp}n_{n,kp}e\left\langle \mathbf{v}_e Q_{ion}\right\rangle U_{ion} - n_{e,kp}n_{n,kp}e\left\langle \mathbf{v}_e Q_{exc}\right\rangle U_{exc} - 3\frac{m_e}{m_i}e(T_{e,kp} - T_{i,kp})\nu_{ei}n_{e,kp} - 3\frac{m_e}{m_i}e(T_{e,kp} - T_{n,kp})\nu_{en}n_{e,kp} \tag{3.164}$$

3.4.6. Electric Potential Equation

Electric potential equation is formulated in Equation 3.81. For convenience, this equation is written here again:

$$\nabla\cdot(\sigma\nabla\phi) = e\nabla\cdot(n_e\mathbf{v}_i) + \nabla\cdot\left(\frac{ek}{m_e\nu_{elastic}}\nabla(T_e n_e)\right) + \nabla\cdot(\sigma(v_{e,\theta}\times\mathbf{B}))$$

where the cross-product of the electron velocity and the magnetic field is evaluated as:

$$\mathbf{v}\times\mathbf{B} = \begin{vmatrix} \hat{\mathbf{r}} & \hat{\theta} & \hat{\mathbf{z}} \\ v_r & v_\theta & v_z \\ B_r & 0 & B_z \end{vmatrix} = (v_\theta B_z)\hat{\mathbf{r}} - (v_r B_z - v_z B_r)\hat{\theta} + (-v_\theta B_r)\hat{\mathbf{z}}$$

This relation will be used in the discretization of the last term of the electric potential equation. The term at the left hand side of this equation consists of the Laplace operator and discretized as:

$$\sigma_{p,kp}\left(\frac{\phi_{kp+np} - 2\phi_{kp} + \phi_{kp-np}}{\Delta r^2} + \frac{\phi_{kp+1} - 2\phi_{kp} + \phi_{kp-1}}{\Delta z^2} + \frac{1}{r}\frac{\phi_{kp+np} - \phi_{kp-np}}{2\Delta r}\right)$$

The first term at the right hand side is formulated as:

$$e\nabla\cdot(n_e\mathbf{v}_i) = e\left(\frac{\partial(n_e u_i)}{\partial z} + \frac{1}{r}\frac{\partial(r n_e v_i)}{\partial r}\right)$$

This equation is discretized as:

$$e\left(\frac{n_{e,ku}u_{i,ku} - n_{e,ku-1}u_{i,ku-1}}{\Delta z} + \frac{n_{e,kp}v_{i,kp}}{r_{kp}} + \frac{n_{e,kv}v_{i,kv} - n_{e,kv-nv}v_{i,kv-nv}}{\Delta r}\right)$$

The second term at the right hand side of the equation consists of the Laplacian of the multiplication of electron number density and temperature, $\nabla^2(T_e n_e)$. The

discretization of this term is:

$$\frac{ek}{m_e \nu_{elastic}} \left(\frac{n_{e,kp+1} T_{e,kp+1} - 2 n_{e,kp} T_{e,kp} + n_{e,kp-1} T_{e,kp-1}}{\Delta z^2} + \frac{n_{e,kp+np} T_{e,kp+np}}{2\Delta r} + \frac{n_{e,kp+np} T_{e,kp+np} - 2 n_{e,kp} T_{e,kp} + n_{e,kp-np} T_{e,kp-np}}{\Delta r^2} \right)$$

The last term of the electric potential equation includes the cross product of the magnetic field and the electron velocity. The term is formulated as:

$$\sigma_p \nabla \cdot (\mathbf{v}_e \times \mathbf{B}) = \sigma_p \left(\frac{1}{r} \frac{\partial (r w_e B_z)}{\partial r} - \frac{\partial (w_e B_r)}{\partial z} \right)$$

This equation is discretized as:

$$\sigma_{p,kp} \left(\frac{w_{e,kp} B_{z,kp}}{r_{kp}} + \frac{w_{e,kp+np} B_{z,kp+np} - w_{e,kp-np} B_{z,kp-np}}{2\Delta r} + \frac{w_{e,kp+1} B_{z,kp+1} - w_{e,kp-1} B_{z,kp-1}}{2\Delta z} \right)$$

The discretizations given above result in the following coefficients for the coefficient matrix:

$$\begin{aligned} a_N &= \sigma_{p,kp}/\Delta r^2 + \frac{1}{r_{kp}} \frac{\sigma_{p,kp}}{2\Delta r} \\ a_S &= \sigma_{p,kp}/\Delta r^2 - \frac{1}{r_{kp}} \frac{\sigma_{p,kp}}{2\Delta r} \\ a_E &= \sigma_{p,kp}/\Delta z^2 \\ a_S &= \sigma_{p,kp}/\Delta z^2 \end{aligned}$$

and the central coefficient is:

$$a_P = -2\sigma_{p,kp}/\Delta z^2 - 2\sigma_{p,kp}/\Delta r^2 \tag{3.165}$$

The remaining terms are handled as the source term that builds up the right hand side of the linear system. The source term is formulated as:

$$b_{source} = e\left(\frac{n_{e,ku}u_{i,ku} - n_{e,ku-1}u_{i,ku-1}}{\Delta z} + \frac{n_{e,kp}v_{i,kp}}{r_{kp}} + \frac{n_{e,kv}v_{i,kv} - n_{e,kv-nv}v_{i,kv-nv}}{\Delta r}\right) + \sigma_{p,kp}\left(\frac{w_{e,kp}B_{z,kp}}{r_{kp}} + \frac{w_{e,kp+np}B_{z,kp+np} - w_{e,kp-np}B_{z,kp-np}}{2\Delta r} + \frac{w_{e,kp+1}B_{z,kp+1} - w_{e,kp-1}B_{z,kp-1}}{2\Delta z}\right) + \frac{ek}{m_e\nu_{elastic}}\left(\frac{n_{e,kp+np} - T_{e,kp+np}}{2\Delta r} + \frac{n_{e,kp+1}T_{e,kp+1} - 2n_{e,kp}T_{e,kp} + n_{e,kp-1}T_{e,kp-1}}{\Delta z^2} + \frac{n_{e,kp+np}T_{e,kp+np} - 2n_{e,kp}T_{e,kp} + n_{e,kp-np}T_{e,kp-np}}{\Delta r^2}\right) \tag{3.166}$$

The linearization and discretization schemes for the governing equations are completed with these explanations. The solution methodology and the implementation details are explained in the following section.

4. ALGORITHM

The equations presented in Section 3.1 and 3.2 are solved with the methods described in Appendix B in a self-consistent manner. The three submodels, the electromagnetic model, the fluid model and the transformer model are executed in accordance. All the submodels are connected to each other by transferring parameters to provide the self-consistent solution. The relationship between the submodels is depicted in Figure 4.1.

Before starting to solve the model equations, AETHER needs some input parameters from the user. Some of these parameters must be given (or calculated) to perform the simulation. These input parameters for the dielectric wall configuration are listed below:

- RF coil frequency
- Physical length of the domain in both axial and radial directions
- Number of coil windings around the chamber
- Coil radius
- Effective length of the coils
- Number of mesh nodes in radial and axial directions
- Time step for fluid and EM models

For the biased wall configuration, instead of the RF settings listed above, the auxiliary electrode size and applied voltage should be given as input. In addition, the external power deposition should be entered. The power deposition field can either be uniform or distributed on the grid according to the particular problem setting.

The solution starts with the initial uniform electron temperature, plasma density and conductivity fields, and an initial RF coil current value. First, the electromagnetic model is solved and the resulting electric and magnetic fields are transferred to the fluid model. These electromagnetic fields are used in evaluating the Lorentz force

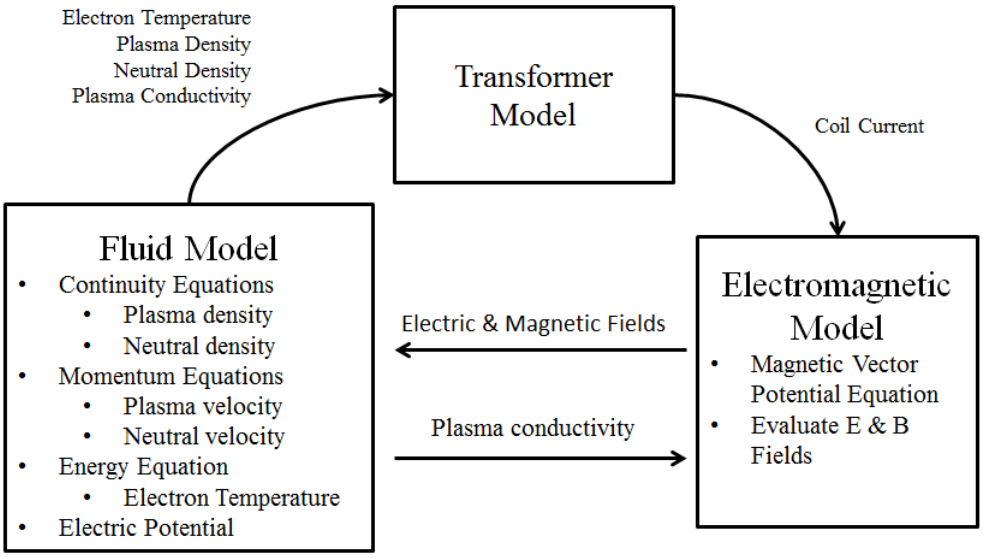

Figure 4.1. Numerical model and the flow of parameters between each submodel.

terms and the equations in the fluid model are solved in time. The resulting flow parameters are used to calculate the plasma conductivity and this value is transferred to the electromagnetic model, hence completing the coupling between the fluid and electromagnetic models.

In addition to this coupling, there is also an input to transformer model from the fluid model. Transformer model requires the flow parameters to evaluate the plasma resistance and inductance. Transformer model calculates the plasma impedance, and RF coil current is calculated and transferred to the electromagnetic model. The new current value is used in electromagnetic model to solve for the electromagnetic fields and the cycle is completed. The view of this scheme is presented in Figure 4.2.

Because of the difference in the time steps of electromagnetic and fluid models, fluid equations are solved at predetermined time step intervals. For the ICP simulations presented in this study, one fluid time iteration is performed between each 200 electromagnetic time iterations. Each fluid time step consists of inner iterations that last until all the equations have residuals that lie below the tolerance value assigned before starting the solution. In the beginning of each time step, linear solvers yield high residual values for equations. As the number of inner iterations increase, these

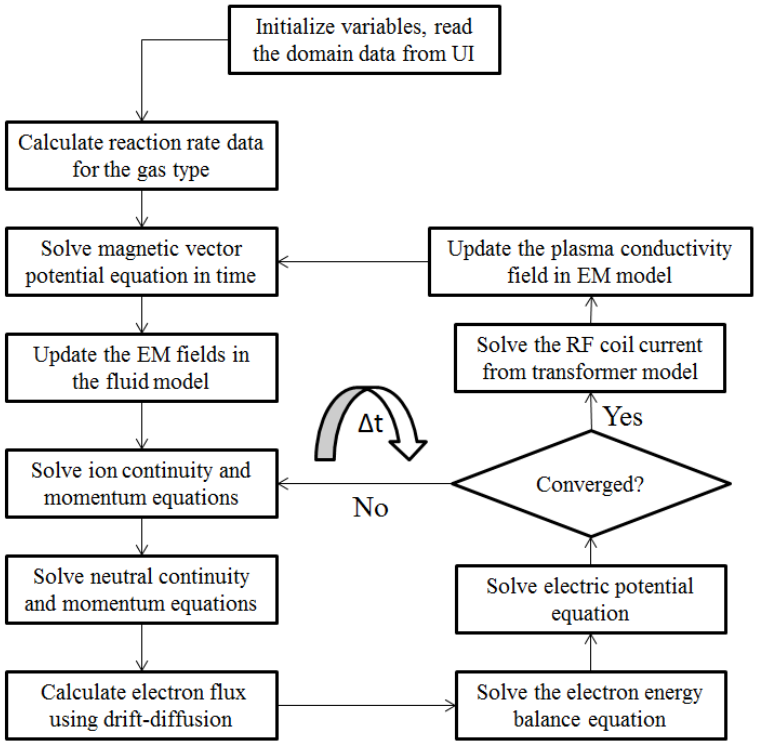

Figure 4.2. Fluid model algorithm and coupling with the electromagnetic model.

residual values decrease and eventually falls below the tolerance value, which is assigned as 1.0E-04 for this study. After the residuals fall below the tolerance, preferred solutions are written to files and then copied as previous time step's solutions for the next time step. Plasma conductivity is recalculated to be sent to the electromagnetic model. Afterwards simulation continues with the solution of electromagnetic model. Users can either input the number of RF cycles or time steps for the simulation before initiating the calculations, or can end the simulation as desired.

5. RESULTS

In the results section, the verification of the model is performed by comparing the results obtained from AETHER with the commercial software COMSOL Plasma Module [41], which is validated as a reliable computational tool for the solution of the fluid model for plasma [42]. The verfication study is presented in Section 5.1. Then the model is applied to the RF ion thruster configuration to evaluate thruster performance in Section 5.2.

5.1. Benchmark Problem: Argon ICP Enclosed within Dielectric Walls

The model explained in previous sections of this work is used to solve a benchmark ICP configuration to verify the results in the Plasma Module of the commercial software COMSOL. For the verification, the preferred discharge chamber is a cylinder made of a dielectric, which is 7 cm long and has a diameter of 8 cm. RF power is deposited into the plasma through the 10 coil windings around the chamber, which extends 5 cm in axial direction. Driving frequency is 13.56 MHz. Argon is the type of the gas. Initial pressure is 20 mTorr, which corresponds to 3.0E+20 m^{-3} neutral density. There is no neutral gas inlet to the system. All the ions that reach the wall go through a recombination process and directed back into the system as neutrals. The same configuration is solved also with COMSOL and the results are compared. For comparison, two different power deposition values, that result in steady-state solutions, are chosen. These values are 3500 W and 6000 W. The plasma density distribution obtained from AETHER at 10 miliseconds is shown in Figure 5.1. It is seen that the plasma is confined at the center of the discharge chamber because of the losses to the walls. It is also seen that the plasma density is slightly higher in the regions that are located below the coils (from origin to 0.050 m in axial direction) compared to regions that do not lay under RF coils (from 0.050 m to 0.070 m in axial direction).

The verification is performed by taking the data on two lines and comparing the electron number density values along these lines for different power deposition

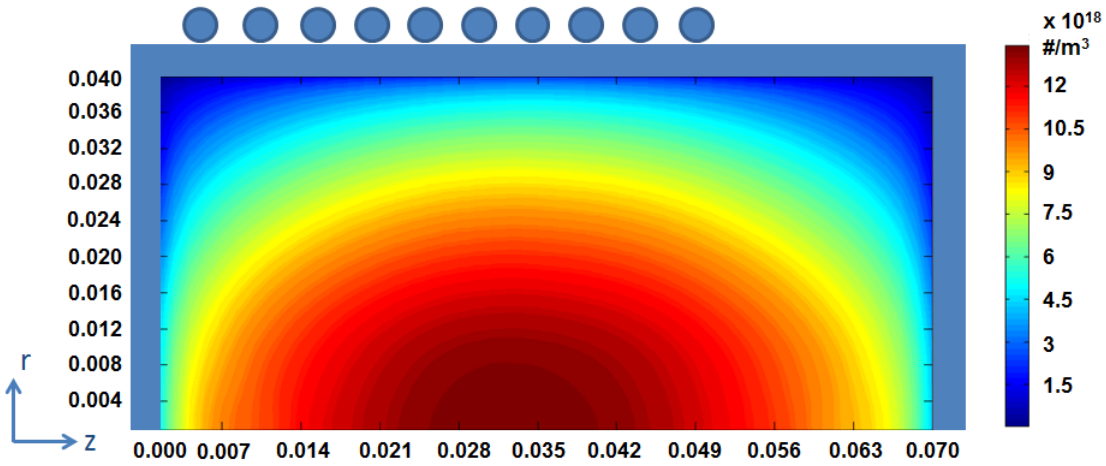

Figure 5.1. Plasma density at the end of 10 miliseconds. Due to the losses to the walls, plasma is confined in the center region of the domain.

values. The first line, $L_1 = |P_1P_2|$, is the center line in radial direction, which starts at $P_1 = (0.035, 0.000)$ and extends up to $P_2 = (0.035, 0.040)$. The number density values along the line L_2 are presented in Figure 5.2. The second line, $L_2 = |P_3P_4|$, is the center line in axial direction, which starts at $P_3 = (0.000, 0.020)$ and extends up to $P_4 = (0.070, 0.020)$. The number density values along the line L_2 are presented in Figure 5.3.

As it can be seen from both Figure 5.2 and Figure 5.3, solutions that come from AETHER matches with COMSOL's Plasma Module results to a great degree. The obtained results have also demonstrated grid independence. The comparison with COMSOL completes the verification of the fluid and electromagnetic models. These models are also verified separately by solving the lid-driven cavity problem and the electromagnetic fields for a plasma torch configuration.

For the verification of the transformer model, a simple test case within AETHER is considered to be sufficient. Transformer model takes the power to be deposited into the plasma as one of the inputs. According to the power value, it arranges the current to be supplied to the RF coils. The transformer model can be verified if the power given as input to the model is equal to the power calculated using Equation 3.69, which is evaluated with the plasma parameters that are independent of the transformer model.

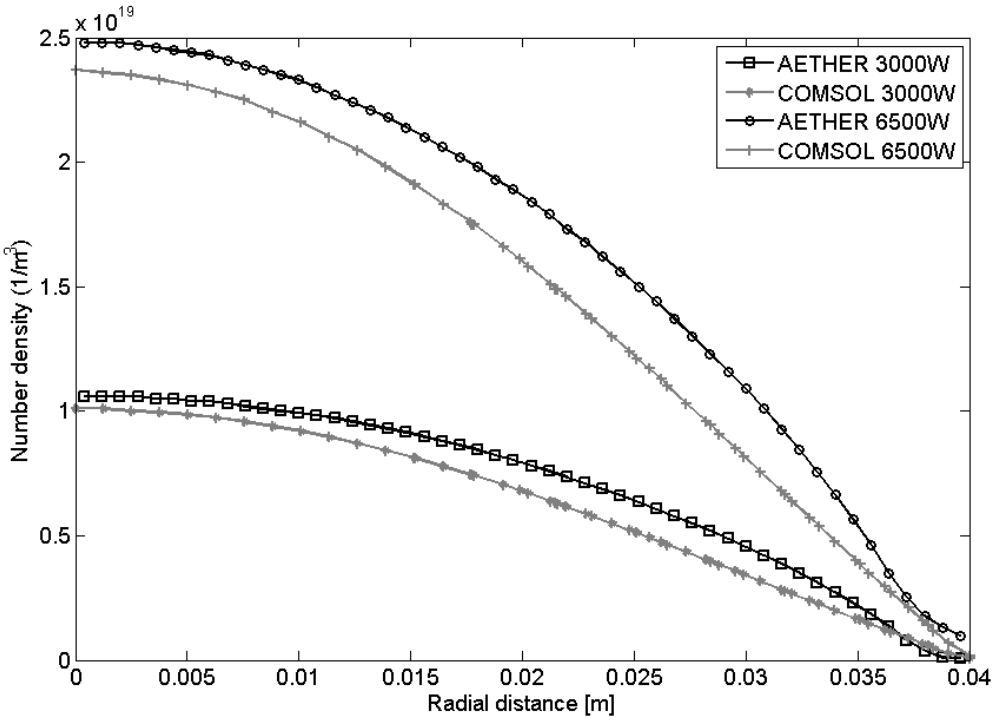

Figure 5.2. Results from AETHER and COMSOL along the line L_1 for 3000 W and 6500 W.

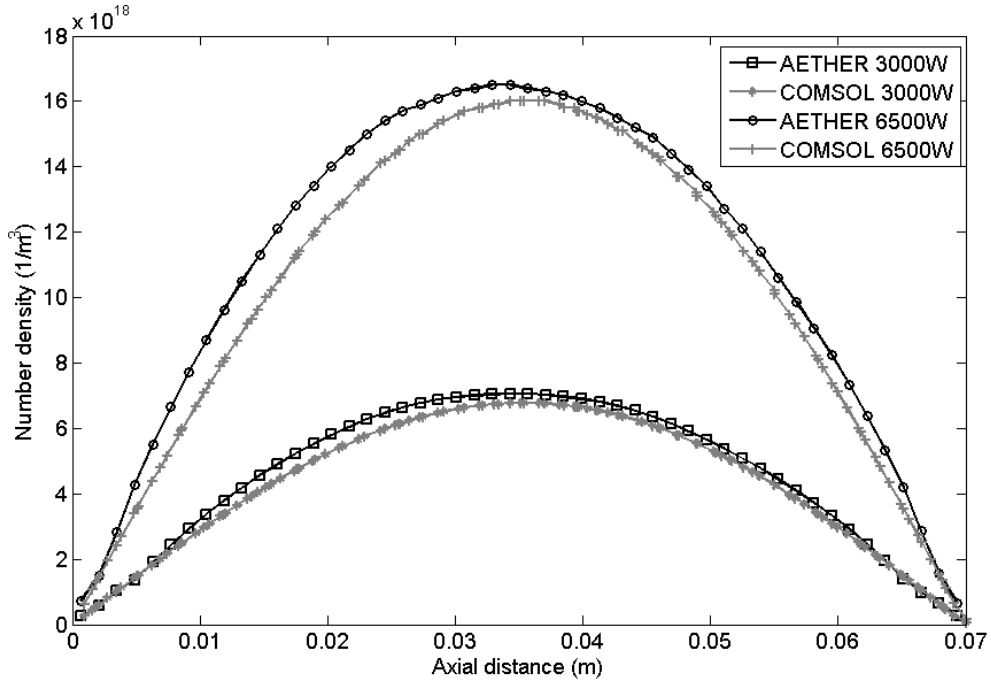

Figure 5.3. Results from AETHER and COMSOL along the line L_2 for 3000 W and 6500 W.

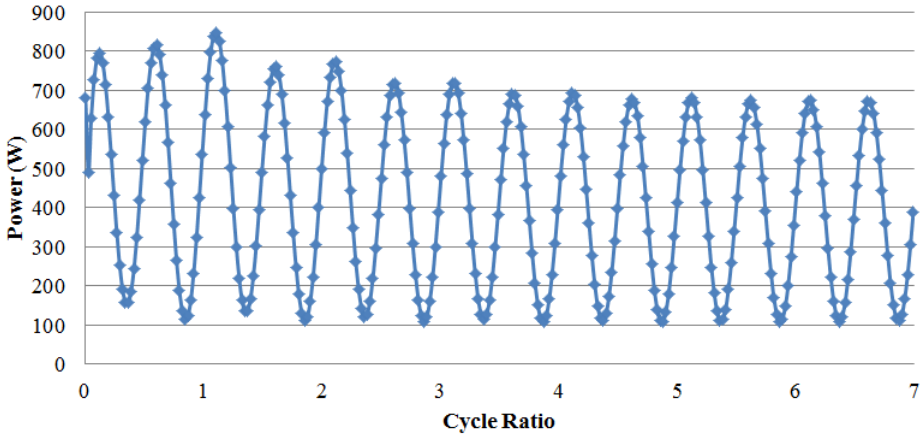

Figure 5.4. Power deposition with time. Verification of the transformer model for $P_{dep} = 400$ W.

For the verification, 400 W of power deposited into the plasma. The change of the total power deposition with time is presented in Figure 5.4. It is observed that after 4 RF cycles, the amount of power deposited into the plasma becomes equal to the input given to the transformer model.

The electric potential distribution is evaluated as presented in Figure 5.5. Here at the boundaries of the plasma, which is the sheath edge, the electric potential is taken as zero and potential values are evaluated with respect to the sheath edge potential. It is also possible to assume that the walls have the 0 V boundary condition. If this is assumed, the plasma potential can be calculated by adding the sheath potential drop to the evaluated potential. The sheath potential is evaluated by equating the ion and electron fluxes to the wall, which is the zero current condition 3.2 that is valid for dielectric walls. According to the sheath potential drop formula 3.87, the potential drop for the mean temperature, 3.93 eV, is 20.71 V.

5.2. RF Ion Thruster Performance Results

The discharge chamber of an RF ion thruster is very similar to the benchmark problem solved in the previous section. In this section an example thruster configuration, which is very similar to RIT-15LP [43], is modeled. The following design will be referred as the concept design in the remaining of this study. This thruster has 15

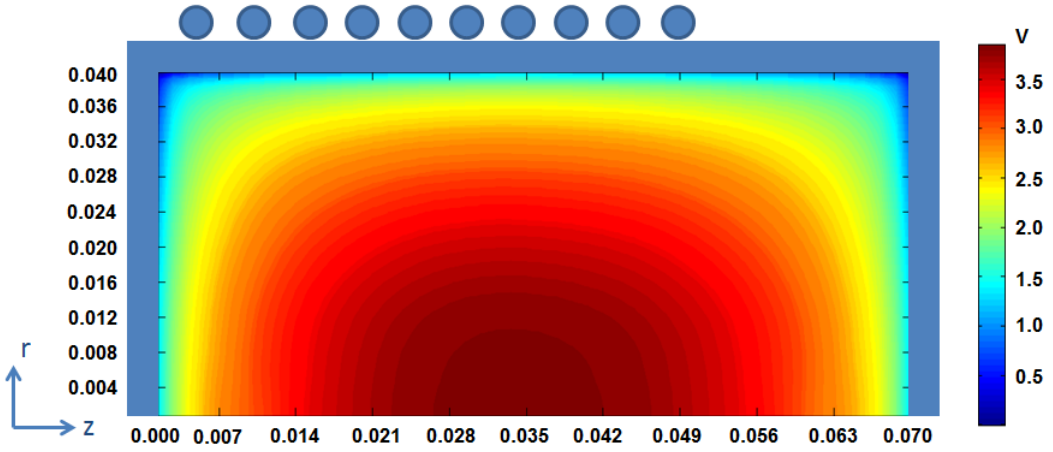

Figure 5.5. Electric potential distribution for the benchmark problem.

cm diameter and 7 cm axial length. The coil wrapped around the cylindrical discharge chamber is represented on the axisymmetric domain with 13 equidistant coils. The RF frequency is 2 MHz, which means that one RF cycle is $5.0e-07$ sec. Typical neutral gas flow rates for 15-cm thrusters are found to be on the order of 10-13 sccm [9]. There are RF thruster designs that work with a few sccm's as well [8]. In this study gas flow rates are tested from 4 sccm to 13 sccm to investigate various pressure levels.

The code requires a very little amount of change to simulate an RF ion thruster. The major change is performed for the boundary conditions of the electromagnetic equation. The magnetic field boundary condition incident on the grid is derived by assuming that the perpendicular component of the magnetic field to the grid becomes zero because grids have much higher electrical conductivity compared to the discharge plasma:

$$\frac{1}{r}\left[\frac{\partial(rA_\theta)}{\partial r}\right] = 0 \tag{5.1}$$

In addition to this condition, the azimuthal electric field on the grid boundary is zero. To capture both of these effects, the approach used in [24] is utilized here, and the magnetic vector potential is taken to be zero on the grid boundary. The dielectric wall conditions are those applied in the benchmark problem.

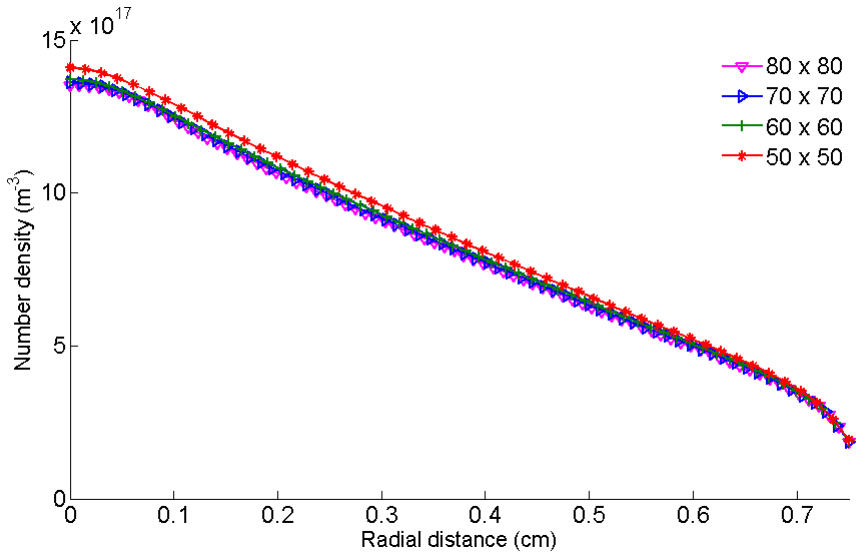

Figure 5.6. Radial center line plasma density variation for a 400 W thruster evaluated on different grids.

Another change is performed at the boundary conditions for plasma fluid equations because of the existence of the grids at the end of the chamber. Grids have transparency values defined for ions and neutrals, which indicate the ratio of the incident particles going through the grids. The remaining portion is assumed to be hitting the grid wall. The grid boundary condition for neutrals is given in Equation 3.84.

In addition to the results evaluated for the benchmark problem, which are plasma density, electron temperature, and electric potential distribution, there are additional results that deserve attention. Beam current obtained from the ion thruster is directly related to the thrust obtained from the device. The beam current is calculated as:

$$I_{beam} = e n_i u_i A_g \Phi_i \tag{5.2}$$

where A_g is the whole grid area and Φ_i is the ion transparency of the grid. The ratio of the power deposited into the plasma and the beam current give a measure for the energy efficiency of the thruster. This ratio is called as the discharge loss per ion, and

formulated as:

$$\eta_d = \frac{P_{abs}}{I_{beam}} \tag{5.3}$$

where P_{abs} is the absorbed power by the plasma. The thruster designing effort is directed at minimizing this parameter for the desired thrust value. All the other parameters, including geometry, neutral gas pressure and accelerator grids are adjusted to obtain a particular value of thrust with minimum discharge loss. Therefore this parameter is used to evaluate the performance of designs accordingly in this study. The physical meaning of the discharge loss per ion is important to understand the concerns for a thruster design. This parameter corresponds to the energy spent for the production of a single ion. For the Xenon atom, the first ionization potential is 12.1 eV as stated before in this text. But including the energy deposited into electrons that do not necessarily lead to ionization and the wasted ions that collide with the wall and become neutrals, the energy spent on an ion that can be extracted from the thruster can reach the orders of 400-500 eVs. It is important to notice that all of this energy is actually a loss for the whole system since it is spent only to the conditioning of the propellant gas, and it should be minimized.

As shown in Section 5.1, the power to be deposited in the plasma can be successfully imposed by the transformer model. Five different power deposition cases are tested with 250-, 300-, 350-, 400-, and 450-W power deposition values for 4 sccm neutral Xenon gas inflow.

Before presenting the results of these cases, it should be stated that the model developed here satisfies the numerical accuracy criteria presented in [44]. The finite volume discretization for the interior nodes is of second order. Also, the results of the grid refinement are presented in Figure 5.6 to verify that the model built in this study is grid independent.

The plasma density distribution for 400-W power deposition along with the representation of the structured grids in the axisymmetric domain for the concept design

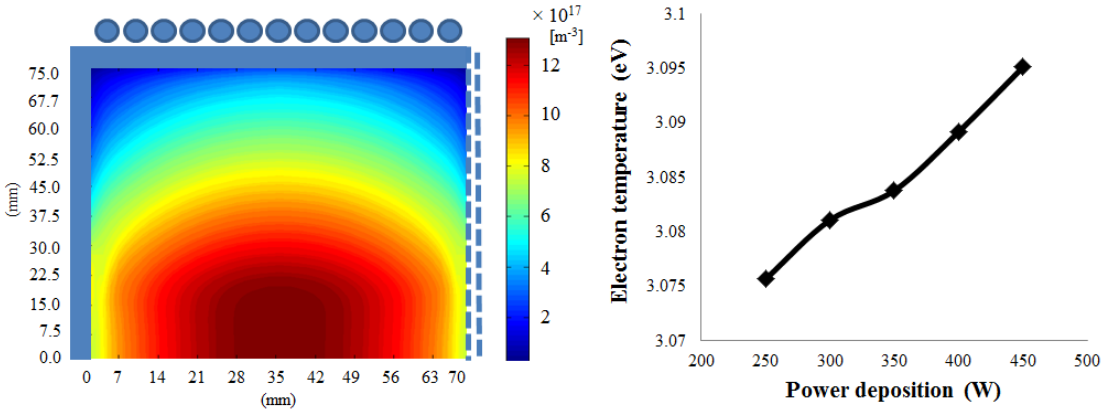

Figure 5.7. Left: Plasma number density distribution. Right: Electron temperature vs. power deposition.

are shown in Figure 5.7. The plasma density is observed to be maximum in the center region of the thruster discharge chamber. The density decreases toward the walls and the grid, where the ions are either neutralized at the wall or accelerated out from the discharge chamber. This picture shows the same tendency as presented in [8] and [24].

The mean electron temperature value shows a similar trend with the examples from the literature. In [8], the global temperature for 7-cm RF ion thruster is found to be 3.2 eV. The mean temperature value evaluated in this study is very close to these values. As it can be observed in Figure 5.7, the electron temperature reaches steady state around values that are very close to each other for the range of power deposition values tested. For all the cases, the steady-state temperature is approximately 3.08 eV. This is a typical behavior for low-temperature plasmas, where additional power results in higher ionization but not in appreciable temperature increase [1], [45].

The spatial distribution of power deposition in one cycle for the 350-W case after the model reaches the steady state is shown in Figure5.8. This trend matches with the one presented in [8]. It is observed that the power deposition is maximum in the top region and varies with the current in time. The maximum penetration of the power into the plasma occurs at 3/8 and 7/8 cycle ratios. There is a 1/8 cycle ratio phase shift between the current maximum and the maximum value of the power penetration. It is also observed from the numerical experiments that the penatration into the plasma

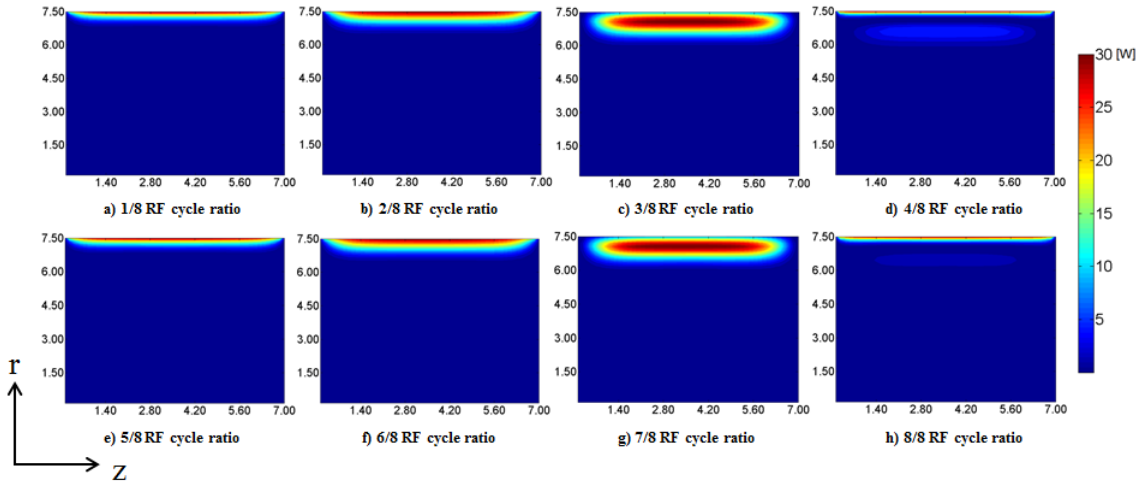

Figure 5.8. Power deposition into the RF ion thruster over one RF cycle.

decreases with the increasing RF frequency, a trend that is verified with the skin depth Equation 3.91.

The plasma density for different power deposition values is shown in Figure 5.9. Steady-state plasma density is increasing with the power deposition. This trend is also observed in [23]. It is observed a small drop at plasma density values in the beginning of the simulation. The configurations tested with different power deposition values start with the same initial condition and evolve in time. The reason for this drop is observed to be the initial conditions. As long as the initial conditions stay within reasonable values, it is observed that the simulations reach the same steady-state solution. Plasma density values are observed to increase with increasing power deposition as opposed to the case observed with the electron temperature. The beam currents are shown in Figure 5.10. The current extracted from the thruster is found to be increasing with the increasing power deposition. This is consistent with the plasma density data, since the beam current is a function of the ion density incident on the grid, as shown in 5.2. The beam current is directly proportional to the thrust desired to be generated. Neglecting the double ionization, assuming that the ions all fall through the same grid potential, the linear relationship between the beam current and the thrust is given as

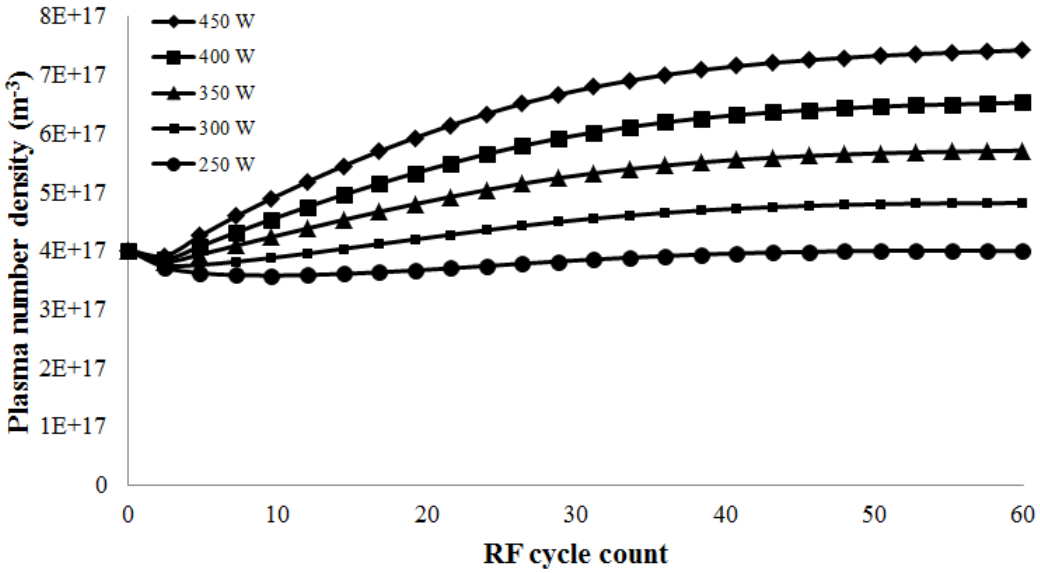

Figure 5.9. Plasma density variation vs. RF cycle count for different power deposition levels.

follows [22]:

$$T = I_b \sqrt{\frac{2 m_i V_b}{e}} \tag{5.4}$$

where V_b is the beam voltage. This relation requires the thruster designs to yield specified beam currents to reach the thrust level aimed for the particular application.

Another way to express the thrust is to express it as the product of the mass flow rate and the exhaust velocity: $T = \dot{m}_i v_i$. The mass flow rate can be calculated by dividing the current to the elementary charge, e, assuming that all of the ions are singly ionized and then multiplying it with the mass of an ion. The exhaust velocity can be calculated with the energy balance if the initial ion velocity incident on the grid and the potential drop between the accelerator grids are known. It should be remembered that the exhaust velocity value that is calculated using this method is a global value for the whole domain, and the calculation relies on the assumption that the ions fall through the entire electrostatic potential drop between the accelerator grids.

The plot of the discharge loss per ion against the power deposition can be seen in

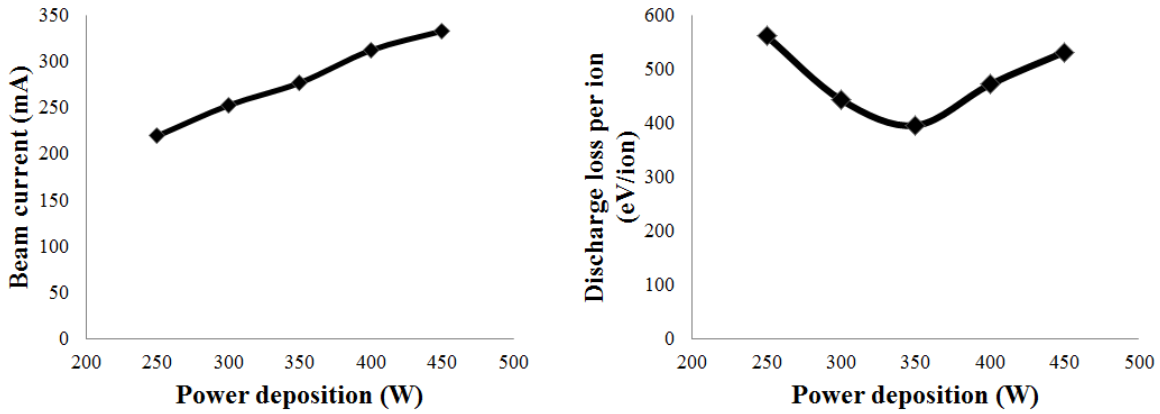

Figure 5.10. Left: Beam current vs. deposited power. Right: Discharge loss per ion vs. deposited power.

Figure 5.10. The discharge loss per ion is evaluated for various thruster configurations in the literature. In [22], it is stated that an example 20-cm thruster can have low discharge loss values as 253 eV/ion. It means that the discharge loss per ion values obtained in this study are considerably high for a feasible thruster design. It can be lowered by changing the neutral inlet flux, but for this study, the concern is not the reduction of the discharge loss per ion, but rather to observe how it changes with the varying power deposition. The behavior of the curve shows that the increase in power deposition does not necessarily result in a proportional decrease or increase in the discharge loss.

When the Xenon gas mass flow rate and the background neutral pressure are increased, a higher power deposition is required to sustain the plasma as expected. With the same discharge chamber geometry, the steady-state temperature is this time much higher along with the power deposition. To observe the effect of high pressure, the neutral flux is increased from 4 sccm to 13 sccm. The tested power deposition values that yield steady-state solutions are 500-, 600-, and 700-W. As it is observed with the previous configuration, the electron temperature yields average values which are very close for each case. The average temperature change for each case versus time is presented in Figure 5.11. For the 600 W case, the mean electron temperature is 4.31 eV.

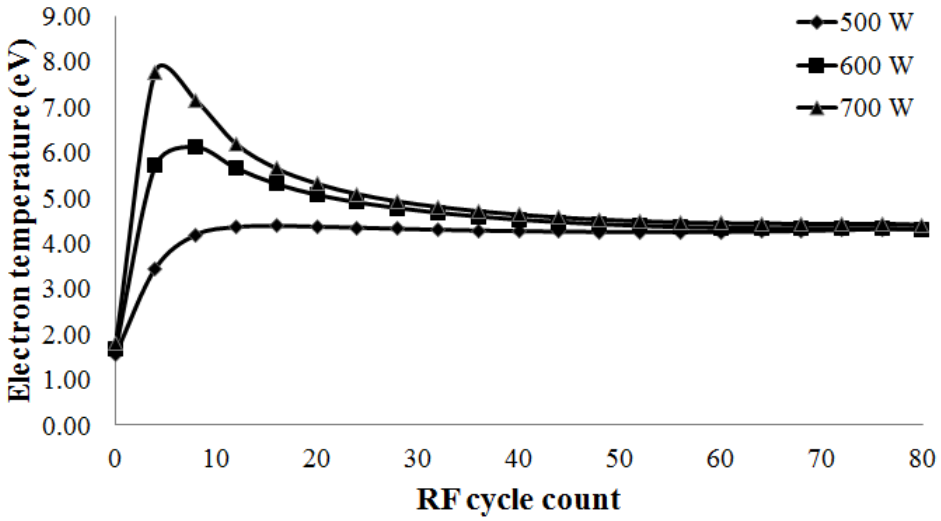

Figure 5.11. Mean electron temperature change vs. time for the high pressure case.

The discharge loss per ion value for this high pressure level is higher than the previous configuration. For the three power deposition levels tested here, the discharge loss per ion does not fall below 650 eV/ion. On the other hand, the lower power deposition values do not result in a steady-state solution, and the plasma turns out to be not sustainable with lower power deposition values.

This lays out another constraint for the thruster design. From the low-pressure configuration, considering Figure 5.10, it could be derived that power deposition does not necessarily increase or decrease the discharge loss per ion. And from the high discharge loss per ion values obtained from the high pressure case, it can be derived that the increasing the mass flow rate and the resulting high electron temperature do not necessarily result in a lower discharge loss per ion.

6. CONCLUSIONS

An extensive 2D axisymmetric fluid plasma model, which is coupled with the developed electromagnetic and transformer models, are successfully developed and implemented. The implementation of the model is done using the C++ programming language.

In this study, the finite volume discretization of the fluid equations that describe the behavior of a partially ionized ICP and include the coupling between the fluid and the electromagnetic models is explained. Additionally a transformer model is included to capture the matching circuit effect to simulate the laboratory experiments. These functionalities are wrapped under a software framework, which can be used by the end-user without delving into the details of the code.

To our knowledge, this is the only software and model developed that can capture the coupling between the fluid and electromagnetic equations and relate plasma parameters to laboratory experiments without requiring an empirical input. Details regarding the finite volume discretization of the equations, velocity and pressure correction terms for the modified Euler equations in the scope of the finite volume method are given extensively. Also the finite volume scheme adapted for the plasma fluid equations will be presented for the first time with this work. Implicit handling of the time-dependency, convergence criteria, matrix storage scheme, multi-core parallelization, linear solvers, and implementation of the code are explained.

The verification of the model is performed by comparing the results of the AETHER platform with the results of the commercial software, COMSOL's Plasma Module. It is observed that the results from AETHER match those that are obtained from COMSOL's Plasma Module with a little amount of overshoot.

The performance parameter of an RF ion thruster, the discharge loss per ion, is the ratio of the power input to beam current. The grid at the end of the discharge

chamber creates the driving electrostatic force for the beam current. Therefore, accelerator grids play an important role in overall ion thruster performance. The design of these accelerator grids is the subject of the ion optics physics. These factors should be considered for a complete thruster performance evaluation. In this thesis, the performance of the thruster is evaluated only by considering the factors that depend on the discharge itself.

The example discharge chamber design used in this study with different power deposition values shows that interdependent plasma parameters result in a nonlinear relationship between the discharge loss per ion and the power deposition. For a given design, a higher power deposition can result in a lower discharge loss per ion value and vice versa.

The behavior of the discharge loss shown in Figure 5.10 indicates the existence of an optimization problem. For a given geometry and a given coil configuration, it is possible to find an optimum configuration that yields the lowest discharge loss per ion value. The configuration should also yield the desired beam current and therefore the desired thrust. The solution of this optimization problem is left as future work. It is observed that after a certain value of power deposition, increasing beam current also results in increasing discharge loss per ion. It means for a particular thruster configuration, there is a trade-off between the beam current and the discharge loss, which should be considered during the thruster design process.

The model developed here shares a common bottleneck with most of the other plasma codes. It requires rather accurate initial conditions. It is very challenging to find initial conditions for the plasma if a previous empirical or numerical data is not available. In this study a great effort is spent to find the configurations that would reach steady-state in a reasonable amount of computational time. Additionally, as future work, a plasma instability study can be performed. An introduction to this type of analyses is to be found in [46].

An extension of the code can be possible if the capability to capture the electrostatic fields in plasma is implemented. This can also lead to the simulation of various types of plasma sources where the nonambipolar flow is dominant. The simulation of these type of flows could be possible if electrons are solved separately from the ions and the electric potential can be evaluated by solving the Gauss' Law. An attempt to these type of simulations can be found in [47]. The interested reader should also consider looking into the different sheath phenomena observed in these types of plasma [48].

The model and the implementation can currently handle structured grids with axially symmetric domains. As future work, the extension of the code into three dimensions can be performed to gain the capability of simulating wider scope of geometries. The code is also parallelized for shared memory structures, such as a multi-core system with single processor. The distributed memory parallelization can be performed with MPI (message passing interface) as future work.

APPENDIX A: NUMERICAL CALCULATION OF THE ELLIPTIC INTEGRALS OF FIRST AND SECOND KIND

The elliptic integrals are used to evaluate the magnetic vector potential. The elliptic integral of the first kind is:

$$K(m) = \int_0^{\pi/2} \frac{d\phi}{\sqrt{1 - m^2 \sin^2 \phi}} \tag{A.1}$$

The elliptic integral of the second kind is:

$$E(m) = \int_0^{\pi/2} \sqrt{1 - m^2 \sin^2 \phi}\ d\phi \tag{A.2}$$

These integrations are performed numerically using the composite trapezoidal rule. The composite trapezoidal rule is defined as in [49]:

$$\int_a^b f(x)\ dx = \frac{h}{2}[f(a) + 2f(x_1) + \ldots + 2f(x_{n-1}) + f(b)] \tag{A.3}$$

where $h = (b - a)/n$ for n subintervals. For the implementation, n is chosen to be 50. The elliptic integral functions are embedded into *ppsSolverHelpers.cpp*

APPENDIX B: LINEAR SOLVERS

For 2D axially symmetric domain, the second order finite volume and finite difference discretizations result in a banded matrix structure for each equation. This banded structure consists of five diagonal entries and zeros everywhere else, as depicted in FigureB.1. The preferred sparse matrix storage scheme is compressed diagonal storage (CDS) and it is implemented as described in [3]. To solve these linearized systems, the utilization of an iterative solution scheme is mandatory. Jacobi, Gauss-Seidel [49], GMRES [4] and ILU preconditioned GMRES [50] methods are implemented in the software framework as solvers. These solvers are implemented considering the matrix storage scheme used. All equations are solved successively and residual is reduced below a predetermined threshold for all equations.

Among these solvers, Jacobi and Gauss-Seidel methods are considered stationary, and GMRES is considered among non-stationary methods [3]. The details of these solvers are presented in the following sections.

Jacobi Method

The Jacobi method is the most trivial iterative solution technique presented in this study to solve the linear systems arising from the discretization of the governing equations. To solve the linear system, $Ax = b$, the following algorithm is utilized:

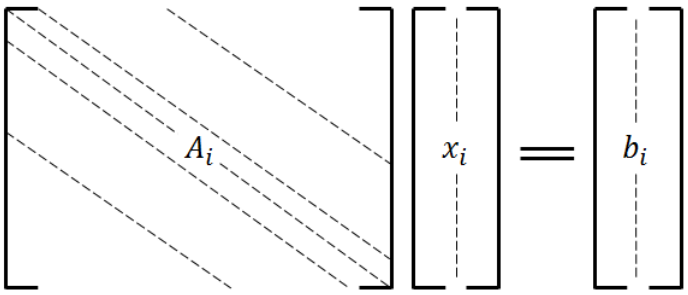

Figure B.1. Pentadiagonal matrix structure resulting from the discretization of equations.

Choose an initial guess $x^{(0)}$ to the solution x.
for $k = 1, 2, \ldots$
  for $i = 1, 2, \ldots, n$
    $\bar{x}_i = 0$
    for $j = 1, 2, \ldots, i-1,\ i+1, \ldots, n$
      $\bar{x}_i = \bar{x}_i + a_{i,j}x_j^{(k-1)}$
    end
    $\bar{x}_i = (b_i - \bar{x}_i)/a_{i,i}$
  end
  $x^{(k)} = \bar{x}$
  check convergence; continue if necessary
end

Figure B.2. Algorithm for the Jacobi Method [3].

Each row of the resulting coefficient matrix actually represents the coefficients of the variables for an equation. For the ith equation, and hence for the ith row:

$$\sum_{j=1}^{n} a_{i,j}x_j = b_i \tag{B.1}$$

In the scope of the Jacobi method, the ith equation is solved for the ith variable while keeping the other variables constant. This leads to:

$$x_i = \left(b_i - \sum_{j \neq i} a_{i,j}x_j\right) \Big/ a_{i,i} \tag{B.2}$$

The formula given above can be formed into an iterative scheme. Denoting the iteration count with k, the iterative scheme is expressed as:

$$x_i^k = \left(b_i - \sum_{j \neq i} a_{i,j}x_j^{k-1}\right) \Big/ a_{i,i} \tag{B.3}$$

The pseudocode for the Jacobi method is given in Figure B.2. The advantage of this solver is that it can be executed in parallel. As it can be seen from the iterative formulation B.3, each row can be executed at the same time. This is how this solver is

Choose an initial guess $x^{(0)}$ to the solution x.
for $k = 1, 2, \ldots$
  for $i = 1, 2, \ldots, n$
    $\sigma = 0$
    for $j = 1, 2, \ldots, i-1$
      $\sigma = \sigma + a_{i,j} x_j^{(k)}$
    end
    for $j = i + 1, \ldots,$ n
      $\sigma = \sigma + a_{i,j} x_j^{(k-1)}$
    end
    $x_i^{(k)} = (b_i - \sigma)/a_{i,i}$
  end
  check convergence; continue if necessary
end

Figure B.3. Algorithm for the Gauss-Seidel Method [3].

implemented in the scope of AETHER.

Gauss-Seidel Method

The Gauss-Seidel method is a modified version of the Jacobi method. In the Jacobi method, as explained in the previous section, each component of the variable vector, x_i, is calculated by holding the other variables fixed at the values obtained from the previous iteration. In the Gauss-Seidel method, the equations are examined one at a time in sequence, and the results from the current iteration are used as soon as they are available. This results in the following formula to calculate the variables:

$$x_i^{(k)} = \left(b_i - \sum_{j<i} a_{i,j} x_j^{(k)} - \sum_{j>i} a_{i,j} x_j^{(k-1)} \right) \Big/ a_{i,i} \tag{B.4}$$

The pseudocode of this algorithm is presented in Figure B.3. Here it should be noted that the computation given above must be performed in series. Each calculation in one iteration depends on the other calculations in the same iteration, therefore parallelization of this algorithm is not possible. But compared to the Jacobi method performed

Choose an initial guess $x^{(0)}$ to the solution x.
Compute $r^{(0)} = b - Ax^{(0)}$, $\beta = \|r^0\|$ and $v^{(1)} = r^{(0)}/\beta$
for $j = 1, 2, \ldots, m$
  $w^{(j)} = Av^{(j)}$
  for $i = 1, 2, \ldots, j$
    $h_{i,j} = \left(w^{(j)}, v^{(i)}\right)$
    $w^{(j+1)} = w^{(j)} - \sum_{i=1}^{j} h_{i,j} v^{(i)}$
  end
  $h_{j+1,j} = \left\|w^{(j+1)}\right\|$
  $v^{(j+1)} = w^{(j+1)}/h_{j+1,j}$
end
$x^{(m)} = x^{(0)} + V^{(m)} y^{(m)}$ where $y^{(m)}$ minimizes $\left\|\beta e_1 - \bar{H}^{(m)} y\right\|$
Restart:
Compute $r^{(m)} = b - Ax^{(m)}$; if satisfied, then stop
else compute $x^{(0)} := x^{(m)}$, $v^{(1)} = r^{(m)}/\left\|r^{(m)}\right\|$

Figure B.4. Algorithm for the Generalized Minimal Residual (GMRES) Method [4].

in series, the Gauss-Seidel method results in faster convergence.

GMRES: Generalized Minimal Residual Method

The Generalized Minimal Residual (GMRES) method is a Krylov subspace method developed to solve nonsymmetric and not positive real linear systems. GMRES utilizes the mathematical properties of the Krylov subspace $K_k \equiv span\{v_1, Av_1, ..., A^{k-1}v_1\}$ and its l_2-orthonormal basis $\{v_1, v_2, ..., v_k\}$.

The full description of the method is presented in [4] and will not be explained here with all the details. But it is necessary to describe the flow of the algorithm and the mathematical principles that this method relies on. The pseudocode of the algorithm is presented in Figure B.4. The algorithm starts with an initial guess, as most iterative schemes do. The residual ($r_0 = b - Ax_0$) that is computed from this initial guess is used to form the first basis vector (v_1) of the l_2-orthonormal basis of the Krylov subspace. V_m is initialized as the matrix whose columns are the l_2-orthonormal

Choose an initial guess $x^{(0)}$ to the solution x.
Solve $Mr^{(0)} = b - Ax^{(0)}$, $\beta = \|r^0\|$ and $v^{(1)} = r^{(0)}/\beta$
for $j = 1, 2, \ldots, m$
    Solve $Mw^{(j)} = Av^{(j)}$
    for $i = 1, 2, \ldots, j$
        $h_{i,j} = \left(w^{(j)}, v^{(i)}\right)$
        $w^{(j+1)} = w^{(j)} - \sum_{i=1}^{j} h_{i,j} v^{(i)}$
    end
    $h_{j+1,j} = \left\|w^{(j+1)}\right\|$
    $v^{(j+1)} = w^{(j+1)}/h_{j+1,j}$
end
$x^{(m)} = x^{(0)} + V^{(m)} y^{(m)}$ where $y^{(m)}$ minimizes $\left\|\beta e_1 - \bar{H}^{(m)} y\right\|$
Restart:
Compute $r^{(m)} = b - Ax^{(m)}$; if satisfied, then stop
else compute $x^{(0)} := x^{(m)}$, $v^{(1)} = r^{(m)}/\left\|r^{(m)}\right\|$

Figure B.5. Algorithm for the ILU preconditioned Generalized Minimal Residual (GMRES) Method [3].

basis $\{v_1, v_2, ..., v_m\}$. The main loop in the GMRES algorithm calculates the remaining vectors of this basis and generates a matrix $H_m \equiv V_m^T A V_m$, which is an upper $m \times m$ Hessenberg matrix whose entries are the scalars $h_{i,j}$. Here the parameter m is called as the Krylov subspace dimension. m is generally held is a small number, since when m increases the number of vectors requiring storage increases linearly and the number of multiplications with $\frac{1}{2}m^2N$, where N is the size of the basis vectors [3]. Therefore the algorithm is restarted at every m steps to accelerate the solution. In the last step of the algorithm, it is seen that the vector y is calculated in the scope of a least squares problem. This problem is solved by the QR factorization of the H_m matrix generated through plane rotations. The QR factorization is rather simple to implement thanks to the fact that H_m is an upper Hessenberg matrix. The implementation of this scheme is performed as given in [3] and [51].

ILU-preconditioning of GMRES

The convergence rate of a linear method depends on some properties of the coefficient matrix. These properties, which are directly related to the convergence of the used method, are called as spectral properties. The idea of preconditioning focuses on transforming the coefficient matrix to obtain more favorable spectral properties [3]. The preconditoner is often represented with a matrix, M, that either approximates the coefficient matrix, A, or its inverse, A^{-1}, in some way and it transforms the linear system as:

$$M^{-1}Ax = M^{-1}b \qquad or \qquad MAx = Mb \tag{B.5}$$

ILU-preconditioning is one of these methods where the coefficient matrix, A, undergoes an LU-factorization. LU-factorization is the decomposition of the coefficient matrix, A, as the product of a lower and an upper triangular matrix ($A = LU$). While applying an LU-factorization to a coefficient matrix, it is desirable to obtain a similar matrix to the coefficient matrix in terms of the storage requirements. The incomplete LU factorization is performed to preserve the original sparsity pattern of the coefficient matrix, since it fills only the stored nonzero entities in the original matrix. The pseudocode of the algorithm is presented in Figure B.5.

The ILU-preconditioning is implemented into the code and the choice left to the user whether to utilize it with GMRES. A computational cost analysis should be made before applying this preconditioner to solve an equation, because generating the ILU factorization and applying the required forward and backward substitutions also result in extra computational cost. In our implementation it is observed through numerical experiments that the application of ILU-preconditioning decreases the required computational time to solve our equations.

APPENDIX C: IMPLEMENTATION OF THE SOFTWARE: AETHER

A software is built in the scope of this work, which is named as AETHER. The software is built according to the model-view-controller design methodology [52] in C++ programming language. The user interface is developed using the WxWidgets [53] cross-platform user interface C++ library. The software has an OpenGL renderer for results visualization. The Visualization Toolkit (VTK) [54] is utilized for visualization purposes. The solvers and the mathematical calculations are implemented mostly parallel, providing 100% CPU usage during the solution process. For the multi-core parallelization Microsoft's Parallel Patterns Library [55] is utilized.

The model-view-controller design of the algorithm and the classes under each category is presented in Figure C.1. The classes that build up the software bear the abbreviation *pps*, which stands for plasma physics simulations, in front of their names. The hierarchy between the classes in this design methodology is very important. The user executes commands through the controller class, *ppsControl*. The controller class inherits the graphical user interface (GUI), where the user gives commands to the software. The viewer classes include the objects on the user interface through the *ppsMainFrame* class, including all the buttons, menus and selection boxes, etc. The VTK is incorporated into the software and the user interface through the *ppsVTKView* class. When the user executes the solve commands, a subroutine in the controller class passes the information on the GUI to the classes in the Model group and solves the problem. To facilitate the communication, there is an umbrella class, named as *ppsModel*, which is used to receive the commands from the controller class and transfer them to the corresponding physical models.

Except for the VTK and WxWidgets toolkits for user interace development, there are no other external package incorporated into the code. All of the computations are performed using the in-house developed C++ routines. Since there is no external

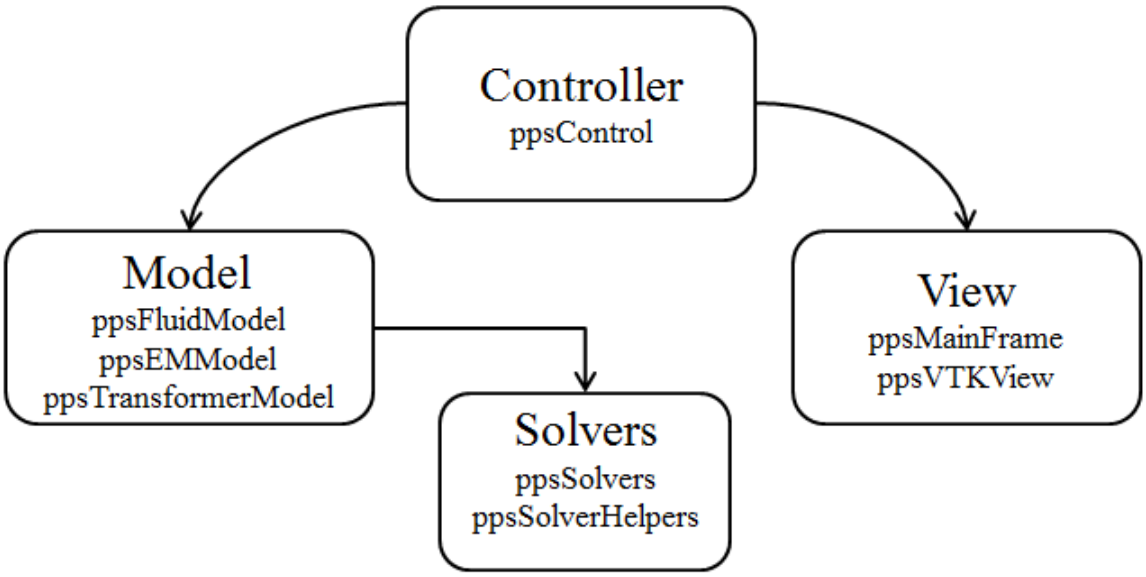

Figure C.1. Model-view-controller design of the software AETHER, and the hierarchy between classes.

package used for mathematical operations either, operations like vector dot product, matrix-vector multiplication, matrix-matrix multiplication, etc. are implemented using functions under a class.

The coding effort has started from the lowest level with these algebraic operations and useful routines. These operations include averaging of a vector, writing a vector to a file whose name to be specified, efficient multiplication of a pentadiagonal matrix with a vector, writing a coefficient matrix to a file whose name to be specified, filling a vector with zeros, initializing a dynamic vector whose size and dimensions are to be given as inputs, and copying a vector's entries to another. These functions build up the class structure named as *ppsSolverHelpers*.

The solver class is built as the next step. The solvers described in Section **??** are implemented into the *ppsSolvers* class. As long as the compressed diagonal matrix storage scheme is utilized, these solvers along with the *ppsSolverHelpers* can be used independent of the software with other projects. The solver classes are created in *ppsFluidModel* and *ppsEMModel*, and can be accessed from these classes.

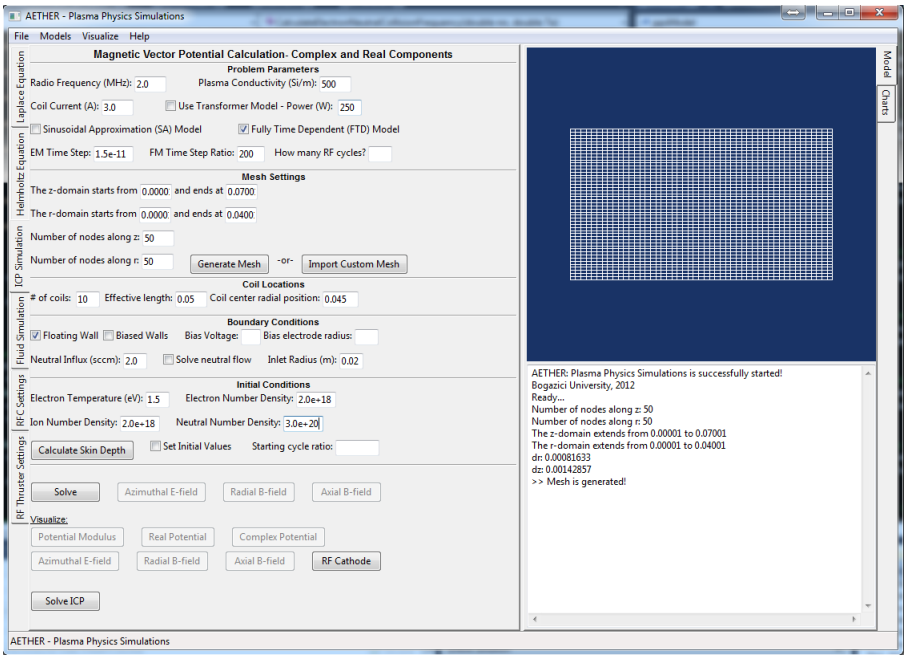

Figure C.2. The graphical user interface (GUI) of the AETHER software. Left hand side of the software is separated for the settings modifiable by the user. Right hand side is split into two, where the upper side is the visualization engine, and the lower side is the text output from the software.

The user interface of the software is built concurrently with the model and modified according to the developments in the model. The development of the user interface with wxWidgets is performed with a trivial design program called wxGlade, which converts the user interface elements like buttons and menus to the commands that are used by wxWidgets. VTK is incorporated manually by using an external class, called *wxVTKRenderWindowInteractor*, that makes it possible to connect the VTK with wxWidgets. The design of the user interface is similar to the structure of the many CAE programs, where the left panel is dedicated to the user input and the right panel is designated for the software output. The final form of the GUI is depicted in Figure C.2.

The most important element of the code is the generation of the linear systems that are obtained after finite volume and finite difference discretizations. These computations are performed within the physical model classes, *ppsFluidModel* and *ppsEMModel*. All of the coefficient matrices and the variables are stored in separate arrays

to eliminate all the dependencies that may cause problems for parallelization. When the program is first started, the dynamic arrays that store the parameters are not yet initialized. After the user enters the sizes of the grid and the physical dimensions of the domain and hits the execution button, the dynamic arrays are initialized using this input.

It is possible from the GUI to specify which approximations are to be applied to the model. The text output screen is designed to give different outputs according to the approximations. Residuals are to be followed easily from the text output screen so it is possible to say whether the equations solved have converged, or if there is a convergence problem, which equation needs to be investigated. To save the results of a configuration, output text files are generated with predetermined time step intervals for the variables solved in the model.

Other than the parallelization routines which are performed with the Microsoft Parallel Patterns Library, the remaining parts of the code are cross-platform, which means that the implementation of the software into UNIX based operating systems is possible. It is designated as a future work to create a version of the software that can work in parallel also in UNIX based operating systems by utilizing parallelization tools like OpenMP and MPI.

APPENDIX D: GLOBAL NEUTRAL PARTICLE BALANCE AND ELECTRON ENERGY BALANCE

The neutral particle balance and the electron energy balance inside an RF ion thruster can be evaluated using a global balance as presented in [8]. These global balance equations are presented also here. These routines are implemented in AETHER and can be used to decrease the computational time. The neutral particle balance is:

$$\frac{\partial}{\partial t}\left(n_n V\right) = \frac{\dot{m}}{m_i} + \iint\limits_{wall} \Gamma_{wall} dA + \iint\limits_{grid} (1-\phi_i)\Gamma_{grid} dA - \phi_n A_{grid} \frac{n_n \bar{c}_n}{4} - \iiint \dot{n}_e dV$$

where $\dot{m}$ is the flow rate in kg/s, Γ denotes the ion flux to the walls and the grid, ϕ_i is the grid ion transparency, ϕ_n is the grid transparency to neutrals, $\bar{c}_n$ is the average neutral thermal velocity. The first term on the right hand side is the particle injection, the next two terms denote the recombination, the fourth term denotes the escaped neutrals through the grids, and the last term is the particles that are ionized. If the user prefers to use the global neutral particle balance, the neutral continuity and momentum equations are not solved within each time iteration. The electron energy balance is formulated similarly as follows:

$$\frac{\partial}{\partial t}\left(\frac{3}{2} k T_e \iiint n_e dV\right) = \iiint \frac{j_{e,\theta}^2}{\sigma} dV - \iiint \dot{n}_e e V_i dV - \iiint \dot{n}_{exc} e V_{exc} dV - \iint\limits_{wall} \left(2kT_e + e\phi_{sheath}\right) \Gamma_{wall} dA$$

where $j_{e,\theta}$ is the azimuthal electron current, Γ_{wall} is the electron flux to the walls, $\dot{n}_e$ is the ionization rate, and $\dot{n}_{exc}$ is the excitation rate. The term on the left hand side denotes the time rate of change of the thermal energy. The first term on the right hand side is the power deposition to the plasma, the second term on the right hand side is the power loss due to ionization collisions, and the third term on the right hand side is the power loss due to excitation collisions. The last term denotes the power loss due to the electrons that can overcome the sheath potential and leave the system.

APPENDIX E: LIST OF PUBLICATIONS FROM THIS RESEARCH PROJECT

The conference proceedings and journal submissions that have been produced during this research project are listed below:

Journal Publications

1. Turkoz, E.; M. Celik, "AETHER: A simulation platform for inductively coupled plasma," Journal of Computational Physics, March 2014 (Submitted).
2. Turkoz, E.; M. Celik, "2D electromagnetic and fluid models for inductively coupled plasma for RF ion thruster performance evaluation," IEEE Transactions on Plasma Science, Vol. 42, No. 1, pp. 235-240, 2014.

Conference Proceedings

1. Turkoz, E.; M. Celik, "2D axisymmetric fluid and electromagnetic models for inductively coupled plasma (ICP) in RF ion thrusters," 33rd International Electric Propulsion Conference, Washington, DC, 2013, IEPC-2013-294
2. Turkoz, E.; M. Celik, "2D fluid model for axisymmetric RF ion thruster cylindrical discharge chamber," 49th AIAA/ASME/SAE/ASEE Joint Propulsion Conference, San Jose, CA, July 2013, AIAA-2013-4110
3. Turkoz, E.; M. Celik, "Optimization of radio-frequency ion thruster discharge chamber using an analytical model," 6th International Conference on Recent Advances in Space Technologies (RAST), pp. 511-516, Istanbul, Turkey, 12-14 June 2013
4. Yavuz, B.; E. Turkoz, M. Celik, "Prototype design and manufacturing method of an 8 cm diameter RF ion thruster," 6th International Conference on Recent Advances in Space Technologies (RAST), pp. 619-624, Istanbul, Turkey, 12-14 June 2013

REFERENCES

1. Chabert, P. and N. Braithwaite, *Physics of Radio-Frequency Plasmas*, University Press, Cambridge, 2011.

2. Tsay, M. and M. M. Martinez-Sanchez, "Simple Performance Modeling of a Radio-Frequency Ion Thruster", 30^{th} *International Electric Propulsion Conference*, Florence, Italy, September 2007.

3. Barrett, R., M. W. Berry, T. F. Chan, J. Demmel, J. Donato, J. Dongarra, V. Eijkhout, R. Pozo, C. Romine, and H. Van der Vorst, *Templates for the Solution of Linear Systems: Building Blocks for Iterative Methods*, Vol. 43, SIAM, 1994.

4. Saad, Y. and M. H. Schultz, "GMRES: A Generalized Minimal Residual Algorithm for Solving Nonsymmetric Linear Systems", *SIAM Journal on Scientific and Statistical Computing*, Vol. 7, No. 3, pp. 856–869, 1986.

5. Lieberman, M. A. and A. J. Lichtenberg, *Principles of Plasma Discharges and Materials Processing*, John Wiley and Sons Inc., 2005.

6. Goebel, D. M. and I. Katz, *Fundamentals of Electric Propulsion - Ion and Hall Thrusters*, JPL Space Science and Technology Series, 2008.

7. Szabo, J. J., "Fully Kinetic Numerical Modeling of a Plasma Thruster", Ph.D. Thesis, Massachusetts Institute of Technology, Cambridge, USA, 2001.

8. Tsay, M., "Two-Dimensional Numerical Modeling of Radio-Frequency Ion Engine Discharge", Ph.D. Thesis, Massachusetts Institute of Technology, Cambridge, MA, USA, 2011.

9. Groh, K. H., H. J. Leiter, and H. W. Loeb, "RIT15-A Medium Thrust Range Radio-Frequency Ion Thruster", 2^{nd} *European Space Propulsion Conference*, ES-

TEC Noordwijk, Netherlands, 1997, 252-257.

10. Killinger, R., J. Mueller, R. Kukies, and H. Bassner, "RITA Ion Propulsion for ARTEMIS–Lifetime Test Results", 3^{rd} *International Spacecraft Propulsion Conference*, Cannes, France, October 2000.

11. Leiter, H., R. Killinger, M. Boss, M. Braeg, M. Gollor, S. Weis, D. Feili, M. Tartz, H. Neumann, and D. M. D. Cara, "RIT–μT – High Precision Micro Ion Propulsion System Based on RF-Technology", 43^{rd} *Joint Propulsion Conference and Exhibit*, Cincinnati, OH, July 2007, AIAA–2007–5250.

12. Loeb, H. W., D. Feili, G. A. Popov, V. A. Obukhov, V. V. Balashov, A. N. N. A. I. Mogulkin, V. M. Murashko, and S. Khartov, "Design of High–Power High–Specific Impulse RF–Ion Thruster", 32^{nd} *International Electric Propulsion Conference*, Wiesbaden, Germany, 2011, IEPC–2011–290.

13. Kawamura, E., D. B. Graves, and M. A. Lieberman, "Fast 2D Hybrid Fluid-Analytical Simulation of Inductive/Capacitive Discharges", *Plasma Sources Science and Technology*, Vol. 20, No. 3, p. 035009, 2011.

14. Suekane, T., T. Taya, Y. Okuno, and S. Kabashima, "Numerical Studies on the Nonequilibrium Inductively Coupled Plasma With Metal Vapor Ionization", *IEEE Transactions on Plasma Science*, Vol. 24, No. 3, pp. 1147 –1154, 1996.

15. Hammond, E., K. Mahesh, and P. Moin, "A Numerical Method to Simulate Radio-Frequency Plasma Discharges", *Journal of Computational Physics*, Vol. 176, No. 2, pp. 402 – 429, 2002.

16. Kumar, H. and S. Roy, "Two-dimensional Fluid Model of DC and RF Plasma Discharges in Magnetic Field", *Proceedings to the 36th AIAA Plasma Dynamics and Laser Conference, Toronto, Canada*, 2005.

17. Hsu, C. C., M. A. Nierode, J. W. Coburn, and D. B. Graves, "Comparison of Model

and Experiment for Ar, Ar/O 2 and Ar/O 2 /Cl 2 Inductively Coupled Plasmas", *Journal of Physics D: Applied Physics*, Vol. 39, No. 15, p. 3272, 2006.

18. Parent, B., S. O. Macheret, and M. N. Shneider, "Electron and Ion Transport Equations in Computational Weakly-Ionized Plasmadynamics", *Journal of Computational Physics*, Vol. 259, pp. 51–69, 2014.

19. Oh, D. Y., "Computational Modeling of Expanding Plasma Plumes in Space Using a PIC-DSMC Algorithm", Ph.D. Thesis, Massachusetts Institute of Technology, Cambridge, MA, USA, 1996.

20. Fife, J. M., "Hybrid-PIC Modeling and Electrostatic Probe Survey of Hall Thrusters", Ph.D. Thesis, Massachusetts Institute of Technology, Cambridge, MA, USA, 1999.

21. Celik, M., M. M. Santi, S. Y. Cheng, M. Martinez-Sanchez, and J. Peraire, "Hybrid-PIC Simulation of a Hall Thruster Plume on an Unstructured Grid with DSMC Collisions", 28^{th} *International Electric Propulsion Conference*, Toulouse, France, March 2003, also IEPC–03–134.

22. Goebel, D., "Analytical Discharge Model for RF Ion Thrusters", *Plasma Science, IEEE Transactions on*, Vol. 36, No. 5, pp. 2111 –2121, October 2008.

23. Chabert, P., J. A. Monreal, J. Bredin, L. Popelier, and A. Aanesland, "Global Model of a Gridded-Ion Thruster Powered by a Radiofrequency Inductive Coil", *Physics of Plasmas*, Vol. 19, No. 4, pp. 1–8, 2012, 073512.

24. Takao, Y., K. Eriguchi, and K. Ono, "Two-Dimensional Particle-in-Cell Simulation of a Micro RF Ion Thruster", 32^{nd} *International Electric Propulsion Conference*, Wiesbaden, Germany, September 2011, IEPC-2011-076.

25. Henrich, R. and C. Heiliger, "Three Dimensional Simulation of Micro Newton RITs", 33^{rd} *International Electric Propulsion Conference*, Washington, DC, Oc-

tober 2013, IEPC–2013–301.

26. T.J.M. Boyd, J. S., *Plasma Dynamics*, Barnes and Noble, New York, 1969.

27. Chen, F. F., *Introduction to Plasma Physics*, Plenum Press, New York, 1974.

28. Celik, M., "Experimental and Computational Studies of Electric Thruster Plasma Radiation Emission", Ph.D. Thesis, Massachusetts Institute of Technology, Cambridge, MA, May 2007.

29. "LXCAT Database", `http://www.lxcat.laplace.univ-tlse.fr`, accessed at January 2014.

30. Stewart, R. A., P. Vitello, D. B. Graves, E. F. Jaeger, and L. A. Berry, "Plasma Uniformity in High-Density Inductively Coupled Plasma Tools", *Plasma Sources Science and Technology*, Vol. 4, No. 1, p. 36, 1995.

31. Si, X.-J., S.-X. Zhao, X. Xu, A. Bogaerts, and Y.-N. Wang, "Fluid Simulations of Frequency Effects on Nonlinear Harmonics in Inductively Coupled Plasma", *Physics of Plasmas*, Vol. 18, p. 033504, 2011.

32. Lee, I., D. B. Graves, and M. A. Lieberman, "Modeling Electromagnetic Effects in Capacitive Discharges", *Plasma Sources Science and Technology*, Vol. 17, No. 1, p. 015018, 2008.

33. Kolev, S., T. Paunska, A. Shivarova, and K. Tarnev, "Low-pressure Inductive Discharges", *Journal of Physics: Conference Series*, Vol. 63, No. 1, p. 012006, 2007.

34. Rowlands, T. P., "Plasma Production by Helicon Waves", *Laser and Particle Beams*, Vol. 24, No. 4, pp. 475–493, 2006.

35. Xue, S., P. Proulx, and M. I. Boulos., "Extended-field Electromagnetic Model for Inductively Coupled Plasma", *Journal of Physics D: Applied Physics*, Vol. 34,

No. 12, p. 1897, 2001.

36. Fridman, A. and L. A. Kennedy, *Plasma Physics and Engineering*, Taylor & Francis, 2011.

37. Piejak, R., V. Godyak, and B. Alexandrovich, "A Simple Analysis of an Inductive RF Discharge", *Plasma Sources Science and Technology*, Vol. 1, No. 3, p. 179, 1992.

38. Versteeg, H. and W. Malalasekera, *An Introduction to Computational Fluid Dynamics - The Finite Volume Method*, Prenctice Hall, Essex, England, 1995.

39. Harlow, F. H. and J. E. Welch, "Numerical Calculation of Time-Dependent Viscous Incompressible Flow of Fluid with Free Surface", *Physics of Fluids*, Vol. 8, p. 2182, 1965.

40. Ferziger, J. H. and M. Peric, *Computational Methods for Fluid Dynamics, 3rd Edition*, Springer-Verlag, Berlin, 2002.

41. "COMSOL Multiphysics 4.3a", 2013, `http://www.comsol.com`, accessed at January 2014.

42. Rafatov, I., E. Bogdanov, and A. Kudryavtsev, "On the Accuracy and Reliability of Different Fluid Models of the Direct Current Glow Discharge", *Physics of Plasmas*, Vol. 19, No. 3, p. 033502, 2012.

43. Leiter, H., H. Loeb, and K.H.-Schartner, "RIT15LS and RIT15LP – The Development of High Performance Mission Optimized Ion Thrusters", 35^{th} *Joint Propulsion Conference and Exhibit*, Los Angeles, CA, June 1999, AIAA–99–2444.

44. "Journal of Fluids Engineering Editorial Policy Statement on the Control of Numerical Accuracy", `http://journaltool.asme.org/templates/JFENumAccuracy.pdf`, accessed at April 2014.

45. Boulos, M. I., "Induction Coupled RF Plasma", *Pure and Applied Chemistry*, Vol. 57, No. 09, 1985.

46. Hasegawa, A., "Plasma Instabilities and Nonlinear Effects", *Springer Verlag Springer Series on Physics Chemistry Space*, Vol. 8, 1975.

47. Zhu, Y., "Modeling of a Microwave Plasma Electron Source for Neutralization of Ion Thrusters", Ph.D. Thesis, Paul Sabatier University of Toulouse, France, 2013.

48. Baalrud, S. D., N. Hershkowitz, and B. Longmier, "Global Nonambipolar Flow: Plasma Confinement where All Electrons are Lost to One Boundary and All Positive Ions to Another Boundary", *Physics of Plasmas*, Vol. 14, No. 042109, pp. 1–6, 2007.

49. Fausett, L., *Applied Numerical Analysis Using MATLAB, Second Edition*, Pearson Prentice Hall, 2008.

50. Meijerink, J. and H. A. van der Vorst, "An Iterative Solution Method for Linear Systems of which the Coefficient Matrix is a Symmetric M-matrix", *Mathematics of Computation*, Vol. 31, No. 137, pp. 148–162, 1977.

51. Ozgen, A., "Numerical Study of Double-Diffusive Convection in Porous Media", M.S. Thesis, Bogazici University, 2001.

52. Krasner, G. E. and S. T. Pope, "A Description of the Model-View-Controller User Interface Paradigm in the Smalltalk-80 System", *Journal of Object Oriented Programming*, Vol. 1, No. 3, pp. 26–49, 1988.

53. Smart, J. and S. Csomor, *Cross-platform* GUI *programming with* W*x*W*idgets*, Prentice Hall Professional, 2005.

54. Schroeder, W. J. and K. M. Martin, *The* VTK *User's Guide*, New York: Kitware, 1998.

55. Campbell, C., R. Johnson, A. Miller, and S. Toub, *Parallel Programming with* M*icrosoft* .NET*: Design Patterns for Decomposition and Coordination on Multi-core Architectures*, O'Reilly, 2010.